Spectral engineering in multiphoton linear and nonlinear interferometry: the importance of being multimode

Der Naturwissenschaftlichen Fakultät
der Universität Paderborn
zur
Erlangung des Doktorgrades Dr. rer. nat.

vorgelegt von:
ALESSANDRO FERRERI
Paderborn, February 22, 2021

Erklärung der Selbstständigkeit

Hiermit versichere ich, die vorliegende Arbeit selbstständig verfasst und keine anderen als die angegebenen Quellen und Hilfsmittel benutzt sowie die Zitate deutlich kenntlich gemacht zu haben.

Paderborn, February 22, 2021 Alessandro Ferreri

Erstgutachter:	J.-Prof. Dr. Polina Sharapova
Zweitgutachter:	Prof. Dr. Stefan Schumacher
Vertreter des Mittelbaus:	Dr. Wolf-Rüdiger Hannes
Vorsitzender der Promotionskommission:	Prof. Dr. Artur Zrenner

Tag der Abgabe: February 22, 2021

Contents

Zusammenfassung

Parametrische Fluoreszenz (PDC) ist ein nichtlinearer Quanteneffekt, der größtenteils in quantumoptischen Aufbauten, aufgrund der Möglichkeit Paarphotonemissionen auszulösen, verwendet wird.

Innerhalb dieser Promotionarbeit wird festgestellt, dass die Spektraleigenschaften des PDC-Effekts eine im Rahmen der Quanteninterferometrie entscheidende Rolle spielen können. Die Argumentation ist in zwei Abschritte unterteilt, in denen lineare und nicht-lineare Interferenzsysteme unterschieden und analysiert werden.

Als Beispiel von linearer Quanteninterferenz wird die Hong-Ou-Mandel-Interferenz untersucht. In dieser Dissertation wird bewiesen, dass das HOM-Minimum im Koinzidenzprofil sich einem "antibunching" Peak zukehrt, wenn eine Vier- statt Zweiphotoninterferenz vorkommt und falls die Photonen Quantenkorrelationen aufweisen [1]. Außerdem wird die Anwesenheit von schnellen manipulierbaren Schwankungen in der Koinzidenzprofil bewiesen, wenn Verschränkung zwischen den zwei Interferometerkanalen ausgelöst wird [2].

Als Vorbild der nicht-linearen Interferometrie wird ein integrierter SU(1,1) Interferometer mathematisch gestaltet und seine Leistungen im Rahmen der Phasensensitivität geprüft. Innerhalb dieser Analyse werden zwei PDC-Prozesse als optisch-parametrische Verstärker, aus denen ein SU(1,1)-Interferometer besteht, genutzt. Es wird bewiesen, dass die Phasensensitivität das Shot-noise-Limit übersteigen kann [3].

Summary

The parametric down-conversion (PDC) is a nonlinear optical effect, largely used in quantum optical frameworks because of the possibility to create photon pairs, in some cases characterized by quantum correlations as well as frequency and polarization entanglement.

In this thesis, the role of the spectral features of the PDC in quantum interferometry is demonstrated. The argumentations here exposed is split in two parts, distinguishing linear and nonlinear interference phenomena.

An example of the first type is the two-photon Hong-Ou-Mandel (HOM) interference, where photons leave the same output door of a beam splitter only if they are identical. In this work it is demonstrated that in the four-photon scenario the coincidence profile changes drastically, and in particular, the HOM dip turns to an antibunching peak if photons undergo quantum correlations [1]. Furthermore, by inducing a spatial entanglement between the channels of the interferometer, the presence of fast oscillations in the coincidence probability is observed. The four photon scenario enables the manipulation of these oscillations as well as the creation of four-photon Bell states [2].

As a paragon of nonlinear interferometry, we mathematically model a relistic integrated SU(1,1) interferometer. In this framework, two PDC waveguides are utilised as optical parametric amplifiers constituting the interferometer. Despite the presence of dispersion, the proposed interferometer can overcome the shot noise limit [3].

Sommario

La conversione parametrica (PDC) è un fenomeno di ottica non lineare che ha trovato un ampio impiego in diversi sistemi fisici, ed in particolare in ottica quantistica, per la possibilità di generare coppie di fotoni correlati. La presenza di tali correlazioni assume un'importanza strategica in diversi settori dell'ottica quantistica e consente di scrivere l'Hamiltoniana del processo PDC attraverso una combinazione di modi spettrali.

Ciò che vogliamo dimostrare in questa tesi è che le caratteristiche spettrali della sorgente di fotoni (nel caso particolare, della PDC) svolgono un ruolo fondamentale in fenomeni di interferometria quantistica, e per tale fine, la argomentazioni presentate verranno divise in due macroaree in cui verranno affrontati diversi aspetti di interferometria lineare e non lineare.

Il caso più elementare di interferometria quantistica lineare è quello che viene indicato come interferenza Hong-Ou-Mandel (HOM). Questo processo asserisce che due fotoni interagenti in un beam splitter (BS) vengono rilevati come uscenti dalla stessa porta se giungono nel BS nello stesso tempo e se indistinguibili l'uno dall'altro. Nei casi esposti in letteratura, questo effetto non dipende dalle proprietà spettrali della sorgente fintantoché il principio di indistinguibilità dei fotoni non viene violato. Questa asserzione comunque smette di essere valida se ad interagire sono quattro fotoni piuttosto che due. In questo caso, possiamo notare che la probabilità di avere coincidenze presenta un picco anti-bunching la cui intensità dipende dalle correlazioni quantistiche dei fotoni interagenti [1]. L'interferometria a quattro fotoni risulta essere di particolare interesse anche per la sua flessibilità. Aggiungendo un convertitore di polarizzazione (PC) nel nostro interferometro, siamo ad esempio in grado di realizzare una condizione di entanglement spaziale tra i due bracci dell'interferometro, la quale si manifesta attraverso la presenza di picchi fortemente oscillanti nelle funzioni di probabilità. Infine, attraverso un controllo dei vari parametri siamo in grado di realizzare sia stati di Bell quadratici, sia una manipolazione sistematica delle oscillazioni nelle coincidenze [2].

Come esempio di interferenza non lineare, analizzeremo matematicamente il caso dell'interferometro SU(1,1). La nostra analisi si soffermerà sulle prestazioni di questo strumento in una versione integrata, ed in particolare ne testeremo la sensitività di fase. In particolare, il sistema specifico da noi considerato è formato da due processi PDC che svolgeranno il ruolo dei amplificatori parametrici che solitamente costituiscono l'interferometro. La caratterizzazione spettrale effettuata sullo strumento consente di mettere in luce effetti di dispersione che influenzano le prestazioni dell'interferometro. Ciononostante, la precisione dello strumento riesce a superare il cosiddetto "shot-noise limit". Questi effetti di dispersione possono comunque essere attenuati attraverso l'impiego di filtri focalizzati intorno la frequenza centrale di emissione [3].

Chapter 1

Introduction

The discovery of the particulate nature of the light in the beginning of twentieth century gave birth to a new branch in quantum physics, called quantum optics. It was immediately clear that the description of the light in terms of discrete bricks of energy, called photons, on one hand could solve many open questions, such as the ultraviolet catastrophe, and on the other hand it largely expanded the frontiers of the research through the exploration of new quantum interaction frameworks. From a conceptual point of view, the wave-particle duality was centre of a lively debate within the scientific community, because both light and matter were subject to a new interpretation of their own nature: what once was wave, can behave as particle and vice versa.

The formulation of light as excitation of the electromagnetic field (particles) is however a first step. In principle, a large amount of photons can still behave classically if their statistics tend to be for instance strongly random, thermal or poissonian. Consequently, a good test to distinguish the quantum from the classical essence in quantum optics is to study the photon statistics. A certain amount of photons tends to show quantum features if the mean value of the expected number of photons is higher than its variance, or in other words, if the photon statistics is narrower than a poissonian distribution (subpoissonian statistics). In that sense, it should not be surprising that a Fock state shows its quantum features in a more evident way than a coherent state: the number of photons in a Fock state is well determined.

However, along the last century, quantum mechanics offered further interesting perspectives and phenomena to explore. One of the most peculiar phenomenon is definitely the entanglement, which is a quantum property largely exploited in quantum optics, also because it can be applied in photonic frameworks. Entanglement is a unique quantum effect, and there is no analogy in classical physics. An attempt to define this property is: given a quantum system characterized by two or more partitions (or subsystems), this system is entangled if the information, that we can get from the measurement of an observable, is stored in a global state which cannot be traced back to the states of the partitions [4]. The final state is therefore written as the inseparable superposition of subsystem states. In other words, the information is spread over the partitions of the system, which are therefore strongly tied, or entangled. It is important to highlight that the entanglement can hold even if the subsystems are spatially separated, following that this effect can lead to non-local correlations.

So far we discussed different elements of the quantum reality, such as the wave-particle dualism, the photon subpoissonian statistics as well as the entanglement. A pertinent question can now be: is there a way to test a quantum optical system in order to bring such features to light (even literally)? One branch of quantum optics offering this possibility is given by quantum interferometry, which is the branch of quantum optics investigating the interference processes. These occur in special devises, called interferometers, when two waves (typically light beams or photons) interact in an optical element, returning a structured pattern as the output of a certain measurement. The structure of the interference pattern as well as the information we can achieve in this type of experiment can strongly depend on the nature of the interacting beams. A tailored example is the interference of two beams entering the two doors of a beam splitter (BS). As long as the features of the beams let us deal the radiation as a classical object, we have to expect that the beams leave the BS either from both channels or just from one of them. On the contrary, the employment of two single interacting photons instead of bright light would maximize the probability of having both photons leaving one of the two door, and annul the probability of having coincidences. This phenomenon, called Hong-Ou-Mandel (HOM) interference, is just one of the possible experiments in quantum optics demonstrating the possibility to test the "quantumness" of optical systems [5]. In this example, as well as in many others [6–10], interferometry becomes a prominent test to investigate the borders between what is classical and what is quantum.

It was mentioned that, depending on the light properties, we can deal with the light in terms of classical beams as well as in term of photons, leading to very diverse outcomes. The mathematical procedure to firstly define and then interpret the light as a quantum object takes generally the name of quantization of the electromagnetic field. In this framework, a single plane wave photon is interpreted as the excitation of one of the infinite modes of the electromagnetic field characterized by specific wave vector and polarization. This formalism also enables to precisely describe light states with a higher degree of complexity, closer to more realistic scenarios.

Indeed, we know that the radiation generated by photon sources typically used in labs for interference experiments is not found in plane wave modes, but it is characterized by specific spectral properties. It is well known, for instance, that nonlinear optical effects such as parametric down-conversion (PDC), largely exploited in quantum optics as source of squeezing light, create photons with a certain degree of quantum spectral correlations, depending on both the geometrical and physical structure of the nonlinear material as well as the spectral features of the laser [11]. The presence of these correlations can make the PDC state not separable, but expressible in terms of a set of infinite spectral modes. It becomes clear, that such complexity of the photon source makes the description of interference scenarios much more articulated and complicated.

In this context, this thesis attempts to partially answer the questions: can the spectral "multimodeness" of the source affect the photon interference? If yes, How? And also: which advantages can we take from it?

In order to answer these questions, we split the work in two parts, namely approaching the topic within the frameworks of linear and nonlinear interferometry. In both cases the PDC effect generated in periodic poled Potassium titanyl phosphate (ppKTP) waveguide is used as spectrally multimode photon state.

After a preparatory chapter, in which we present the most interesting features of the PDC state and the main concepts of interferometry and quantum metrology, in Chapter 3 we will face the HOM interference when four rather than two photons are generated in a PDC waveguide. We will treat this system extensively, explaining how our theoretical and experimental setup enables to split the photons in the two spatial channels of the interferometer and make them identical. Once the interference occurs, we will figure out if the pattern profile in the four-photon design is more sensitive to the spectral features of the photon source with respect to the typical two-photon HOM interference. In the second part of this chapter, we will further take advantage of the spectrally multimode four-photon design, but in a setup where the degree of spatial entanglement between the two channel of the interferometer can be maximized. We will see that this different framework is more flexible and allows to modify and further manipulate the interference pattern as well as the entanglement of the output state. Finally, in Chapter 3 we will describe a realistic integrated SU(1,1) interferometer, namely a nonlinear interference device, still taking into account the multimode structure of the PDC waveguides. Along the chapter, we will present two different designs comparing their performances. Once the most efficient design is delineated, we test the sensitivity of the interferometer when the device is subject to a discrete range of filtering and seeding strategies. From a detailed investigation of the cases explored in this thesis, we can establish the optimal conditions in which the interferometer can work. In the end of this thesis, it should be clear why the presence of spectral features of photons is so important in interference frameworks.

Chapter 2

Basics: photon source and interferometry

2.1 The parametric down-conversion process

The investigation of frameworks based on nonclassical light is an essential element in quantum optics and photonics. Sometimes the non-classicality of the employed light is straightforwardly yielded via optical phenomena, stemming from the nonlinear response of certain materials by intense electromagnetic fields. In other words, by taking advantages of the nonlinear features of such materials, it is possible to create light having strongly nonclassical and even quantum behaviours, mathematically described in terms of photon number states and Bell states. However, the nonlinear interaction depends on the intensity of the electromagnetic field as well as on the susceptibility of the material. For instance, a second order nonlinear effect is a phenomenon whose dielectric polarization density $\vec{P}$ is proportional to the second order susceptibility $\chi^{(2)}$ and quadratically proportional to the electric field, meaning that the interaction of three beams is expected: a typical example of this family is the so-called parametric down-conversion (PDC) [11], where a pump laser hits a nonlinear material, which responds generating a photon pair, typically called signal and idler photons.

The importance of the PDC effect in quantum optics is due to its extraordinary properties and is proved by the large amount of works in the literature where it is exploited in different scenarios, for instance in photon engineering [12], quantum cryptography [13,14], quantum walk [15,16] and photon interference [17]. Surely, one of the most interesting features is the entanglement between signal and idler photons [18–20]. In some situations, one may observe that signal and idler photons are connected by a frequency entanglement by examining the Joint Spectral Amplitude (JSA) of the biphoton state. Moreover, for some specific cases, PDC photons are also affected by polarization entanglement, which gives rise to spatial correlations in bulk systems [21,22].

Another element of interest is the possibility of describing the PDC effect as a squeezed source. It will be seen that both the degree of quantum correlations of the created photons and the power of the pump determine a squeezing in the quadrature space [23].

In this chapter, we will obtain an explicit expression of the two-photon state, starting from the definition of nonlinearity in quantum optics and the general Hamiltonian characterizing nonlinear phenomena; and step by step we will select terms identifying the PDC process in order to achieve an explicit mathematical form for the PDC state. In the second part we will focus our attention on the spectral properties of the PDC. We will see that the control of such features allows us to manipulate and tailor the biphoton state in accord to our purposes.

2.1.1 From energy to PDC state

A laser beam passing through a medium experiences an interaction which strongly depends on both the intensity of the incident radiation and the atomic properties of the used crystal. Assuming conventionally the crystal as an ensemble of electric dipoles, namely harmonic oscillators, the first order of interaction leads to the well known refraction process, which can be seen as the linear response of the medium to an electric stress. Nevertheless, as increasing the pump intensity, the linear approximation does not hold any more, and nonlinear response of the material occurs. In order to take into account such effects in the mathematical model, the vector describing the polarization inside the medium $P(t)$ needs to be Taylor expanded at higher orders, namely:

$$P_i(t) = \epsilon_0 \left[\sum_j \chi_{ij}^{(1)} E_j(t) + \sum_{jk} \chi_{ijk}^{(2)} E_j(t) E_k(t) + \sum_{jkl} \chi_{ijkl}^{(3)} E_j(t) E_k(t) E_l(t) + \dots \right], \tag{2.1}$$

where ϵ_0 is the vacuum permittivity, and $\chi^{(n)}$ describes different order of susceptibility, and it can be seen as a coupling constant of the field interaction. Different polarization of the fields are labelled by ijk. The relative displacement vector is therefore:

$$\vec{D}_i(\vec{r}, t) = \epsilon_0 \vec{E}_i(\vec{r}, t) + \vec{P}_i(\vec{r}, t). \tag{2.2}$$

Such field is necessary to define the energy of the electromagnetic field along the crystal, which is introduced by the Hamiltonian [24]:

$$\begin{aligned} H(t) &= \int_V d^3r \left(\vec{B}(t) \cdot \vec{H}(t) + \vec{E}(t) \cdot \vec{D}(t) \right) \\ &\approx \int_V d^3r \left[\vec{B} \cdot \vec{B} + E_i \left(\epsilon_0 E_i + \frac{\epsilon_0}{2} \sum_{ij} \chi_{ij}^{(1)} E_j + \frac{\epsilon_0}{3} \sum_{ijk} \chi_{ijk}^{(2)} E_j E_k \right) \right]. \end{aligned} \tag{2.3}$$

where $\vec{B}$ and $\vec{H}$ are the magnetic flux density and the magnetic field strength respectively. Conventionally, it is useful to split the Hamiltonian in two parts, namely by distinguishing the term due to the free propagation from the interaction:

$$H(t) = H_0(t) + H_I(t), \tag{2.4}$$

where

$$H_0 = \int_V d^3r \left(\vec{B} \cdot \vec{B} + \epsilon_0 \vec{E} \cdot \vec{E} + \frac{\epsilon_0}{2} \sum_{ij} \chi_{ij}^{(1)} E_i E_j \right) \tag{2.5}$$

is the free propagation of fields, i.e. the term containing both the unperturbed propagation of both magnetic and electric fields as well as the linear response of the waveguide, whereas

$$\hat{H}_I(t) = \frac{\epsilon_0 O}{3} \sum_{ijk} \chi^{(2)}_{ijk} \int_0^L dz \hat{E}_i(z,t) \hat{E}_j(z,t) \hat{E}_k(z,t) \tag{2.6}$$

is the term of interaction, characterized by the nonlinear susceptibility tensor and three interacting beams. In this expression, O corresponds to the overlap of all fields along the orthogonal direction of propagation. Estimating the integration volume equal to the size of the waveguide, it is reasonable that the overlap of the three fields is connected to the cross-section of the waveguide via $O = 1/\sqrt{A_{PDC}}$, where A_{PDC} is the cross-section. Since we are interested in PDC process in waveguide, we can consider just a collinear configuration, namely imposing that all beams propagate along one direction, and therefore we can focus on the integration along the length of the waveguide L. Furthermore, a proper description of the interaction needs to take into account the energy conservation of the process, namely $\omega_1 = \omega_2 + \omega_3$, where we label with ω_1, ω_2 and ω_3 the frequency of $E_i(z,t)$, $E_j(z,t)$ and $E_k(z,t)$ respectively.

Since we will work in the interaction picture, we will merely focus on the interaction Hamiltonian in Eq.(2.6); an explicit expression of the quantized electromagnetic field is therefore required. In quantum electrodynamics and optics, the full expression of the electric field is given by [25]:

$$\hat{E}(\vec{r},t) = i \sum_{ki} \sqrt{\frac{\hbar\omega_k}{2\epsilon_0 n_{ki} V}} \left(\hat{a}_k \epsilon_{ki} e^{i(\vec{k}\vec{r} - \omega_k t)} - a^\dagger_k \epsilon^*_{ki} e^{-i(\vec{k}\vec{r} - \omega_k t)} \right). \tag{2.7}$$

where k describes the wave vector, i indicates the polarization, ω_k represents the allowed frequencies according to the energy conservation, ϵ_{ki} are unit vectors determining the polarization direction of the field, n_{ki} is the refractive index inside the material and V is the volume determined by the boundary conditions of the considered system.

As it may be noticed in Eq.(2.7), a fully quantum treatment of the electromagnetic field leads to an "upgrade" of the electric field from a classical function to a quantum operator. This allows, for instance, to explore a large spectrum of phenomena in both quantum optics and quantum electrodynamics, not predictable by a classical description of these fields, such as spontaneous emission [26,27], Lamb shift [28,29], Casimir effect [30,31] etc., or, more pertinent for our scopes, to carefully describe nonlinear interaction in medium, such as frequency conversion [32, 33], parametric down-conversion [33–35] and four wave mixing [36].

The absence of limited boundaries in the environment of the PDC waveguide allows us to operate in continuum. Mathematically it means that we can extend the quantization volume to infinity and transform the sums to integrals, so that the electric field becomes:

$$\hat{E}_i(z,\omega) = i \sqrt{\frac{\hbar\omega_0}{4\pi\epsilon_0 A n(\omega_0)}} \int d\omega \left(\hat{a}(\omega) e^{i(k(\omega)z - \omega t)} - \hat{a}^\dagger(\omega) e^{-i(k(\omega)z - \omega t)} \right), \tag{2.8}$$

where A labels the transverse quantization area of the material [37]. Since the bandwidth of fields is much smaller than the central frequency ($\Delta\omega \ll \omega_0$), we can assume that the field envelope slowly varies during the propagation of fields along the medium, such that we can mathematically fix the dispersion term in the central frequency and take the refrective index out of the integral. Then we transform the sum into integrals, the commutation rules for the annihilation and creation operators transform accordingly:

$$\left[\hat{a}(\omega), \hat{a}(\omega')^{\dagger}\right] = \delta(\omega - \omega') \qquad [\hat{a}(\omega), \hat{a}(\omega')] = 0. \tag{2.9}$$

In order to isolate the Hamiltonian of PDC from other effects, it is more convenient to split the electric field in two parts, by separating the positive and negative frequencies as following [25]:

$$\hat{E}(z,t) = \hat{E}^{(+)}(z,t) + \hat{E}^{(-)}(z,t), \tag{2.10}$$

hence, by substituting Eq.(2.10) in Eq.(2.6) we get:

$$\begin{aligned} \hat{H}_I(t) = \frac{\epsilon_0}{3} \sum_{ijk} \chi^{(2)} \int_0^L dz \left(\hat{E}_i^{(+)}(z,t) + \hat{E}_i^{(-)}(z,t)\right) \\ \times \left(\hat{E}_j^{(+)}(z,t) + \hat{E}_j^{(-)}(z,t)\right) \left(\hat{E}_k^{(+)}(z,t) + \hat{E}_k^{(-)}(z,t)\right). \end{aligned} \tag{2.11}$$

Some terms of this Hamiltonian, such as $\hat{E}_i^{(+)}\hat{E}_j^{(+)}\hat{E}_k^{(+)}$ or $\hat{E}_i^{(-)}\hat{E}_j^{(-)}\hat{E}_k^{(-)}$ can be excluded because they do not fulfil the energy conservation, but other terms enable to describe a remarkable number of non-linear processes in quantum optics. For instance, focusing just on PDC, we can distinguish three types of PDC process, depending on the relation between pump laser and output photons polarization: we indicate with "Type-0" the PDC process characterized by pump, signal and idler having same polarization; with "Type-I" the PDC process when both signal and idler photons have the same polarization and the pump polarization is orthogonal; and finally with "Type-II" the case when signal and idler photons have orthogonal polarizations. Henceforth, since in this work the possibility to distinguish signal from idler is fundamental, we will only focus on Type-II PDC process. From Eq.(2.11) we can therefore select just the following term:

$$\hat{H}_{PDC}(t) = \frac{\epsilon_0}{3} \chi^{(2)} \int_0^L dz \hat{E}_p^{(+)}(z,t) \hat{E}_s^{(-)}(z,t) \hat{E}_i^{(-)}(z,t) - h.c., \tag{2.12}$$

where we renominate all beams with the well-known names present in literature: p, s and i correspond to "pump", "signal" and "idler" respectively.

Having identified the Hamiltonian of the PDC process, Eq.(2.12), we can firstly define the unitary transformation (starting from Hamiltonian in Eq.(2.12)):

$$\hat{U}_{PDC} = \mathcal{T} \exp\left[-\frac{i}{\hbar} \int_{\infty}^{\infty} dt \hat{H}_{PDC}(t)\right], \tag{2.13}$$

and finally obtain the PDC state:

$$|\psi\rangle_{PDC} = \hat{U}_{PDC}|0\rangle = \mathcal{T} \exp\left[-\frac{i}{\hbar} \int_{-\infty}^{\infty} dt \hat{H}_{PDC}(t)\right] |0\rangle. \tag{2.14}$$

In this expression, we had to introduce the time ordering operator $\mathcal{T}$ due to the fact that the Hamiltonian does not commute with itself at different times [33,38]. Although effects due to the temporal ordering can play a crucial role in the PDC effect and can therefore modify remarkably the results in the high gain regime (characterized namely by a high pump power and hence more photons) [39], they are not particularly relevant for our scopes, so that we can ignore them by eliminating the time ordering operator from the expression written above:

$$|\psi\rangle_{PDC} \simeq \exp\left[-\frac{i}{\hbar}\int_{-\infty}^{\infty} dt\hat{H}_{PDC}(t)\right]|0\rangle. \tag{2.15}$$

Now we are able to explicitly write down the temporal integral in Eq.(2.15). Taking advantage of the large number of photons, we can treat the pump beam classically, which means that we do not need to quantize the field amplitude. Hence we can write:

$$\int_{-\infty}^{\infty} dt\hat{H}_{PDC}(t) = B\int_{-\infty}^{\infty} dt\int_0^L dz\iiint d\omega_p d\omega_s d\omega_i \exp[-i(\omega_p-\omega_s-\omega_i)t] \tag{2.16}$$

$$\times\sqrt{\frac{I}{\hbar\omega_p}}\exp[i(k_p(\omega_p)-k_s(\omega_s)-k_i(\omega_i))z]\hat{a}^\dagger(\omega_s)\hat{a}^\dagger(\omega_i) - h.c. \tag{2.17}$$

where we collect all constants in B and introduce the pump intensity I. By performing the integration over the direction of propagation z we have

$$\int_{-\infty}^{\infty} dt\hat{H}_{PDC}(t) = B\int_{-\infty}^{\infty} dt\iiint d\omega_p d\omega_s d\omega_i \alpha(\omega_s,\omega_i) \tag{2.18}$$

$$\times L\,\mathrm{sinc}\left[(k_p(\omega_p)-k_s(\omega_s)-k_i(\omega_i))\frac{L}{2}\right]\exp[-i(\omega_p-\omega_s-\omega_i)t] \tag{2.19}$$

$$\times\exp\left[i\,(k_p(\omega_p)-k_s(\omega_s)-k_i(\omega_i))\,\frac{L}{2}\right]\hat{a}^\dagger(\omega_s)\hat{a}^\dagger(\omega_i) - h.c. \tag{2.20}$$

where we defined the pump spectral function

$$\alpha(\omega_s,\omega_i) = \sqrt{\frac{I}{\hbar\omega_p}}e^{-(\omega_p-\omega_s-\omega_i)^2 t_0^2/2}, \tag{2.21}$$

where t_0 is the pulse duration of the pump laser[1]. If the integration over time is performed, the delta function $2\pi\delta(\omega_p-\omega_s-\omega_i)$ appears and therefore the integration over ω_p gives finally:

$$|\psi_{PDC}\rangle = \exp\left\{2\pi B\int d\omega_s d\omega_i L\alpha(\omega_s,\omega_i)\,\mathrm{sinc}\left[\frac{\Delta kL}{2}\right]e^{i\frac{\Delta kL}{2}}\hat{a}^\dagger(\omega_s)\hat{a}^\dagger(\omega_i) - h.c\right\}|0\rangle, \tag{2.22}$$

where $\Delta k = k_p(\omega_p)-k_s(\omega_s)-k_i(\omega_i)$ is the so called phase matching function, and determines the momentum conservation of the process. In order to compact such expression, we introduce the coupling constant $\Gamma = 2\pi BL$ and the so called "joint spectral amplitude" function (JSA):

$$F(\omega_s,\omega_i) = \alpha(\omega_s,\omega_i)\,\mathrm{sinc}\left[\frac{\Delta kL}{2}\right]e^{i\frac{\Delta kL}{2}}, \tag{2.23}$$

---

[1] Other profiles of $\alpha(\omega_s,\omega_i)$ will be specified along this work opportunately.

so that from Eq.(2.22) we get finally

$$|\psi_{PDC}\rangle = \exp\left\{\Gamma \int d\omega_s d\omega_i F(\omega_s,\omega_i)\hat{a}^\dagger(\omega_s)\hat{a}^\dagger(\omega_i) + h.c\right\}|0\rangle, \tag{2.24}$$

which describes the state of a PDC process. Since the function $\alpha(\omega_s,\omega_i)$ in Eq.(2.21) exhibits the frequency dependence only in the exponential part, we point out that the prefactor $\sqrt{I/(\hbar\omega_p)}$ and consequently the dependence on the pump intensity, will be included in the coupling constant Γ henceforth. Next sections we will show how to manipulate both the momentum and the spectrum of both signal and idler photons. It will be clear soon, that such features play a fundamental role in different interference processes.

2.1.2 Quasi-phase matching

The possibility to manipulate the output beam, namely the frequency range of both signal-idler photons, is an important element in most of the typical setups working for instance in telecom regime. Normally, such possibility is spontaneously provided by properly tailoring the frequency of the pump laser. Nevertheless, although the choice of ω_p sets the energy conservation figured by the function $\alpha(\omega_s,\omega_i)$, the fulfilment of momentum conservation of the process described by the phase matching function $\Delta k(\omega_s,\omega_i)$, is not immediately reached. Indeed, it strongly depends on the optical features, and in particular the refractive index inside the waveguide which restricts the allowed frequencies for both signal and idler photons. Typically, such problem can be overcome by periodic poling the waveguide; but this choice leads to an alteration of the non-linear coefficient and subsequently the momentum conservation of the process [40, 41]. This solution is called quasi-phase matching. Experimentally, the modification of the non-linear coefficient can be done for instance by inducing strong and modulated electric field along the crystal in $LiNbO_3$ [42, 43] (see Fig.2.1) or by ion exchange process in case of KTP [44].

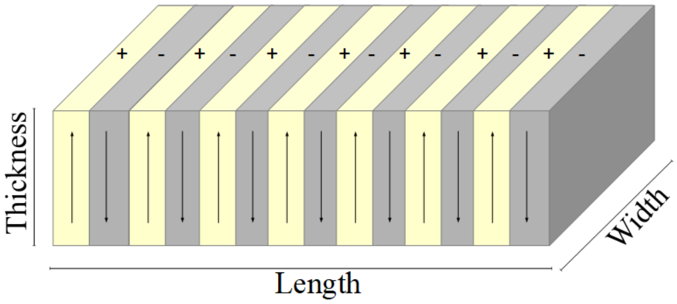

Figure 2.1: Sketch of a periodic poled PDC section

Mathematically, it corresponds to substituting the constant nonlinear coefficient in the Hamiltonian (see Eq.(2.6)) with a spatially, periodically modulated coefficient, which approximately is

$$\chi^{(2)}(z) = \chi_0^{(2)} \sin\left(\frac{2\pi}{\Lambda}z\right). \tag{2.25}$$

The temporal integration of the hamiltonian becomes:

$$\int_{-\infty}^{\infty} dt\hat{H}_{PDC}(t) = \frac{\epsilon_0}{3}\int_{-\infty}^{\infty} dt \int_0^L dk\chi^{(2)}(z)\hat{E}_p(z,t)\hat{E}_s(z,t)\hat{E}_i(z,t) \tag{2.26}$$

$$= B\int_{-\infty}^{\infty} dt \int_0^L dz \iiint d\omega_p d\omega_s d\omega_i \exp[-i(\omega_p - \omega_s - \omega_i)t] \tag{2.27}$$

$$\times\frac{1}{2i}\Bigg(\exp\left\{ i\left(k_p(\omega_p) - k_s(\omega_s) - k_i(\omega_i) + \frac{2\pi}{\Lambda}\right) t\right\} \tag{2.28}$$

$$- \exp\left\{ i\left(k_p(\omega_p) - k_s(\omega_s) - k_i(\omega_i) - \frac{2\pi}{\Lambda}\right) t\right\} \Bigg) a^\dagger(\omega_s)a^\dagger(\omega_i) + h.c. \tag{2.29}$$

From the equation above it is clear that the phase matching function is split in two parts shifted from the original position by $\pm\frac{2\pi}{\Lambda}$. However, one of them can drop to zero by modifying the pump laser accordingly in order to obtain finally:

$$|\psi_{PDC}\rangle = \exp\left\{\frac{\Gamma}{2i}\int d\omega_s d\omega_i \alpha(\omega_s,\omega_i)\,\mathrm{sinc}\left[\frac{\Delta\beta L}{2}\right] e^{i\frac{\Delta\beta L}{2}}\hat{a}^\dagger(\omega_s)\hat{a}^\dagger(\omega_i) + h.c\right\}|0\rangle, \tag{2.30}$$

where we introduced $\Delta\beta = \Delta k + \frac{2\pi}{\Lambda}$. The presence of the periodic poling allows to close the phase matching as needed and therefore to fix the emission frequency of the PDC process, by paying half of emission intensity though. Since in all cases considered in this work the quasi-phase matching technique is utilized, we will henceforward identify the PDC state as Eq.(2.30), and the corresponding JSA is:

$$F(\omega_s,\omega_i) = \alpha(\omega_s,\omega_i)\,\mathrm{sinc}\left[\frac{\Delta\beta L}{2}\right] e^{i\frac{\Delta\beta L}{2}}. \tag{2.31}$$

In the reminder of this chapter, the pulse duration t_0 within $\alpha(\omega_s,\omega_i)$ will be simply indicated by t.

2.1.3 PDC as squeezing process

In this section we will show how to control the emission process and the degree of correlation of signal and idler photons, introducing the temporal Schmidt modes and lending different spectral characterizations to the PDC state.

As we have seen in the previous sections, the JSA consists of two superimposing elements, namely the pump profile $\alpha(\omega_s,\omega_i)$ and the phase matching function, that can be modified independently [45]. For instance, assuming $\alpha(\omega_s,\omega_i)$ as in Eq.(2.21), we can control the pump bandwidth by varying the pump pulse duration t.

On the other hand, we can change the shape and the orientation of the phase matching Sinc function by altering the length of the waveguide, the poling period and trivially using certain materials having specific refractive indices rather than others.

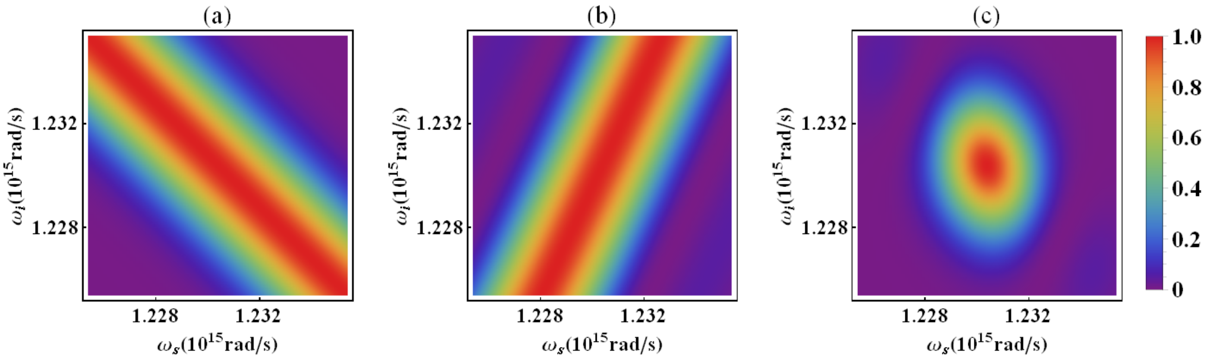

Figure 2.2: Plots of $\alpha(\omega_s, \omega_i)$ (a), phase matching function (b) and total JSI (c) of a PDC process in a KTP crystal in the single mode regime (low degree of correlation between signal and idler photons). Length of the crystal $L = 8mm$, poling period $\Lambda = 126\mu m$ and pulse duration $t = 0.346ps$. Schmidt number K=1.07.

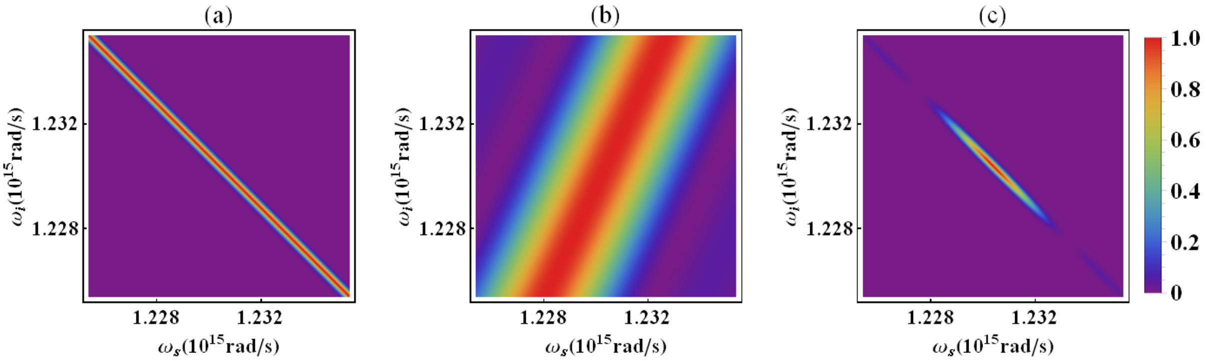

Figure 2.3: Plots of $\alpha(\omega_s, \omega_i)$ (a), phase matching function (b) and total JSI (c) of a PDC process in a KTP crystal in the multimode regime (high degree of correlation between signal and idler photons). Length of the crystal $L = 8mm$, poling period $\Lambda = 126\mu m$ and pulse duration $t = 5ps$. Schmidt number K=7.75.

Therefore, fixing a waveguide having specific optical properties distinctly, the only way we have to modify JSA is via varying the pump pulse duration. In Fig.(2.2) and Fig.(2.3) we plot the joint spectral intensity (JSI) $|F(\omega_s, \omega_i)|^2$ of two PDC processes distinguishable by just different values of t, when the source consists of a periodic poled KTP (ppKTP) waveguide.

The pictures show how to manipulate the JSI, in particularly increasing the pulse duration. It becomes clear that the reduction of the pump bandwidth causes a visible alteration of the JSI, which is upheld by a modification of the photon correlations. Roughly we can say that, as long as the JSI is close to be circular as in Fig.(2.2)c, a measurement on idler photon does not provide any clear information about the frequency of signal photon, determining an uncertainty in the knowledge of signal photon. In contrast, the JSI in Fig.(2.3) is quite narrow along the frequency antidiagonal, therefore the frequency of signal photon is heralded by the measurement on idler.

In this specific situation in which the pump profile is described by Eq.(2.21), the shape of the JSA is also connected with the degree of correlations of signal and idler photons.

A way to concretely estimate such correlations is via performing the so-called Schmidt decomposition of JSA in Eq.(2.31) [46, 47]:

$$F(\omega_s, \omega_i) = \sqrt{C} \sum_k \sqrt{\lambda_k} u_k(\omega_s) v_k(\omega_i) \tag{2.32}$$

where

$$C = \int d\omega_s d\omega_i |F(\omega_s, \omega_i)|^2 \tag{2.33}$$

is the normalization constant, λ_k are the normalized Schmidt eigenvalues, meaning that $\sum_k \lambda_k = 1$, and $u_k(\omega_s)$ and $v_k(\omega_i)$ are the spectral modes, called also Schmidt modes, for signal and idler photons respectively, which fulfil the orthonormality condition:

$$\int_0^\infty d\omega_s u_\mu(\omega_s) u_\nu^*(\omega_s) = \int_0^\infty d\omega_i v_\mu(\omega_i) v_\nu^*(\omega_i) = \delta_{\mu\nu}. \tag{2.34}$$

From Eq.(2.32) it is worth to notice that when $\lambda_1 = 1$ the JSA consists of a single spectral mode and the state is separable. This means that there is no correlation between signal and idler photons, nor entanglement. If the PDC state contains more than one spectral modes, such state is not separable any more and the degree of correlation increases. Therefore, in order to properly quantify such correlation between signal and idler photons, we introduce the so called Schmidt number $K = 1/(\sum_k \lambda_k^2)$: the higher is the value of K, the more correlated are signal and idler photons, and the JSA tends to become symmetrical along the diagonal axis $\omega_i = \omega_p - \omega_s$. A more common test to quantify the correlations in quantum optics is the measurement of the second order cross correlation function $g^{(2)}$. In this framework, the correlation between signal and idler photons is related to the Schmidt number via:

$$g^{(2)} = 1 + \frac{1}{K}. \tag{2.35}$$

This expression clarifies that the second order correlation function reaches 2 for noncorrelated states and tends to 1 for strongly correlated states. Cases reported in Fig.(2.2) and Fig.(2.3) are characterized by $g^{(2)} = 1.93$ and $g^{(2)} = 1.13$ respectively.

In the second part of this section we see how to mathematically elaborate the PDC state in order to rewrite it as a multimode squeezing state. Expressing the photon sources in terms of spectral modes is a strategy largely used in quantum optics, for instance in photon state engineering [48], tomography [49, 50] as well as in quantum information [51].

We start by defining both the so called Schmidt annihilation and creation operators for both signal and idler photon:

$$\begin{aligned} A_k^\dagger &= \int d\omega_s u_k(\omega_s) a^\dagger(\omega_s), \\ B_k^\dagger &= \int d\omega_i v_k(\omega_i) a^\dagger(\omega_i). \end{aligned} \tag{2.36}$$

The action of these operators on the state describe the creation of a signal-idler photon pair in the spectral mode k characterized by the spectra $|u_k(\omega_s)|^2$ and $|v_k(\omega_i)|^2$ respectively. These operators fulfil the typical bosonic commutation rules:

$$[A_k, A_j^\dagger] = \delta_{kj},\ [A_k, B_j^\dagger] = 0. \tag{2.37}$$

At this point, we just rewrite the Hamiltonian in terms of such operators defined above:

$$H = i\hbar\Gamma\sqrt{C}\sum_k \sqrt{\lambda_k}(A_k^\dagger B_k^\dagger - A_k B_k). \tag{2.38}$$

By substituting the Hamiltonian in Eq.(2.15) we get:

$$|\psi_{PDC}\rangle = \exp\left\{\Gamma\sqrt{C}\sum_k \sqrt{\lambda_k}(A_k^\dagger B_k^\dagger - A_k B_k)\right\}|0\rangle = \bigotimes_k S_k(\zeta_k)|0\rangle, \tag{2.39}$$

where

$$S_k(\zeta_k) = \exp\left\{\zeta_k(A_k^\dagger B_k^\dagger - A_k B_k)\right\} \tag{2.40}$$

are the two-mode (if signal and idler are distinguishable as in our case) squeezing operators and $\zeta_k = \Gamma\sqrt{\lambda_k}$ are the squeezing parameters, clearly showing that the PDC state is a product of squeezing states in the Schmidt basis. However, the squeezing characterization depends on different factors, such as the length of the waveguide, the pulse duration and the intensity of the pump. It is thus important to stress that the squeezing parameter itself clarifies that the amount of squeezing can be enhanced keeping the same number of spectral modes but increasing the pump intensity.

The action of the Schmidt operators on the initial state (vacuum in this case) is finally given by solving the Heisenberg equations for both A_k and B_k, taking into account the commutation rules given in Eq.(2.37):

$$\begin{aligned} \frac{dA_k}{dt} &= \Gamma\sqrt{\lambda_k}B_k^\dagger, \\ \frac{dB_k^\dagger}{dt} &= \Gamma\sqrt{\lambda_k}A_k. \end{aligned} \tag{2.41}$$

These equations can be solved using the Bogolyubov transformations, so that we can obtain the expression:

$$\begin{aligned} A_{k_{out}} &= A_{k_{in}}\cosh\left[G\sqrt{\lambda_k}\right] + B_{k_{in}}^\dagger \sinh\left[G\sqrt{\lambda_k}\right], \\ B_{k_{out}} &= B_{k_{in}}\cosh\left[G\sqrt{\lambda_k}\right] + A_{k_{in}}^\dagger \sinh\left[G\sqrt{\lambda_k}\right], \end{aligned} \tag{2.42}$$

where the parametric gain of the process $G = \int \Gamma dt$ was introduced. Such output operators can be used to calculate many interesting quantities in quantum optics. For example, we can calculate the output number of signal (idler) photons of the PDC effect as [52]:

$$N = \langle 0|A_{k_{out}}^\dagger A_{k_{out}}|0\rangle = \sum_k \sinh^2\left[G\sqrt{\lambda_k}\right], \tag{2.43}$$

highlighting the exponential growth of the number of photons for high pump intensities.

Following the same procedure, the Heisenberg equation can be solved also in terms of plane wave operators, yielding:

$$\begin{aligned} a^{out}(\omega_s) &= a^{in}(\omega_s) + \sum_k u_k(\omega_s) \\ \times \left[A_k^{in} \left(\cosh\left[G\sqrt{\lambda_k} \right] - 1 \right) \right. &+ \left. (B_k^\dagger)^{in} \sinh\left[G\sqrt{\lambda_k} \right] \right], \\ b^{out}(\omega_i) &= b^{in}(\omega_i) + \sum_k v_k(\omega_i) \\ \times \left[B_k^{in} \left(\cosh\left[G\sqrt{\lambda_k} \right] - 1 \right) \right. &+ \left. (A_k^\dagger)^{in} \sinh\left[G\sqrt{\lambda_k} \right] \right]. \end{aligned} \tag{2.44}$$

Both these set of operators will be of crucial importance along this work. The description of the PDC as a squeezing state will be a fundamental brick for engineering our model of the SU(1,1) interferometer and in particular it enables to bring out the analogies and the differences between the single mode squeezing vacuum, largely used as optical parametric amplifiers in theoretical SU(1,1) interferometer investigation, and the realistic PDC state.

2.1.4 Low gain regime

In many uses of PDC processes as photon source, it is not necessary to employ a pump with strong intensity, since a weaker one can already provide a suitable number of PDC photons. In condition of weak pump intensity, the expression in Eq.(2.24) can be treated in the so called "low gain regime", namely a condition characterized by $\Gamma \ll 1$, and expanded in Taylor expansion:

$$|\psi_{PDC}\rangle \approx |0\rangle + \Gamma \int d\omega_s d\omega_i F(\omega_s, \omega_i) \hat{a}^\dagger(\omega_s) \hat{a}^\dagger(\omega_i) |0\rangle. \tag{2.45}$$

The first term describes the zero order, which in this case is represented by the quantum vacuum, whereas the first order returns the PDC state in the low gain regime. For our purposes, we can ignore the zero order and normalize the PDC state to the first order:

$$|\psi_{PDC}\rangle \simeq \Gamma \int d\omega_s d\omega_i F(\omega_s, \omega_i) \hat{a}^\dagger(\omega_s) \hat{a}^\dagger(\omega_i) |0\rangle. \tag{2.46}$$

By definition it is clear that, in the low gain regime, $C\,\Gamma^2$ corresponds to the number of output photons generated by the waveguide. Along this work we will extend this expansion to the second order, so that we can generate two pairs of signal and idler photons at the same time.

2.2 Quantum interferometry

The second part of this introductory chapter will provide an overview of quantum interferometry and metrology. The main topic will be the distinction between linear and nonlinear interferometry in quantum optics [53]. A linear interferometer is a an interferometer characterized by linear transformations, typically beam splitter transformations [54]. We will see that in this kind of device the number of photons is a constant of motion, meaning that the photon number does not change during the propagation along the whole device. On the contrary, the nonlinear interferometer considered in this chapter, namely the SU(1,1) interferometer, consists of two optical parametric amplifiers (OPAs) [55]. In ideal conditions, the interaction between the beams and the OPAs leads to an enhancement (amplification) or to a reduction (deamplification) of the output intensity depending on some internal phase shifting, therefore the photon number is not a constant of motion. Very commonly both the linear and nonlinear interferometry are investigated by utilising a matrix strategy, which namely enables to treat all elements of the interferometer as matrices acting on the vector basis of the signal-idler annihilation/creation operators. Although this is a straightforward strategy when the input light consists of plane wave states, along this work we will see that it is not the most convenient to adopt when spectrally multimode sources are involved.

In order to start a more detailed description of the interference processes, we will firstly focus our attention on the linear interferometry. In particular, after introducing the concept of measurement in quantum optics, we will present the Hong-Ou-Mandel interference [5], which is a fundamental linear interference phenomenon in quantum mechanics, that can be used for instance to test the distinguishability of two photons. For this purpose, the PDC will be employed as a photon source of the interferometer. This choice allows to immediately present a formalism in which the spectral features of the source can be managed in order to control the interference pattern [56].

Afterwards, we will contextualise both the linear and nonlinear interferometry within the framework of quantum metrology. For this scope, it will be necessary to introduce fundamental concepts such as the phase sensitivity and the sensing limitations, and distinguish the two most common detection strategies utilized in quantum metrology, namely direct and homodyne detection. Finally, we will present a typical example of linear interferometer, called Mach Zehnder interferometer, testing the behaviour of the phase sensitivity at different input states. A similar analysis will be carried out in the context of the nonlinear interference along the last part of this section, where in particular we will test the performance of the SU(1,1) interferometer.

2.2.1 Quantum measurement

Before starting with the introduction of the HOM interference in more detail, it is fruitful to immediately introduce what a quantum measurement is, in particular the so called Positive Operator-Valued Measure (POVM) formalism [57], and the distinction between projective and non-projective measurement in quantum mechanics.

Let us suppose to have a quantum system described by the quantum state $|\psi\rangle$ and that we want to perform a measurement on it. One way to visualise such process consists in a projection of the state on the vectors generating the Hilbert space. In mathematical words, we firstly express the state via decomposing it on the vector basis of the Hilbert space, namely

$$|\psi\rangle = \sum_k b_k |\beta_k\rangle, \tag{2.47}$$

where $k = 1, 2, 3...$, while $|\beta_k\rangle$ and b_k are respectively the basis vectors of the Hilbert space and the probability amplitude to get the k state respectively; afterwards we define a set of projecting operators as

$$P_k = |\beta_k\rangle\langle\beta_k|, \tag{2.48}$$

fulfilling the completeness condition $\sum_k \langle\psi|P_k^\dagger P_k|\psi\rangle = 1$. Therefore, the action of P_k literally consists of a projection of the quantum state in one of the allowed states belonging to the basis, and the probability to obtain the state k as outcome is given by $p(k) = \langle\psi|P_k^\dagger P_k|\psi\rangle$, determining therefore the quantum statistics of our system[2].

Although this is a straightforward way to define the measurement process on the state mathematically, sometimes it might happen us to be interested not to the basis states, but to a new set of outcome states, expressed as superposition of basis elements like in Eq.(2.47). In this case, a projection measurement on the basis vectors is not efficient, because we want the measurement to distinguish and determine the states. Since all states are characterized by an own linear combination of basis elements, a projection measurement on the basis vectors is not really worthy, because the same basis vectors can appear in linear combinations of different outcome states.

In order to solve this uncertainty, it seems quite convenient to adapt the measurement design on the required output states by extending the definition of quantum measurement and introduce a specific set of measurement operators $\{M_k\}$, generally called POVM operators. Like the projectors, they must both fulfil the completeness condition $\sum_k \langle\psi|M_k^\dagger M_k|\psi\rangle = 1$ and be positive. The main idea of this strategy is therefore to fully identify the required states rather than to select one of the possible basis vectors. Such operators therefore enable to univocally identify the states we are investigating. On the other hand, the drawback of this strategy is that the completeness condition forces to define POVM operators which are useless for inferring something about the state we are measuring [57]. Along this text we will make use of POVM in order to calculate the coincidence probability in the four-photon Hong-Ou-Mandel framework.

2.2.2 Two-photon Hong Ou Mandel interference

In 1987 Chung Ki Hong, Zhe Yu Ou and Leonard Mandel demonstrated that two indistinguishable photons, entering a balanced beam splitter (BS) from two different spatial channels at the same time, experience an interference quite different from what was expected in classical optics [5]. It was known from classical interference experiences that two beams, interacting in a beam splitter and detected, originate a modulated interference pattern in the output channels if the time delay between them is tuned. The discovery of the HOM interference changed this paradigm drastically: Hong, Ou and Mandel demonstrated that the use of two single photons rather than two classical beams would generate completely different outcomes, i.e. two photons entering the BS at the same time can be only found in one of the two output channels and not split in both.

---

[2] In the specific case of projector operators, the quantum statistics can be simply expressed by $p(k) = \langle\psi|P_k|\psi\rangle$, since $P_k^\dagger P_k = P_k$.

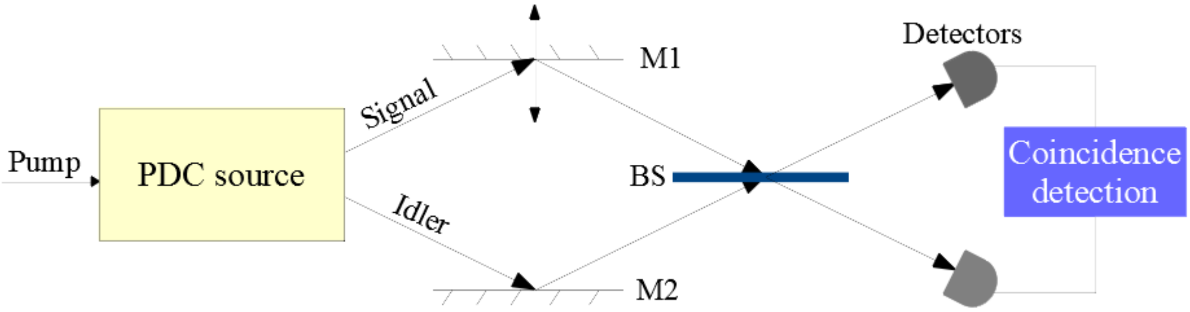

Figure 2.4: Schematic model of a typical HOM set-up. A pump laser interacts with a nonlinear medium (PDC source), creating a signal-idler photon pair. After the reflection in two mirrors (M1 and M2), they interfere on a beam splitter (BS) and are detected. The coincidence events are finally measured. The phase scanning is performed by spatially translating one of the two mirrors.

In order to give an explanation of such phenomenon in more detail, we will consider the scheme in Fig.2.4, where both signal and idler photons interfere in a beam splitter before getting detected. By moving one of the two mirror is hence possible to detect coincidence events at different time delays between the two photons. As it was already mentioned before, in this paragraph we make use of the PDC effect as photon source, and the spectral features of both signal and idler photons are taken into account [58,59]. For the sake of simplicity, we assume that we were already able to both separate signal and idler photons in two different channels and make them indistinguishable, so that we do not need to introduce too many elements in the description of this set-up, and we can only focus on the interference process itself[3].

Working in the low gain regime using the JSA as in Section 2.1.4, the quantum state entering the BS is the PDC state when the idler photon undergoes a time delay τ:

$$|\psi_i\rangle = \frac{1}{\sqrt{C}} \int d\omega_s d\omega_i F(\omega_s, \omega_i) e^{i\omega_s \tau} \hat{a}_1^\dagger(\omega_s) \hat{a}_2^\dagger(\omega_i) |0\rangle. \tag{2.49}$$

In this expression, the indices $\mu = 1, 2$ differentiate the upper from the lower channel of the 50:50 BS. The BS is mathematically described by a linear transformation turning the input creation operators to [54]:

$$\begin{aligned} a_1^\dagger &\rightarrow \frac{1}{\sqrt{2}} \left(a_1^\dagger + i a_2^\dagger \right), \\ a_2^\dagger &\rightarrow \frac{1}{\sqrt{2}} \left(a_2^\dagger + i a_1^\dagger \right). \end{aligned} \tag{2.50}$$

---

[3] Further theoretical and experimental details will be given along the next chapter and in the Appendix.

Hence, by letting this transformation act on the input state in Eq.(2.49) we have

$$
\begin{aligned}
|\psi_f\rangle &= \frac{1}{2\sqrt{C}} \int d\omega_s d\omega_i F(\omega_s, \omega_i) e^{i\omega_s\tau} \left(\hat{a}_1^\dagger(\omega_s) + i\hat{a}_2^\dagger(\omega_s)\right) \left(\hat{a}_2^\dagger(\omega_i) + i\hat{a}_1^\dagger(\omega_i)\right) \\
&= \frac{1}{2\sqrt{C}} \int d\omega_s d\omega_i F(\omega_s, \omega_i) e^{i\omega_s\tau} (i\hat{a}_1^\dagger(\omega_s)\hat{a}_1^\dagger(\omega_i) + i\hat{a}_2^\dagger(\omega_s)\hat{a}_2^\dagger(\omega_i) \\
&\qquad + \hat{a}_1^\dagger(\omega_s)\hat{a}_2^\dagger(\omega_i) - \hat{a}_2^\dagger(\omega_s)\hat{a}_1^\dagger(\omega_i))|0\rangle.
\end{aligned}
\tag{2.51}
$$

The first two terms represent the state with both signal and idler photon in the same channel, whereas they are in different channels according to the last two terms. It is interesting to notice that, if $\omega_s = \omega_i = \omega_p/2$ (monochromatic plane waves), Eq.(2.51) would return a final state where both photons are found either in the output channel 1 or in the output channel 2, as predicted by Hong, Ou and Mandel. Since we want to investigate the connection between the physical features of the PDC and the coincidences, we firstly define the POVM operators [57, 59]:

$$
M_b = \int d\omega_b d_1^\dagger(\omega_b)|0\rangle\langle 0|d_1(\omega_b), \tag{2.52}
$$

$$
M_c = \int d\omega_c d_2^\dagger(\omega_c)|0\rangle\langle 0|d_2(\omega_c), \tag{2.53}
$$

and the coincidence event is therefore given by:

$$
\begin{aligned}
P_{11} = \langle\psi_f|M_b \otimes M_c|\psi_f\rangle &= \int d\omega_b d\omega_c |\langle 0|d_1(\omega_b)d_2(\omega_c)|\psi_f\rangle|^2 \\
&= \frac{1}{4C} \int d\omega_b d\omega_c |F(\omega_b, \omega_c)e^{i\omega_c\tau} - F(\omega_c, \omega_b)e^{i\omega_b\tau}|^2.
\end{aligned}
\tag{2.54}
$$

This formula represents the probability that two detectors, described by the annihilation operators $d_1(\omega_b)$ and $d_2(\omega_c)$, catch two photons in different channels at frequencies ω_b and ω_c respectively; however, the integration over ω takes all frequencies into account. In order to plot this function for a large time delay range between the two photons, we want to split our argumentation in three different scenarios, depicted in Fig.(2.5) by different colours. The black curve characterizes the coincidence events when the input state contains a quasi-circular JSA (see Fig.2.2c); in a second scenario we can think to increase the pulse duration (red curve) in order to have a symmetrical JSA; finally we increase the length of the waveguide (blue curve). Since the group velocity of the signal photon is higher with respect to idler, the dip of the coincidence curve is found at positive time delay. This means that we need to extend the path of signal photon to compensate the path delay and let both photon arrive at the same time.

The first remarkable information we achieved in Fig.2.5 concerns the visibility, defined in the HOM experiments as $1 - P(\tau = 0)/P(\tau \to \infty)$. It is evident that this parameter varies in the black and red curves: indeed, the dip of the black curve does not reach zero, in contrast to the minimum point of the red curve. The reason of such difference is explainable by comparing the symmetry of JSA for both configurations: the JSA depicted in Fig.2.2c is not symmetrical along the diagonal $\omega_i = \omega_p - \omega_s$, meaning that the spectra of signal and idler photons are different from each other, violating the requisite

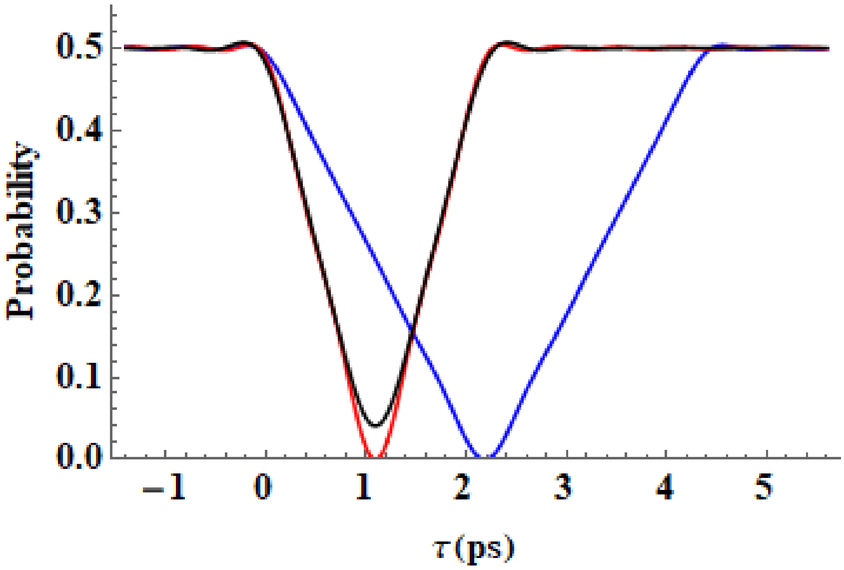

Figure 2.5: Coincidence probabilities by varying the time delay between signal and idler photons. A KTP section was used as photon source. In black line, $t = 0.346\,ps$ and $L = 8\,mm$; in red line $t = 1\,ns$ and $L = 8\,mm$; and in blue line $t = 1\,ns$ and $L = 12\,mm$.

of indistinguishability of the photons crossing the BS. Nevertheless, such problem can be solved for instance by enhancing the pump pulse, or in other words by reducing the spectral bandwidth of pump laser, thereby letting the JSA be diagonal and symmetrical (red curve). Mathematically, it means that $F(\omega_b, \omega_c) \simeq F(\omega_c, \omega_b)$, and the coincidence probability is reduced to

$$P_{11} = \frac{1}{2C} \int d\omega_b d\omega_c |F(\omega_b, \omega_c)|^2 [1 - \cos((\omega_b - \omega_c)\tau)], \tag{2.55}$$

clearly returning zero at $\tau = 0$.

Lastly we can notice that, if longer waveguides were used, the dispersion inside the waveguide would enhance the temporal bandwidth of both signal and idler photons, and consequently, also the overlapping range between them, making the interaction curve broader in time (blue curve).

We want to stress that as long as the condition $P_{11} = 0$ is fulfilled, the output state corresponds to the NOON state with N=2, which is a maximal entangled state [60]. Unfortunately, NOON states with higher photon number are not realizable via HOM interference.

In conclusion, we demonstrated that HOM interference is an extremely useful tool in order to test the distinguishability of two photons, moreover we highlighted that a manipulation of the photon source drastically modifies the coincidence profile of HOM dip. In the second part of this work we will show how a similar spectral engineering influences the four photon interference, finding also a direct connection between the coincidence probability and the number of Schmidt modes, not present in the two photon interference described so far.

2.2.3 Phase sensing and limitations

In interference experiments, whatever the required measurement is (intensity, coincidences, quadrature measurements), a certain phase object has to be scanned in order to delineate the specific modulation pattern.

Mathematically, this means that the output quantities depend on a certain element ϕ parametrically. In some cases the phase object can be simply designed as a constant parameter, depending only on the channel where it is located, so that the beam undergoes a phase modulation which does not depend on any optical quantities but is merely a constant. This approximation is typically used in single mode interferometry, as we will see along this chapter.

Sometimes the description of the interference process requires more accuracy, and it is necessary to express the parametric dependence in terms of time/path delay between the interacting objects. For example, the HOM profile in Fig.2.5 was accomplished by scanning the time delay between signal and idler photons before reaching the BS and finally detecting the coincidences. The description of the phase shift in terms of time (or space) delay between the optical beams allowed us to estimate the real order of magnitude of the interaction range. In Fig.2.5 the time delay was expressed in unity of ps, which is the same order of magnitude as that of the pulse duration. In some cases it may happen that the interference fringes are very fast, meaning that the detected quantity changes dramatically for short phase shifting. In this case, it is necessary to have an interferometer capable to perform very accurate measurements, whatever the detection strategy is.

Besides the accuracy of the interferometer, another element we have to care about in measurement contexts is the photon statistics. It is well known that photons having poissonian or super-poissonian distributions tend to have a large standard deviation the higher the mean number of photons is. This means that the measured outcome can dramatically vary from the expectation value because of statistic fluctuations, leading therefore to a false discrimination of the interference fringes. In that sense, it becomes worthwhile to estimate how sensitive the interferometer has to be in order to properly sketch the fringe pattern by phase scanning. To do that, it seems reasonable to define a parameter that quantitatively characterizes the sensitivity of the interferometer with respect to the variation of the internal phase.

In order to define such parameter, let us assume therefore to have a an observable O parametrically dependent on a phase ϕ. If we suppose to slightly deviate O by varying the phase parameter, the new value of the observable is expressed as [61]:

$$O(\phi + \delta\phi) \approx O(\phi) + \frac{\partial O}{\partial \phi}\delta\phi, \tag{2.56}$$

meaning that we performed a variation with respect to the original position amounting to $\delta O = O(\phi + \delta\phi) - O(\phi)$. At this point, it becomes opportune to make a proper discrimination of the origin of this variation. In other words, in a phase sensing experiment, one has to make sure that the scanned perturbation of the observable is specifically due to the variation of the phase and not to some statistical fluctuations. In order to determine this variation distinctively, it is necessary that the perturbation due to the phase scanning has to be greater or equal to the standard deviation of the observable, given by the square root of the variance $\sqrt{\Delta^2 O} = \sqrt{\langle O^2 \rangle - \langle O \rangle^2}$. Consequently, the minimal perturbation of the observable that we are able to sense must be the same order of magnitude of the standard deviation $\delta O \simeq \sqrt{\Delta^2 O}$. The variation of ϕ determining the smallest appreciable perturbation of O beyond the statistical fluctuation is therefore called sensitivity, and it is defined as

$$|\Delta\phi| = \left| \frac{\langle \Delta\hat{O} \rangle}{\partial \langle \hat{O} \rangle / \partial \phi} \right|, \tag{2.57}$$

where we expressed the observable as a quantum operator $\hat{O}$. Optimizing the trend of $\Delta\phi$ is one of the main goal of quantum metrology: the smaller such parameter is, the more precise one can profile the interference patterns.

Unfortunately, the progressive reduction of the phase sensitivity cannot lead to an ideal condition, in which the observable $\hat{O}$ is determined with 100% accuracy, and in fact, any improvement actually undergoes some practical limitations. For instance, in a typical linear interferometer, measurements can be altered by photon counting (detection) errors as well as vibrational movements in the phase scanner [62, 63]. In 1981, Caves attributed the movements of the mirrors in a Michelson interferometer to the radiation pressure carried out by the laser [62]. The employment of a photon source with lower intensity could partially balance and reduce the radiation pressure, but this intensity reduction makes the observable estimation dramatically subject to photon counting errors.

We can express this argumentation in terms of photon statistics. It is well known that a light beam having a very high intensity can be seen as a classical electromagnetic wave, namely a continuous wave with a certain profile. However, a dramatic reduction of the beam intensity lets the particle (quantum) nature of the light emerge, and the photon statistics of such coherent beam can be described by a poissonian distribution of photons. If we calculated and optimized the phase sensitivity of a linear interferometer seeded with such coherent state by making use of Eq.(2.57), we would obtain

$$\Delta\phi_{SNL} = \frac{1}{\sqrt{N_{in}}}, \tag{2.58}$$

where SNL is the denomination for "shot noise limit" and N_{in} is the number of photons inside the interferometer[4].

The expression in Eq.(2.58) can be intuitively achieved: assuming a typical sinusoidal modulation, the derivative of the output photon number in one channel is proportional to the radiation intensity undergoing the phase modulator, and the variance $\Delta^2 N$ is equal to the mean number of photons because of the poissonian distribution. Hence, in case of coherent states the optimized phase sensitivity corresponds to the inverse of signal-to-noise ratio (SNR),

$$\Delta\phi_{SNL} = \frac{1}{SNR} = \frac{\sqrt{N}}{N}, \tag{2.59}$$

where $SNR = I/(\Delta I)$, being I the intensity of the detected signal.

The SNL is a key element in quantum metrology. We can talk about sub-shot-noise measurement, when the interferometer we are working with is able to scan the same

---

[4] In principle, there is no reason to distinguish the number of photons inside the interferometer and in ouput, being these numbers identical in linear interferometry. However, we will use this nomenclature to conform the notation.

amount of photons N_{in} with a low sensitivity, namely when we are able to achieve a phase sensitivity scaling faster than the SNL, $\Delta\phi < \Delta\phi_{SNL}$. Caves was the first who identified the possibility to escape the impasse between photon counting error and radiation-pressure error by seeding one of the two doors of a Michelson interferometer with squeezing input state [62]. More generally, in linear interferometry, we will see that the interferometer can overcome the SNL by generating nonlocal correlations between the two arms of the interferometer [64]. In nonlinear interferometry, two-mode squeezing states generated by OPAs, for example Type-II PDC waveguides, can be spontaneously correlated. We will see that the presence of internal correlations explains why the SU(1,1) interferometer is able to beat the SNL even with vacuum state as input.

It was mentioned above that overcoming the SNL basically means reaching an expression of $\Delta\phi$ which can decrease faster than Eq.(2.58). Once photons inside the interferometer are correlated, another limit of quantum metrology can be reached,

$$\Delta\phi_{HL} = \frac{1}{N}, \tag{2.60}$$

called Heisenberg limit (HL), which stems from the use of nonclassical light [65]. It is clear that an interferometer having such sensitivity is able to discriminate the measured observable more precisely than a shot noise limited interferometer.

It is worthy to mention that both SNL and HL can be interpreted as results of the Heisenberg uncertainty principle for the phase and photon number [65]

$$\Delta N \Delta\phi \sim 1. \tag{2.61}$$

We saw that the variance of a coherent beam is equal to the photon number, therefore $\sqrt{N}\Delta\phi \sim 1$ is exactly the definition of SNL. However, in a quantum mechanical description Eq.(2.61) is equivalent to the Heisenberg uncertainty principle for time and energy. We said above that the variation of ϕ can be expressed in terms of time delay. The uncertainty of the number of photons during the phase scanning corresponds to a fluctuation of the energy, which in quantum mechanics can be of the order of magnitude of the energy itself $\Delta E \simeq E$. In terms of photon number, this leads to the Heisenberg limit in Eq.(2.60).

Before concluding this section, it is appropriate to mention that there are other methods to quantify the phase sensitivity. For instance, one common way is via estimating the Fisher information, namely how much information the parameter ϕ carries to the measurement outputs [66]. In a quantum scenario, the phase sensitivity is always bounded by the so-called quantum Cramer-Rao Bound (QCRB), given by

$$\Delta\phi \geq \frac{1}{\sqrt{F_Q}}, \tag{2.62}$$

where F_Q is the quantum Fisher information associated to the quantum state undergoing the phase shift. It is possible to demonstrate that the QCRB corresponds to the SNL when $F_Q = N$, whereas it corresponds to the HL when $F_Q = N^2$ [67]. However, since the Fisher information approach is not subject of this work, we will not go into further details.

2.2.4 Direct and homodyne detection in Quantum metrology

A crucial element of Quantum Optics is the photon detection. Depending on the system we are dealing with, the choice of the proper detection technique can be of strategic relevance. In quantum metrology, the most direct way to mathematically approach the light detection is the photon counting technique: supposing to have a final state expressed as a linear combination of Fock states, we can both determine the photon statistics by projecting the output state on the Fock basis, and calculate the average number photons by utilising the well-known expression $\langle \hat{N} \rangle = \langle \hat{a}^\dagger \hat{a} \rangle$. This way to quantify the outcome of a measurement is called "direct detection", because it allows to immediately estimate the photon number.

However, there are situations where this strategy is not particularly fruitful, whereas others can be more effective. For example, let us suppose to quantify the degree of squeezing of a state; in this case it would be more convenient to measure for instance the variance of the quadrature of the field. Such type of measurements can be performed by using the so called "homodyne detection" [68].

The scheme of the balanced version of this technique is modelled in Fig.2.6. In this detection scheme, the signal beam interacts with a strong coherent beam called "local oscillator" (LO) having the same frequency of the signal, in a 50/50 beam splitter.

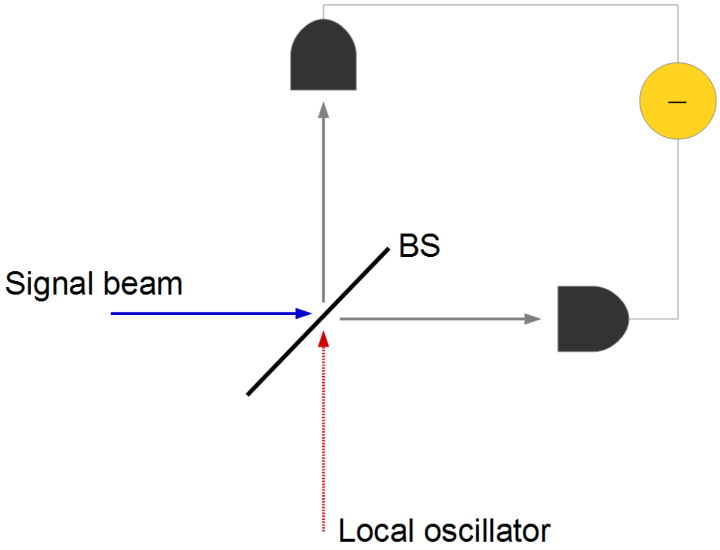

Figure 2.6: Schematic model of the balanced homodyne detection. The signal beam interacts in a balanced BS with a local oscillator. Finally, the output radiation is caught by two detectors and the difference between the intensities so detected is measured.

Calling a and b the annihilation operators of the input channel of the BS and with c and d the relative operators for the output channels, we can write the linear transformation of the BS:

$$c = \frac{a+ib}{\sqrt{2}} \tag{2.63}$$

$$d = \frac{ia+b}{\sqrt{2}} \tag{2.64}$$

where the coefficient $1/\sqrt{2}$ corresponds to the transmission and reflection parameter of the BS, being identical in a balanced homodyne detection. The detected number of photons is therefore given by:

$$c^\dagger c = \frac{1}{2}(a^\dagger a + b^\dagger b + ia^\dagger b - ib^\dagger a), \tag{2.65}$$

$$d^\dagger d = \frac{1}{2}(a^\dagger a + b^\dagger b - ia^\dagger b + ib^\dagger a). \tag{2.66}$$

In order to test the phase of the squeezed beam, we now need to determine the difference between the photocurrent (intensity) of both channels:

$$c^\dagger c - d^\dagger d = -i(a^\dagger b - b^\dagger a); \tag{2.67}$$

and tracing out the LO we can define the homodyne operator as:

$$H_d = \frac{|\beta_{lo}|}{2}(ae^{-i\theta} + a^\dagger e^{i\theta}), \tag{2.68}$$

where $|\beta_{lo}|$ and θ are respectively modulus and phase of the coherent parameter of the LO. From Eq.(2.68) it is clear that this operator can be utilized to measure the quadrature of squeezing states. The amplitude of the LO only causes a rescale and does not provide any further fruitful information.

The homodyne detection is of strong interest in quantum optics. For instance it is employed in quantum communication [69] and quantum cryptography [70], and is particularly used in quantum metrology along with the direct detection for special cases of photon sensing [66, 71]. In the last part of this work, we will make use of both direct and an adapted homodyne detections in order to quantify the phase sensitivity of the multimode SU(1,1) interferometer in case of seeding.

2.2.5 Mach-Zehnder interferometer

The first interferometer we want to present in this work is a specific design of SU(2) interferometer, usually called Mach-Zehnder due to its inventors. As shown in Fig.2.7, it consists of two spatially separated beam splitters and a detection set-up. In this scheme, two input beams enter the first beam splitter, which separates the radiation in two channels; a phase shifter located in one channel triggers a phase delay in the beam travelling through the relative channel; both beams interact in the second BS, and in the end, they are detected. Due to the phase delay, the intensity of the single channels is modulated, returning fringes of interference, although the total output intensity keeps constant along the whole interferometer[5].

---

[5] If no loss effects are included.

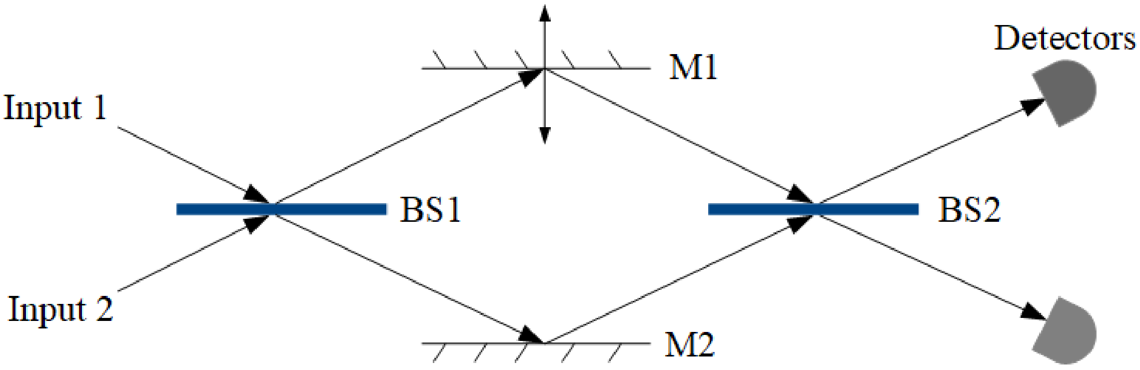

Figure 2.7: Schematic model of a Mach-Zehnder interferometer. Two input beams interact on the first beam splitter; after that one beam undergoes a phase delay, both beams interact on the second beam splitter and finally they are detected.

In order to both describe the Mach Zehnder set-up mathematically and finally evaluate the phase sensitivity for different configurations, it is worth to use a matrix representation, namely we define a set of unitary transformations, where every transformation, expressed as a matrix, refers to a specific element of the interferometer. This approach is quite practical for describing the interferometer when the radiation entering the BS consists of single plane wave modes, and it allows to obtain the output operators of the interferometer.

As first step, we both express the unitary transformations in terms of matrices and define the basis vectors. We proceed by calculating the overall transformation of the Mach-Zehnder interferometer, acting on the initial state vector and returning the final state. The two vectors that will be used as initial (i) and final (f) state are:

$$V_{i(f)} = \left\{ \begin{matrix} \hat{a}^{\dagger}_{i(f)} \\ \hat{a}_{i(f)} \\ \hat{b}^{\dagger}_{i(f)} \\ \hat{b}_{i(f)} \end{matrix} \right\} \tag{2.69}$$

where we distinguish the annihilation and creation operators for the two channels by choosing two different letters, a and b. In order to describe the BS transformation rigorously, we need to force the preservation of boson commutation relations at the output of the beam splitter, which means that we have to make sure that the sum of intensities of transmitted and reflected beams corresponds to the intensity of input beam [54], $T + R = 1$, which for instance is true when $R = \cos^2\theta$ and $T = \sin^2\theta$. The beam splitter transformation is therefore determined by:

$$M_\theta = \left\{ \begin{matrix} \cos\theta & 0 & i\sin\theta & 0 \\ 0 & \cos\theta & 0 & i\sin\theta \\ i\sin\theta & 0 & \cos\theta & 0 \\ 0 & i\sin\theta & 0 & \cos\theta \end{matrix} \right\}, \tag{2.70}$$

where, according to this notation, the parameter $\theta \in [0, \pi/2]$ determines the transparency of the BS: when $\theta = 0$, the BS is not working at all (full transmission); when $\theta =$

$\pi/2$ both beams are fully reflected; finally, for values in between we can have a partial transmission/reflection of the input light and in particular, for $\theta = \pi/4$ the incoming light is equally split in the two output channels of the BS (balanced configuration).

The transformation determining the phase shift depends on how many channels contain the phase modulator: supposing that in only one of the two channels the radiation undergoes the phase shift, the phase matrix is:

$$M_\phi = \begin{Bmatrix} e^{i\phi} & 0 & 0 & 0 \\ 0 & e^{-i\phi} & 0 & 0 \\ 0 & 0 & 1 & 0 \\ 0 & 0 & 0 & 1 \end{Bmatrix}, \tag{2.71}$$

where ϕ is the phase shift generated in one channel of the MZI. Consequently, we are now able to introduce the transformation for the whole Mach-Zehnder interferometer: $M_{tot} = M_\theta \cdot M_\phi \cdot M_\theta^\dagger$, where we suppose to work with perfectly identical balanced beam splitters[6]. Finally, by letting the matrix M_{tot} acting on the input vector Eq.(2.69) we can calculate explicitly the final annihilation and creation operators:

$$\begin{aligned} \hat{a}_f &= e^{i\phi/2}\left(\hat{a}_i \cos(\phi/2) - \hat{b}_i \sin(\phi/2)\right) \\ \hat{b}_f &= e^{i\phi/2}\left(\hat{a}_i \sin(\phi/2) + \hat{b}_i \cos(\phi/2)\right). \end{aligned} \tag{2.72}$$

Such operators are therefore the results of the total transformation on the input state and can be utilised for different goals. In this framework, since we are interested in the phase sensitivity estimation, we need to seek an operator $\hat{O}$ such that we can make use of Eq.(2.57). This choice is typically determined by both the employed detection strategy and the characteristics of the interferometer. For instance, we can notice that in the MZI interferometer it is not worthy to utilise the total photon number operator $\hat{N} = \hat{N}_a + \hat{N}_b$, where N_x is the number of photon in channel x, as observable to estimate the phase sensitivity, since in a Mach-Zehnder interferometer such quantity is always constant, i.e. it does not depend on the phase ϕ. Proper operators are provided by the group theory as suggested in [53] and [67], in particular we can analyse the performance of the MZI interferometer (namely estimate the phase sensitivity) by introducing the angular momentum operators:

$$\hat{J}_x = \frac{1}{2}(\hat{a}^\dagger \hat{b} + \hat{b}^\dagger \hat{a}), \quad \hat{J}_y = \frac{i}{2}(\hat{b}^\dagger \hat{a} - \hat{a}^\dagger \hat{b}), \quad \hat{J}_z = \frac{1}{2}(\hat{a}^\dagger \hat{a} - \hat{b}^\dagger \hat{b}). \tag{2.73}$$

These operators fulfil the angular momentum commutation relations $[\hat{J}_i, \hat{J}_j] = i\epsilon_{ijk}\hat{J}_k$. It is clear from Eq.(2.73) that $\hat{J}_z = \hat{N}_a - \hat{N}_b$, which is the difference in intensities between the two outputs. The phase sensitivity of Mach-Zehnder interferometer can be properly estimated by choosing J_z as observable. This can be done by firstly calculating both the derivative of the mean value and the variance of J_z and insert them into Eq.(2.57). In Tab.2.1 we show the phase sensitivity calculated for different input states [8, 66, 67]:

---

[6] The choice of $M_\theta^\dagger$ instead of M_θ as matrix of the first beam splitter is purely arbitrary.

Input state	$\langle N_i \rangle$	$\langle \Delta\phi \rangle$
$\lvert\alpha\rangle\lvert 0\rangle$	$\lvert\alpha\rvert^2$	$\frac{1}{\sqrt{N}}\lvert\sin\phi\rvert$
$\lvert N\rangle\lvert 0\rangle$	N	$\frac{1}{\sqrt{N}}$
$\lvert\alpha\rangle\lvert r\rangle$	$\lvert\alpha\rvert^2 + \sinh^2 r$	$\frac{\sqrt{\cot^2\phi(\lvert\alpha\rvert^2+\frac{1}{2}\sinh^2 2r)+\lvert\alpha\rvert^2 e^{-2r}+\sinh^2 r}}{\lvert\lvert\alpha\rvert^2-\sinh^2 r\rvert}$
$\lvert r_1\rangle\lvert r_2\rangle$	$\sinh^2 r_1 + \sinh^2 r_2$	$\frac{\sqrt{A(r_1,r_2)\cos^2\phi+B(r_1,r_2)\sin^2\phi}}{\lvert(\sinh^2 r_1-\sinh^2 r_2)\sin\phi\rvert}$
$\frac{1}{\sqrt{2}}\big(\lvert\frac{N}{2}\rangle\lvert\frac{N}{2}\rangle + \lvert\frac{N}{2}+1\rangle\lvert\frac{N}{2}-1\rangle\big)$	N	$\frac{\sqrt{\cos^2\phi+\sin^2\phi\left[\frac{N}{2}\left(\frac{N}{2}+1\right)-1\right]}}{\left\lvert\sin\phi+\cos\phi\sqrt{\frac{N}{2}\left(\frac{N}{2}+1\right)}\right\rvert}$
$\frac{1}{\sqrt{2}}(\lvert N\rangle_1\lvert 0\rangle_2 + \lvert 0\rangle_1\lvert N\rangle_2)$	N	$\frac{1}{N}$

Table 2.1: Overview of the Mach-Zehnder interferometer. Both the mean photon number and the phase sensitivity are illustrated for different input states.

where

$$\begin{aligned} A(r_1, r_2) &= -2\sinh^2 r_1 \sinh^2 r_2 + \cosh^2 r_1 \sinh^2 r_1 + \cosh^2 r_2 \sinh^2 r_2 \\ B(r_1, r_2) &= \frac{1}{2}\sinh 2r_1 \sinh 2r_2 + \sinh^2 r_1 \cosh^2 r_2 + \sinh^2 r_2 \cosh^2 r_1 . \end{aligned} \tag{2.74}$$

This table confirms what we have already mentioned in Section 2.2.3. As it can be seen in the first two cases, the phase sensitivity of the MZI is shot noise limited, namely it scales as $\Delta\phi \sim 1/\sqrt{N}$. The choice of seeding one channel was already criticized in [67], since it does not allow to induce correlation between the internal channel of the interferometer.

One way to induce such correlations is via using specific non-classical states as input, such as squeezed light [72, 73], as firstly suggested by Caves. It is interesting to notice that a scheme like Fig.2.4, where the phase modulation is located between the parametric amplifier and the first BS, already seems to operate beyond the SNL, even without the presence of a second BS [74].

It was claimed that the use of quantum input states such as Fock states is not enough for beating the SNL. However, one can use Fock states or combination of them to seed both channels of the interferometer in order to increase the degree of correlations between the two channels. Since both a well determined number of photons and the presence of non-classical correlations are required, these states are very hard to prepare, but on the other hand, they allow to beat the SNL and even reach the Heisenberg limit [65, 75]. Examples par excellence are the NOON states, which are highly correlated states with maximized entanglement [76]. The use of these states allows to make high sensitive measurements [8,77], moreover, they are a good compromise between the request of higher brightness for reducing photon counting errors, and the possibility of working with a non-fluctuating number of photons.

2.2.6 SU(1,1) interferometer

In the last section, it was seen that the presence of quantum correlations between the two channels of the MZI is mandatory in order to overcome the SNL. These correlations can be achieved via generating entangled states or introducing squeezing states into the MZI. Nevertheless, one can imagine to generate squeezing states inside the interferometer before the phase object. For this purpose, a new apparatus which consists of two squeezers substituting the beam splitters was ideated. This choice ensures the generation of nonclassical correlations inside the interferometer, required for beating the SNL. This special class of interferometers was developed in the last 40 years, and takes the name of SU(1,1) interferometer [53, 55].

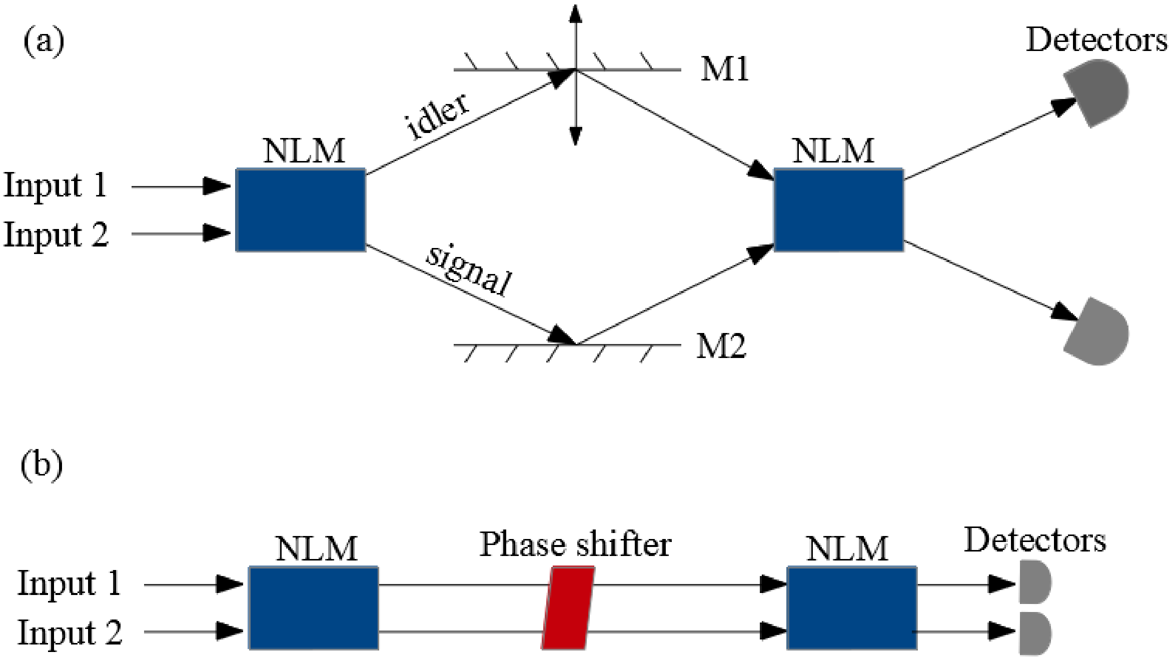

Figure 2.8: Schematic model of a SU(1,1) interferometer. Two input beams interact in a first nonlinear medium. The interaction between input light and the nonlinear medium generates a couple of signal-idler photons: in (a) one photon undergoes a phase delay (oscillation of mirror M1), in (b) all beams undergo the phase delay, in any case afterwards both photons interact on a second nonlinear medium. Such interaction induces either an amplification or a deamplification effect of the input signal depending on the internal phase. Finally they are detected.

The system is depicted in Fig.2.8: starting from the the Mach-Zehnder interferometer discussed above, two optical nonlinear media (NLM) or optical parametric amplifiers (OPA) take the place of both beam splitters, introducing the nonlinearity and in particular the effect of squeezing. This changes drastically the main features of the interferometer; for instance, the number of photons is not a conserved quantity any more, since the nonlinear phenomena commonly used (four-wave mixing, parametric down-conversion) affect the light intensity by generating (or annihilating) photons. The literature provides two configurations shown in Fig.2.8, depending on the number of beams undergoing the phase delay.

Mathematically, we can investigate the performance of this interferometer taking advantage of the same procedure used in the previous chapter; we need to define a new matrix, which substitutes the beam splitter transformations and represents the squeezing process [71]. For the sake of simplicity, we assume to have two identical squeezers described by the squeezer operators $\hat{S} = e^{r(\hat{a}\hat{b} - \hat{a}^\dagger \hat{b}^\dagger)}$, characterized by a real and positive[7] squeezing parameter r. The signal and idler modes are again identified by the letters a and b.

In this framework, the squeezing operator for the signal and idler modes can be rewritten as the action of a matrix transformation as following:

$$M_r = \begin{Bmatrix} \cosh r & 0 & 0 & \sinh r \\ 0 & \cosh r & \sinh r & 0 \\ 0 & \sinh r & \cosh r & 0 \\ \sinh r & 0 & 0 & \cosh r \end{Bmatrix}. \tag{2.75}$$

Such matrix determines the transformation of the annihilation and creation operators of the two-mode input state in Eq.(2.69) under the action of a squeezing process whose squeezing parameter is r. Recalling the phase matrix Eq.(2.71) and using the same procedure employed in the last section, we introduce the total matrix transformation of the SU(1,1) interferometer $M_{tot} = M_r \cdot M_\phi \cdot M_r$. By letting such matrix act on the input state in Eq.(2.69), we obtain the output creation and annihilation operators for both signal and idler photons:

$$\begin{aligned} a_f &= (\cosh^2 r\, e^{i\phi} + \sinh^2 r) a_i + \sinh r \cosh r (e^{i\phi} + 1) b_i^\dagger \\ b_f &= (\sinh^2 r\, e^{-i\phi} + \cosh^2 r) b_i + \sinh r \cosh r (e^{-i\phi} + 1) a_i^\dagger . \end{aligned} \tag{2.76}$$

These operators look very different with respect to what we calculated for the Mach-Zehnder interferometer, and reflect the nonlinear behaviour of the sources: indeed, annihilation operators depend on the creation operators and viceversa, and this is symptomatic of a nonlinear process.

Now we want to estimate the performance of the interferometer by calculating the phase sensitivity of such interferometer. As first case, we suppose to seed the interferometer with a coherent state $|\alpha\rangle$. For this purpose, we merely need to utilise the expression in Eq.(2.57), where, in this case, the observable $\hat{O}$ is the number of output photons. The calculation of the phase sensitivity gives [78]:

$$\Delta^2\phi = \frac{\cosh 2r \cosh 4r + \sinh 2r (\cosh 4r \cos^2\phi + \sin^2\phi) + \sinh 4r \cos\phi (\cosh 2r + \sinh 2r)}{4|\alpha|^2 \sinh^2 2r \sin^2\phi}. \tag{2.77}$$

When $e^{-2r} \ll 1$, namely for higher degree of squeezing, it can be shown that such formula can be drastically reduced to

$$\Delta\phi \simeq \frac{e^{-r}}{\sqrt{|\alpha|^2}}. \tag{2.78}$$

---

[7] The choice of a real and positive squeezing parameter is experimentally supported.

which is equal to the SNL damped by the exponential factor e^{-r}. This equation clearly shows that the SU(1,1) interferometer is able to overcome the SNL without requiring any exotic quantum input state, furthermore, the higher the squeezing gain is, the better performs the interferometer.

Anyway, we can exploit the fact that the SU(1,1) interferometer generates the interfering photons directly inside the apparatus via the OPAs, so that it appears worthy to make use of vacuum state (no seeding) as input in order to calculate the output quantities and therefore the phase sensitivity [53, 79]. It is clear that the input number of photons is zero, since both input channels contain no photons[8]. However, due to the squeezing vacuum generated inside the interferometer, the internal number of photons corresponds to $N_{in} = 2\sinh^2 r$. By repeating the same procedure, the phase sensitivity can be finally calculated:

$$\Delta^2\phi = \frac{2\coth^2 2r}{1-\cos\phi} - 1, \tag{2.79}$$

and, maximizing it at $\phi = \pi$, we achieve

$$\Delta^2\phi = \coth^2 2r - 1 = \frac{1}{\sinh^2 2r} = \frac{1}{N_{in}(N_{in}+2)} \simeq \frac{1}{N_{in}^2}, \tag{2.80}$$

which demonstrates that the SU(1,1) interferometer can beat the SNL and even reach the HL without seeding.

Before concluding this section, it is worth noting that all results and considerations reported heretofore only concern an idealistic version of the SU(1,1) interferometer. It means for instance that any losses were ignored[9], and secondly, we did not take into account eventual spectral features of the nonlinear media, but supposed to deal with single mode monochromatic squeezers. Such idealistic approximation does not hold in realistic set-up (without the employment of filters), where a full description of the temporal-spectral properties of the nonlinear source becomes necessary. Indeed, in the third chapter of this thesis we will see how the spectral properties of the nonlinear crystals influence the interference process and how we can optimize a realistic SU(1,1) interferometer in order to achieve the best performance.

2.2.7 Loss effects in the SU(1,1) interferometer

In order to investigate the influence of losses in the performance of the SU(1,1) interferometer, we have to distinguish two types: internal and external losses [79]. With the first ones, we normally indicate losses due to dissipative effects which can reduce the photon intensity inside the interferometer or distort the spectrum.

---

[8] We assume that the laser interacting with the OPAs and triggering the squeezing modes is a classical plane wave and therefore is not accounted as a quantum input state, coherently with the previous description of the parametric down-conversion process.

[9] Next session we will see that such losses do not strongly influence the main result of this section though, namely the fact that the SU(1,1) is able to overcome the SNL.

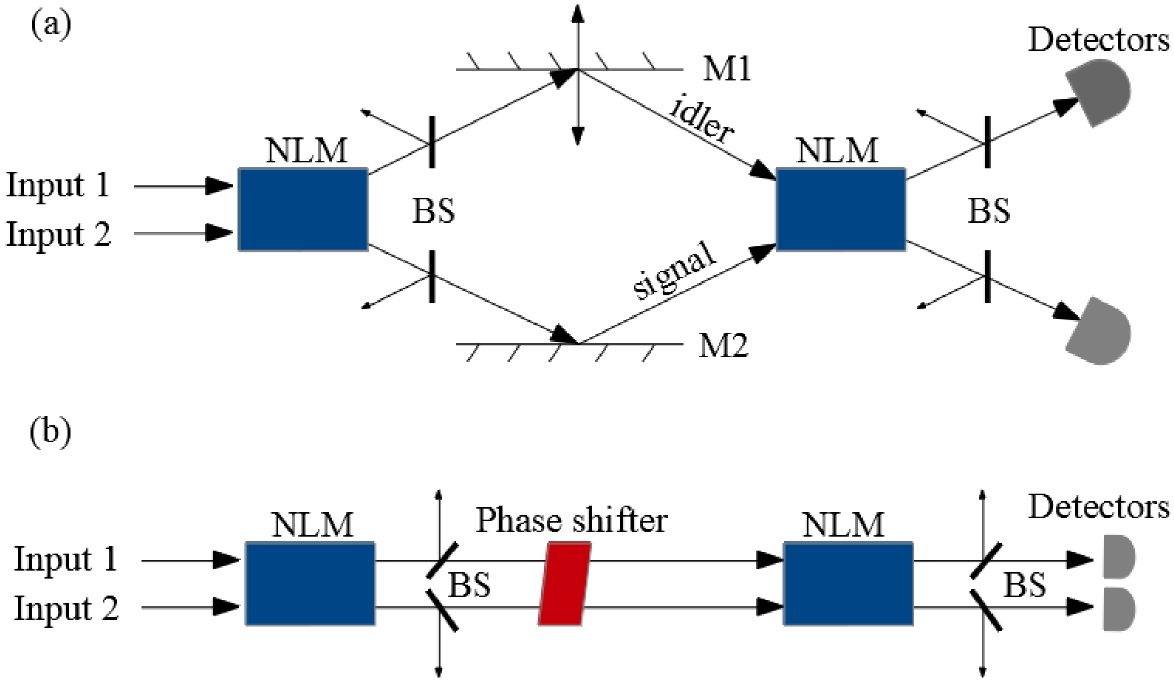

Figure 2.9: Schematic model of a SU(1,1) interferometer in Fig.2.8 taking into account losses effects. The internal losses are included via inserting beam splitters between the two nonlinear media, whereas the external losses are represented by beam splitters in front of the two detectors.

These can be due for instance to absorption phenomena or imperfections along the interferometer. Instead, external losses are typically due to non-perfectly efficient detectors, and though they do not belong strictly to the interferometer structure, they can in principle perturb the final results [80].

Although the losses can stem from multiple and different phenomena, for the sake of simplicity both internal and external losses can be mathematically taken into account in the previous model of the SU(1,1) interferometer by simply adding two beam splitter matrices, whose reflection coefficient determines the amount of lost radiation. The internal losses are therefore represented by beam splitters located between the two squeezing transformations, whereas the beam splitters depicting external losses, whose reflection coefficients determine the detector efficiency, are located in front of the detectors (see Fig.2.9). Normally such losses effects are independent from each other and are represented by different parameters; furthermore, in case of distinguishable interacting photons, it is commonly assumed that both signal and idler photons undergo the same amount of losses.

As first case, we can assume to have highly efficient detectors, meaning we can ignore external losses. The calculation of the phase sensitivity performed by using the procedure delineated above provides [81]:

$$\Delta^2\phi_\eta = \Delta^2\phi + \frac{1-\eta}{\eta}\left[\frac{2(N_{in}+1)}{(1-\cos\phi)N_{in}(N_{in}+2)} + \frac{1+(1-\eta)(N_{in}+1)}{\eta N_{in}(N_{in}+2)^2\sin^2\phi}\right], \tag{2.81}$$

where η determines the amount of internal losses. In this case, it can be seen that additional terms appear on $\Delta^2\phi$ calculated with no losses, showing that the new sensitivity profile is drastically modified. In particular, due to the last term inside the brackets, a divergent behaviour is expected where previously was the minimum of the phase sensitivity, namely at $\phi = \pi$. Such additional terms split the supersensitivity region in two parts by the presence of a central peak as shown in Fig.2.10, furthermore, by increasing the internal losses, the width of this peak increases and the supersensitivity region tends to reduce, demonstrating that the SU(1,1) interferometer is dramatically subject to internal losses.

Now we assume to have no internal losses but defected detectors and we indicate with ϵ their efficiency. In this case, the calculation of the phase sensitivity gives:

$$\Delta\phi_\epsilon^2 = \frac{1}{\epsilon}\Delta\phi^2, \tag{2.82}$$

which means that the external losses effects lead just to a rescale of the phase sensitivity, which anyway maintains the same functional form. In other words, the interferometer works at the same degree of precision as in the ideal case and in that sense we can affirm that the SU(1,1) interferometer is essentially immune to external losses. Ultimately, we can resume claiming that internal losses play a crucial rule in the SU(1,1) interferometer, whereas it is immune to external losses because of non-perfect detector efficiency [81].

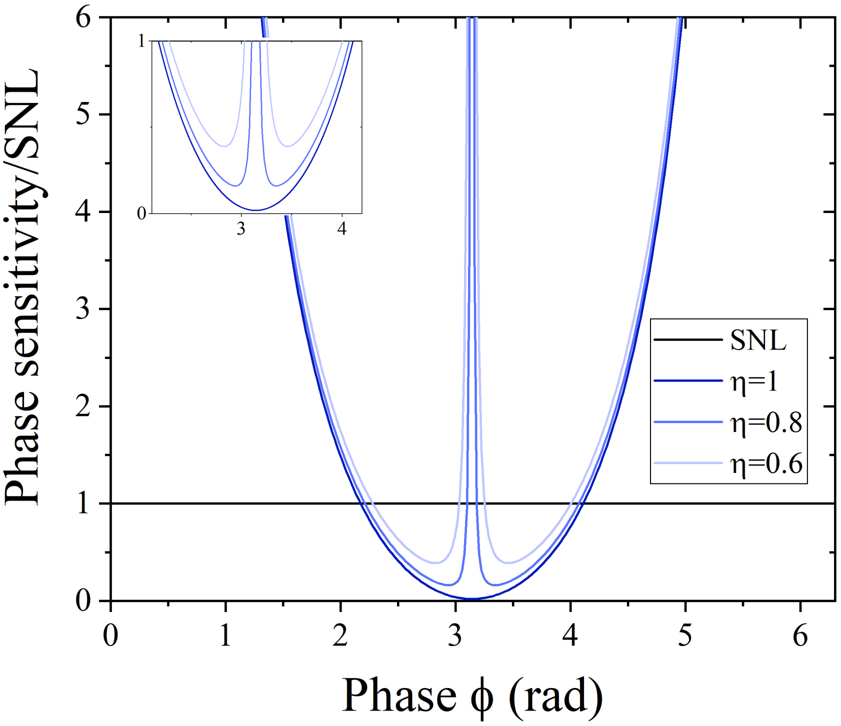

Figure 2.10: Normalized phase sensitivity respect to SNL (black line) as ϕ varies, for $\eta = 1$ (dark blue line), $\eta = 0.8$ (blue line) and $\eta = 0.6$ (light blue line). The red line indicates the SNL. $N_{in} = 5$. Insert: zoom on the supersensitivity region.

We conclude this chapter mentioning that the presence of a central peak in the phase sensitivity profile is not a peculiarity of loss effects. Indeed, along this work we will experience that in a more complex scenario, in which the spectral features of the photon sources are counted, the light travelling the interferometer undergoes dispersion due to its propagation in waveguides. The mismatching of the beams in the second OPA due to the different group velocities will generate both a reduction of visibility in the interference pattern and the consequent presence of a central peak in the phase sensitivity profile.

However, we will see that the consequence of such dispersion can be attenuated by modifying cunningly the interferometer and by making use of filters, as we will show in the last part of this work.

Chapter 3

Four-photon Hong-Ou-Mandel interference

The Hong-Ou-Mandel interference is one of the fundamental tools in quantum optics and quantum information theory [5], for instance, because it is one of the "easiest" investigable example of quantum interference effect, and also because it allows to directly test the indistinguishability of photon pairs. The flexibility of this phenomenon in different experimental strategies explains why it is so exploited for instance in quantum Bell-state measurement [82] or similarly for testifying the non-locality in entangled system [83], as well as in quantum lithography [84, 85].

Although these works demonstrate both the validity and the still promising potential of the two photon quantum interference, recent developments [86–92] seem to suggest a gradual approach to multiphoton interference platforms, namely where three or more photons are involved. The perspective of using multiphoton interference devices is particularly fruitful for different technological purposes, a typical example is quantum computing, via boosting for instance both boson sampling [93, 94] and machine learning [95–98].

Along the first section of this chapter, we will delineate another important aspect characterizing the multiphoton interference, namely the classical-to-quantum transition in a four-photon interference scheme. Such transition regime was already tested via using four-photon HOM interference in different scenarios, such as in [99] and in [100], where the effect of the pump power on the visibility of the interference pattern was investigated. On the contrary, we will carry out the classical-to-quantum transition in an elegant way via a manipulation of the pump laser profile, which leads to a fluctuation of the number of spectral modes, that consequently determines the presence of a bunching or antibunching peak.

The multiphoton HOM interference can also be used as first bricks for more complicated scenario. Proper modifications of the interference setup enables to test the indistinguishability of a many-particle systems [101, 102] as well as to generate multidimensional entangled state [103–106], such as Greenberger-Horne-Zeilinger (GHZ) states [107–109] or NOON state [110]; such states are often used to break the classical limit in interferometry [8, 111], as it was mention in the end of Section 2.2.5 as well as in quantum walks [112] and quantum communications [113].

In the second part of this chapter, we will demonstrate how the presence of only one additional tool, namely a further polarization converter, offers new aspects and perspective to analyse. In particular, we will be able to generate the spatial entanglement between the two arms of the interferometer; this will lead to fast oscillations in the coincidence probability. By manipulating some internal parameters, our interferometer will also yield combinations of high entangled states belonging to the four-quibit Bell gem introduced in [114,115]. Finally, via reaching the spectral indistinguishability of the four photons we will be able to further manipulate the fast interference fringes, whose periodicity will be smaller than the wavelength of the pump laser.

3.1 Temporal modes and antibunching peaks

3.1.1 Four-photon PDC state and set-up

When the two-photon interference was introduced in Sec.2.2.2 we emphasized the importance of the spectral properties of PDC state, connecting such features with the different profiles of the coincidence probability. In particular, it was seen that the symmetry of the JSA is a necessary condition to achieve the spectral indistinguishability of signal and idler photons, leading to a highly efficient HOM interference confirmed by a vanishing coincidence probability. Since we have already experienced the influence of the spectral features of the PDC on the outcome of the two-photon interference pattern, one can now wonder if the use of a higher number of interacting photons can provide a new spectrum of possibilities in the manipulation of the interference process [116]. In this section we will demonstrate how the employment of four photons changes the relation between spectral features of the source and the coincidence probability with respect to the two-photon interference.

The photon source we consider is the Type-II PDC process in a ppKTP waveguide. Mathematically, the four-photon state can be achieved from Eq.(2.14) by using the second order of the perturbation theory for $\Gamma \ll 1$. Experimentally, it can be done by enhancing the pump power reasonably, so that a significant number of photons is generated within the perturbation assumption. In this case, by neglecting the time ordering effects[1], the four-photon PDC state takes the following form [118–120]:

$$\begin{aligned} |\psi_{4ph}\rangle &= \frac{1}{2}\left(\int_0^t H(t')dt'\right)^2 |0\rangle = \\ = \frac{\xi^2}{2}\int_{-\infty}^{+\infty} d\omega_s d\omega_i F(\omega_s,\omega_i) a_H^\dagger(\omega_s) a_V^\dagger(\omega_i) &\times \int_{-\infty}^{+\infty} d\tilde{\omega}_s d\tilde{\omega}_i F(\tilde{\omega}_s,\tilde{\omega}_i) a_H^\dagger(\tilde{\omega}_s) a_V^\dagger(\tilde{\omega}_i)|0\rangle, \end{aligned} \tag{3.1}$$

where $\omega_s, \omega_i, \tilde{\omega}_s, \tilde{\omega}_i$ are the frequencies of the four generated photons, H and V indicate the horizontal and vertical polarization respectively, and $\xi = \Gamma t$, where t is the interaction time of the process. From Eq.3.1, one of the consequence of the inhibited time order effect is the possibility to deal with two temporal independent photon pairs.

The quantum state in Eq.(3.1) is the input state of the interferometer. As discussed in Section 2.2.2, in a HOM interference experiments we have to make sure that photons

---

[1] We assume that the generation processes along the PDC section happens so sporadically that two different output photon pairs do not spend a relevant amount of time in the same place [117].

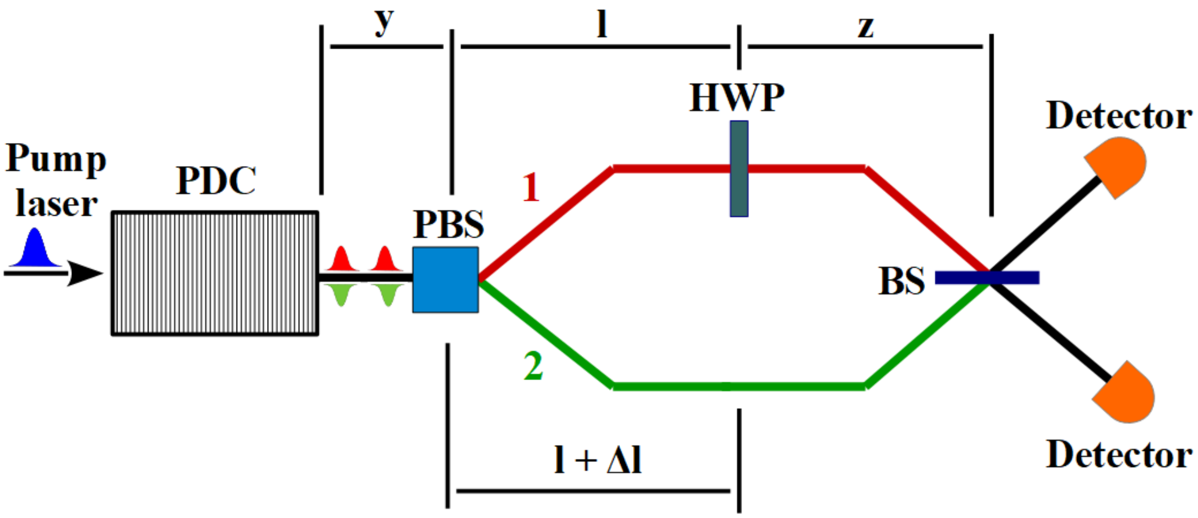

Figure 3.1: Schematic setup. The type-II PDC process generates two signal-idler pairs of photons. After PBS, two horizontally-polarized photons are routed to the channel 1 (red line), while two vertically-polarized photons, are routed to the channel 2 (green line). A half wave plate (HWP) located in the upper channel converts the horizontally-polarized photons into the vertically-polarized. An additional path increment $l+\Delta l$ in the lower channel allows to compensate the time delay between the signal and idler photons. Then four vertically-polarized photons cross the balanced BS at the same time, the HOM interference occurs. The photons are detected after the BS [1].

are split in the two arms of interferometer, so that they can reach the BS for two different doors. Moreover, a certain degree of photon indistinguishability must be reached. As it was seen in Eq.(3.1), output photons generated by Type-II PDC process are characterized by orthogonal polarizations. We can exploit this initial distinguishability to split photons in the two spatial channels of the interferometer. The indistinguishability can be finally achieved by using a polarization converter or a half wave plate, rotating the polarization of one photon opportunely.

In order to introduce the interferometer in more details, we sketch it in Fig.3.1 [1]. The picture shows the PDC source generating two photon pairs whose polarization is distinguished by green and red colours. Such photons reach a polarization beam splitter (PBS) splitting them in two spacial channels according to their own polarization. In order to finally observe four identical photons, a half wave plate (HWP) rotates the polarization of the photons in the upper channel by 90°, while both photons in the lower channel undergo a delay due to an additional path increment δl. The manipulation of the path delay allows to scan the interference pattern and eventually compensate the time delay due to the group velocity mismatching. This ensures all photons to reach the balanced BS at the same time. After the interference process, all photons are detected and the coincidence probabilities is measured and hence, by varying slightly the path delay it is possible to scan the coincidence probabilities.

Mathematically, the various components of the interferometer are described by unitary matrix transformations acting on the input state in Eq.(3.1), whereas the total transformation is given by the product of all matrices[2] :

$$U_{tot} = BS \times FP_3 \times HWP \times FP_2 \times PBS \times FP_1, \tag{3.2}$$

where BS, HWP and PBS are matrices corresponding to the relative optical elements, whereas all FP_x matrices represent the free propagation paths in between.

The initial state is given in the basis $\{a^{\dagger}_{1H}, a^{\dagger}_{1V}, a^{\dagger}_{2H}, a^{\dagger}_{2V}\}$ where 1 and 2 differentiate the two channels and the indices V and H the polarization. By applying the total transformation in Eq.(3.2), we can calculate the output state, namely the quantum state of the four photons leaving the interferometer and ready to get detected [59]:

$$\begin{aligned} |\psi_{out}\rangle = \frac{\xi^2}{2}\int \mathsf{d}\omega_s \mathsf{d}\omega_i \mathsf{d}\tilde{\omega}_s \mathsf{d}\tilde{\omega}_i F(\omega_s,\omega_i)F(\tilde{\omega}_s,\tilde{\omega}_i)\times \\ U_0(\omega_s)U^{\dagger}_{tot}(\omega_s)\begin{pmatrix} a^{\dagger}_{1H}(\omega_s) \\ a^{\dagger}_{1V}(\omega_s) \\ a^{\dagger}_{2H}(\omega_s) \\ a^{\dagger}_{2V}(\omega_s) \end{pmatrix} \otimes U_0(\omega_i)U^{\dagger}_{tot}(\omega_i)\begin{pmatrix} a^{\dagger}_{1H}(\omega_i) \\ a^{\dagger}_{1V}(\omega_i) \\ a^{\dagger}_{2H}(\omega_i) \\ a^{\dagger}_{2V}(\omega_i) \end{pmatrix} \otimes \\ U_0(\tilde{\omega}_s)U^{\dagger}_{tot}(\tilde{\omega}_s)\begin{pmatrix} a^{\dagger}_{1H}(\tilde{\omega}_s) \\ a^{\dagger}_{1V}(\tilde{\omega}_s) \\ a^{\dagger}_{2H}(\tilde{\omega}_s) \\ a^{\dagger}_{2V}(\tilde{\omega}_s) \end{pmatrix} \otimes U_0(\tilde{\omega}_i)U^{\dagger}_{tot}(\tilde{\omega}_i)\begin{pmatrix} a^{\dagger}_{1H}(\tilde{\omega}_i) \\ a^{\dagger}_{1V}(\tilde{\omega}_i) \\ a^{\dagger}_{2H}(\tilde{\omega}_i) \\ a^{\dagger}_{2V}(\tilde{\omega}_i) \end{pmatrix} |0\rangle, \end{aligned} \tag{3.3}$$

where the matrices $U_0(\omega)$ determine both the initial channel and polarization of signal and idler photons . We will make use of this expression for the calculation of the coincidence probabilities. In order to have a more clear visual of such state, we can express it in terms of the bidimensional Fock basis $|m,n\rangle$, where m and n represent the number of photons in the upper and lower channel, respectively[3]:

$$\begin{aligned} |\psi_{out}\rangle = \int \mathsf{d}\omega_s \mathsf{d}\omega_i \mathsf{d}\tilde{\omega}_s \mathsf{d}\tilde{\omega}_i (C_{22}(\Delta l,\tau)|2,2\rangle + \\ C_{31}(\Delta l,\tau)(|3,1\rangle + |1,3\rangle) + C_{40}(\Delta l,\tau)(|4,0\rangle + |0,4\rangle)). \end{aligned} \tag{3.4}$$

where $C_{m,n}(\Delta l,\tau)$ expresses the probability amplitude to get m and n photons in the upper and in the lower channel respectively. As expected, these coefficients depend strictly on all parameters concerning both the spectral properties of the PDC and the transformations along the interferometer. However, in Eq.(3.4) we only keep the dependence with respect to both the delay shift and the pulse duration explicitly. This expression shows clearly which kind of outputs we should expect from this interference. In contrast with the well-known two-photon interference, after the splitting we can distinguish three scenarios, depending on the number of expected photons found in every channel, namely we can have two photons per channel, three photons in the upper channel and one in the other (and viceversa) or we can find all photons in the same channel.

---

[2] Since every optical element of this interferometer could work more or less optimally, the respective matrix depends on a specific parameter, determining the efficiency of the optical tool. However, in this work we suppose that all elements are working with optimal efficiency [59].

[3] The Fock state counts the number of photon per channels, hiding their polarization and shifting the information about spectral distribution to the coefficients $C_{m,n}(\Delta l,\tau)$.

Since the output state is now well-known, we can use the POVM measurement strategy to calculate the measuring coincidence probabilities at the detectors:

$$P_{22}(\Delta l, \tau, L) = \int \mathsf{d}\omega_b \mathsf{d}\omega_c \mathsf{d}\tilde{\omega}_b \mathsf{d}\tilde{\omega}_c |\langle 0| \frac{1}{\sqrt{2!}\sqrt{2!}} d_1(\omega_b) d_2(\omega_c) d_1(\tilde{\omega}_b) d_2(\tilde{\omega}_c) |\tilde{\psi}_{out}\rangle|^2 \tag{3.5}$$

$$P_{31}(\Delta l, \tau, L) = \int \mathsf{d}\omega_b \mathsf{d}\omega_c \mathsf{d}\tilde{\omega}_b \mathsf{d}\tilde{\omega}_c |\langle 0| \frac{1}{\sqrt{3!}} d_1(\omega_b) d_1(\omega_c) d_1(\tilde{\omega}_b) d_2(\tilde{\omega}_c) |\tilde{\psi}_{out}\rangle|^2 \tag{3.6}$$

$$P_{40}(\Delta l, \tau, L) = \int \mathsf{d}\omega_b \mathsf{d}\omega_c \mathsf{d}\tilde{\omega}_b \mathsf{d}\tilde{\omega}_c |\langle 0| \frac{1}{\sqrt{4!}} d_1(\omega_b) d_1(\omega_c) d_1(\tilde{\omega}_b) d_1(\tilde{\omega}_c) |\tilde{\psi}_{out}\rangle|^2, \tag{3.7}$$

where we introduced the annihilation operators $d_1(\omega)$ and $d_2(\omega)$ for both upper and lower channel respectively, the detected frequencies $\omega_b, \omega_c, \tilde{\omega}_b, \tilde{\omega}_c$, and the normalised output state $|\tilde{\psi}_{out}\rangle = |\psi_{out}\rangle / \langle \psi_{out}|\psi_{out}\rangle$. Expressions in Eq (3.5), Eq.(3.6) and Eq.(3.7) represent hence the probability P_{mn} to detect m photons in the upper channel and n photons in the lower channel. These formulas will be our start point for comparing our theoretical simulation with the experimental results. As a start point, in the next section we will employ these formulas in an artificial model, where the JSA is roughly represented as a double-gaussian function. This will give us an analytical estimation of the coincidence probability, partially anticipating the results of our rigorous formalism. Afterwards, we will make explicit any connections between the spectral features of the PDC and HOM curve.

3.1.2 Double Gaussian JSA: an analytical expression for P_{22}

Although a precise and detailed description of the interference scheme would let us achieve outcomes directly comparable with the experimental results, it can be more convenient to firstly address the problem with a pure analytical approach by reasonably reducing the complexity of the system. This choice both provides a visual interpretation of all steps and makes the role of all parameters more clear and evident.

A smart way to attempt an analytical calculation is via simplifying the phase matching function drastically, thereby annulling the dependence on the refractive indices and explicitly calculating P_{22}. In particular, the approach we are going to utilize makes use of a double gaussian expression for the JSA, holding the exponential trend of the pump laser function but converting the sinc function to an exponential as following:

$$F(\omega_s, \omega_i) = e^{-a^2(\omega_s + \omega_i - \omega_p)^2} e^{-b^2(\omega_s - \omega_i)^2}, \tag{3.8}$$

where $a = t_0/\sqrt{2}$ contains the pulse duration t_0, whereas b is connected with the length of the waveguide L and other technical parameters of the PDC. It is immediately evident that such expression cannot describe a realistic PDC process, however this is a good approximation, since Eq.(3.8) can take different shapes, similarly to the real JSA of the PDC. It is opportune to state that, in contrast to the real JSA, this model cannot reproduce the asymmetry along the $\omega_s = \omega_p - \omega_i$ diagonal of the single mode regime of the

PDC in ppKTP waveguide in Fig.2.3a, which was fundamental in the description of the two-photon HOM interference in Section 2.2.2.

Nevertheless, the new JSA in Eq.(3.8) drastically simplifies the analytical complexity of the photon state. In addition, it also leads to a reduction of the amount of information concerning the interferometer. As already elaborated in Section 2.2.2, we can merely suppose to have generated two photon pairs having already identical polarization and let them interfere in a balanced BS. According to these considerations, the expression describing the output state of the BS transformation is:

$$\begin{aligned} |\psi_{out}\rangle = \frac{1}{4}\int & d\omega_s d\omega_i d\bar{\omega}_s d\bar{\omega}_i F(\omega_s,\omega_i)F(\bar{\omega}_s,\bar{\omega}_i)e^{i\omega_s\tau + i\bar{\omega}_s\tau}\left[a_1^\dagger(\omega_s) - a_2^\dagger(\omega_s)\right] \\ & \times\left[a_2^\dagger(\omega_i) - a_1^\dagger(\omega_i)\right]\left[a_1^\dagger(\bar{\omega}_s) - a_2^\dagger(\bar{\omega}_s)\right]\left[a_2^\dagger(\bar{\omega}_i) - a_1^\dagger(\bar{\omega}_i)\right]|0\rangle, \end{aligned} \tag{3.9}$$

where τ is the time delay experienced by photons in one of the two arms of the interferometer before the BS due to a phase modulator. By inserting this state in Eq.(3.5) we finally obtain explicitly the probability to detect two photons in every channel[4]:

$$\begin{aligned} P_{22} = \int d\omega_b d\omega_c d\bar{\omega}_b d\bar{\omega}_c \Big| & F(\omega_b,\omega_c)F(\bar{\omega}_b,\bar{\omega}_c)e^{i(\omega_b+\bar{\omega}_b)\tau} + F(\bar{\omega}_b,\omega_c)F(\omega_b,\bar{\omega}_c)e^{i(\omega_b+\bar{\omega}_b)\tau} \\ & -F(\omega_b,\omega_c)F(\bar{\omega}_c,\bar{\omega}_b)e^{i(\omega_b+\bar{\omega}_c)\tau} - F(\bar{\omega}_b,\omega_c)F(\bar{\omega}_c,\omega_b)e^{i(\bar{\omega}_b+\bar{\omega}_c)\tau} \\ & -F(\omega_b,\bar{\omega}_c)F(\omega_c,\bar{\omega}_b)e^{i(\omega_b+\omega_c)\tau} - F(\bar{\omega}_b,\bar{\omega}_c)F(\omega_b,\omega_c)e^{i(\bar{\omega}_b+\omega_c)\tau} \\ & -F(\omega_b,\bar{\omega}_b)F(\omega_c,\bar{\omega}_c)e^{i(\omega_b+\omega_c)\tau} - F(\bar{\omega}_b,\omega_b)F(\omega_c,\bar{\omega}_c)e^{i(\bar{\omega}_b+\omega_c)\tau} \\ & -F(\omega_b,\bar{\omega}_b)F(\bar{\omega}_c,\omega_c)e^{i(\omega_b+\bar{\omega}_c)\tau} - F(\bar{\omega}_b,\omega_b)F(\bar{\omega}_c,\omega_c)e^{i(\bar{\omega}_b+\bar{\omega}_c)\tau} \\ & +F(\omega_c,\omega_b)F(\bar{\omega}_c,\bar{\omega}_b)e^{i(\omega_c+\bar{\omega}_c)\tau} + F(\bar{\omega}_c,\omega_b)F(\omega_c,\bar{\omega}_b)e^{i(\bar{\omega}_c+\omega_c)\tau}\Big|^2. \end{aligned} \tag{3.10}$$

This expression consists of 144 terms, but fortunately, taking advantage of the symmetry of the JSA in Eq.(3.8) with respect to the frequency axes, namely $F(\omega_s,\omega_i) = F(\omega_i,\omega_s)$, it turns out that most of them are identical. Moreover, the simplified mathematical expression of the JSA allows us to solve the integrals of the JSA analytically, so that we can finally calculate and normalize the probability obtaining:

$$P_{22} = \frac{3}{8}\left(e^{-\frac{\tau^2}{4b^2}} + 1\right) - \frac{(a^2+b^2)e^{-\frac{\tau^2}{8b^2}}}{4(a+b)^2} - \frac{ab}{2(a+b)^2}\left(e^{-\frac{\tau^2}{4(a^2+b^2)}} + 2e^{-\frac{(a^2+3b^2)\tau^2}{16b^2(a^2+b^2)}}\right). \tag{3.11}$$

Although the validity of this formula mainly holds in the multimode regime, it describes the coincidence probability profile P_{22} very well, and already enables the knowledge of some results, for instance the connection between the position of the point at zero time delay and the spectral features of the PDC.

In Section 2.1.3 it was mentioned that the amount of correlations between signal and idler photons determine the separability of the quantum state in the product of two substates; in other words, a separable state denotes lack of correlation. In Eq.(3.8) this can be easily achieved by imposing $a = b$. As a consequence, at $\tau = 0$ this would

---

[4] The expression still needs to be normalized.

reduce the P_{22} to 0.25. On the other hand, a state denoting high correlation, namely a high number of spectral modes, is not separable. This behaviour is emulated by our model via assuming $a \gg b$, namely reproducing a narrow JSA oriented along the signal-idler antidiagonal in the frequency axes. In this condition, a straightforward calculation provides $P \approx 1/2 = 0.5$, which is higher than what is observed in the no-interaction region ($\tau \gg 0$), namely $P = 3/8 = 0.375$. This demonstrates the presence of an antibunching peak in the coincidence probability. These considerations will be described formally along the next sections within our rigorous model.

3.1.3 Spectral and temporal engineering

In Section 2.1.3 it was seen that by properly manipulating some parameters, in particular the pulse duration of the pump laser and the length of the waveguide, we can control the profile of the coincidence probability. Starting from this chapter, we want to implement this framework, showing that an increasing number of interacting photons offers more prospectives of interference manipulation: in the end of this section we will demonstrate an unequivocal connection between the amount of correlation between signal and idler photons and the relative HOM profile.

As a start point, let us define three states A, B and C, shown in Fig.3.2, characterized by a different number of spectral modes. More experimental details concerning these states are listed in Appendix A, in Table A.1.

State A is characterized by a quasi-circular JSI, and in accord with our analysis in Section 2.1.3, the Schmidt number, i.e. the effective number of spectral modes, is close to one. Such state is quasi-separable, meaning that there is almost no frequency entanglement between signal and idler photons; furthermore, such photons are also typified by a low degree of spectral correlations, namely a frequency identification of one of them does not provide any information about the other. We stressed that the JSI is "quasi-circular" and not purely "circular": it is an important detail about the JSI that will be used along this chapter.

State B is experimentally achieved by state A via dramatically decreasing the pump bandwidth by increasing of the pulse duration. The shape of the JSA changes drastically: it is strongly pressed along the $\omega_s - \omega_i$ anti-diagonal, and thus it presents a high degree of spectral anti-correlations between signal and idler photons, which increases the Schmidt number.

In order to enhance further the number of Schmidt modes and define the state C, we opt for another strategy. Indeed, rather than increasing further the pulse duration, we keep the same spectral shape of state A, but provide the pump laser with an additional quadratic phase, modifying thus only the pump function $\alpha(\omega_s, \omega_i)$ [45, 121]. The JSA for this state C is given by:

$$\bar{F}(\omega_s, \omega_i) = F(\omega_s, \omega_i) e^{iD(\omega_s + \omega_i - \omega_p)^2}, \tag{3.12}$$

where D is a constant. It is clear that the presence of this quadratic phase does not affect the JSI, which is spectrally identical to the state A. Nevertheless, by using this trick we are able to drastically increase both the number of Schmidt modes and the symmetry of the JSI in the frequency domain. In order to distinguish the state A from the state B

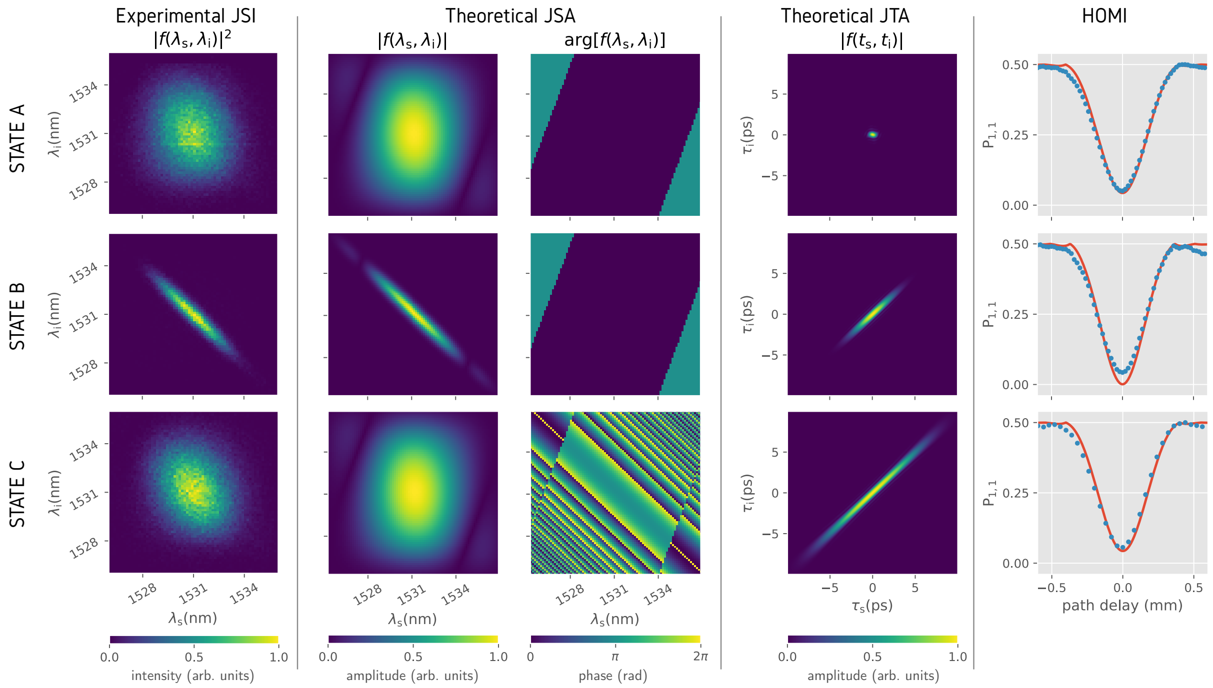

Figure 3.2: Spectral-temporal properties of considered PDC states: state A is a nearly decorrelated, state B is a standard frequency anti-correlated, and state C has spectral phase anti-correlations from a strongly chirped pump. The first column presents measured joint spectral intensity (JSI) which contains no information about the spectral phase. The second column depicts the absolute value and the phase of theoretical joint spectral amplitudes (JSAs). The third column is the absolute value of theoretical joint temporal amplitudes (JTAs). The fourth column shows the calculated (red solid line) and measured (blue dots) two-photon Hong-Ou-Mandel intereference (HOMI), with error bars smaller than the dots. Experimental points on $P_{1,1}$ correspond to two-fold coincidences between detectors 1 and 3, with maximum count rates of 1590426, 1583615, and 1675548 per 60s for states A, B, and C, respectively [1].

and highlight the higher degree of correlation of signal and idler photons in the temporal domain, we plot the Fourier transformation of the JSA in the third column of Fig.3.2, obtaining the joint temporal amplitude JTA:

$$F(t_s, t_i) = \int \mathrm{d}\omega_s \mathrm{d}\omega_i F(\omega_s, \omega_i) e^{i(\omega_s t_s + \omega_i t_i)}. \tag{3.13}$$

From this picture it seems clear that the joint temporal intensity JTI changes, becoming intensely diagonal along the $t_s - t_i$ axis. The modification of the JTA causes a further increase of the Schmidt number with respect to the state B, proving that this technique enables the control of the correlation between signal and idler photon without altering the spectral profile. The realization of the states A, B and C is quite worthy for our purpose: it allows us to clearly individuate the causes of any modification of the coincidence probabilities, testing individually the symmetry of the JSA and the correlations.

Before presenting the results concerning the four-photons HOM interference, we show the predicted and observed results about the two-photon HOM interference in the last column of Fig. 3.2. As it was already discussed in Section 2.2.2, since we fixed the waveguide length, the influence of the spectral features of the PDC to the HOM curves is restricted to the JSA symmetry along the signal-idler diagonal. Indeed, for state B the HOM dip reaches zero at zero delay, as expected from the use of a strongly symmetrical JSA, whereas the non-perfect circular shape of the JSA in state A and C leads to a non-vanishing coincidence probability, due to the partial spectral distinguishability of signal and idler photons. This certainly excludes the influence of the temporal correlations on the coincidence probability in the two-photon scenario.

3.1.4 Schmidt number and antibunching profile

The states A, B and C defined above constitute the input set of states of our interferometer. In order to test the influence of the spectral/temporal properties of the photon source to the HOM profile, we calculate the probabilities to measure a certain amount of photon per channel via Eq.(3.5), Eq.(3.6) and Eq.(3.7). These probabilities, plotted in Fig. 3.3, display a drastically different scenario with respect to the well-known two photon interference.

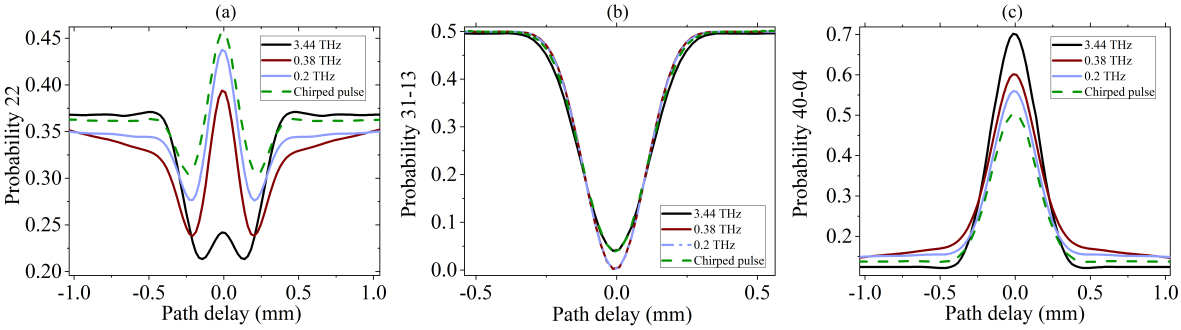

Figure 3.3: Theoretical coincidence probabilities to detect: (a) two photons per channel, (b) three photons in one channel and one photon in the other channel, (c) four photons in one channel for different pump spectral bandwidth (state A, B and C are presented by black, red and dashed green curves respectively) [1].

Let us consider firstly Fig.3.3a, where the probability P_{22} is plotted. The picture shows how such probability behaves by varying both the bandwidth and the temporal characterization of the pump profile. As it was mentioned in the previous section, the alteration of the pump profile gives rise to a variation of the Schmidt number. For instance, the black curve, obtained by state A, is characterized by a Schmidt number K=1.11, namely close to unity, and shows a bunching dip in the coincidence probability. Instead, the increase of correlations (higher Schmidt number), induced by either a reduction of the pump bandwidth (state B and blue line in Fig.3.3a) or by the use of a phased pump (state C) , lets this probability experience an antibunching behaviour. This univocally determines a link between the probability P_{22} and the amount of temporal correlations, keeping any connection with the shape of the JSA profile out. This theoretical prediction finds experimental confirmations in Fig.3.4, where the setup sketched in Fig.A.1 of Appendix A was utilized to measure the photon counts for all three states.

In order to analytically demonstrate how this peak depends on the Schmidt number, we calculated explicitly P_{22} for zero delay, similarly to Section 3.1.2, observing that most

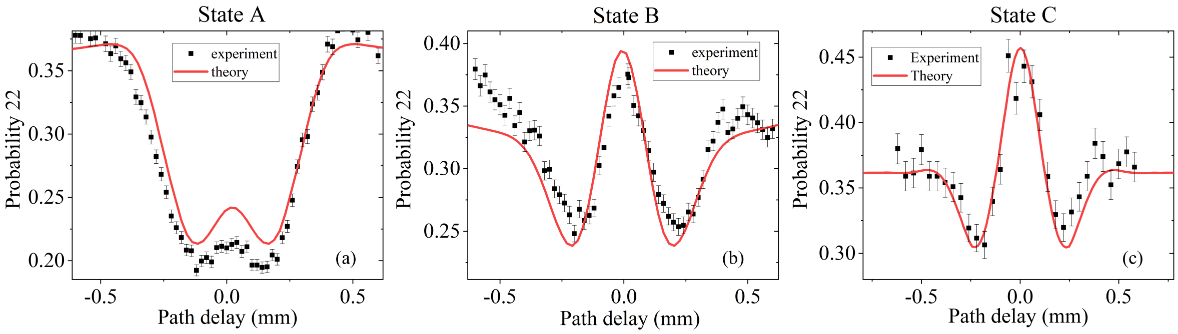

Figure 3.4: Theoretical and experimental P_{22} probabilities for states A, B, and C. Experimental points correspond to maximum counting rates of 3761, 2127, and 2309 per 60s for states A, B, and C, respectively [1].

of its 144 elements cancel each other out, so the final probability drastically reduces to:

$$P_{22} = \frac{\int d\omega_b d\omega_c d\tilde{\omega}_b d\tilde{\omega}_c F(\omega_c,\omega_d)F(\tilde{\omega}_c,\tilde{\omega}_d)F^*(\omega_d,\omega_c)F^*(\tilde{\omega}_d,\tilde{\omega}_c)}{2+2\int d\omega_b \mathrm{d}\omega_c d\tilde{\omega}_b d\tilde{\omega}_c F(\omega_c,\omega_d)F(\tilde{\omega}_c,\tilde{\omega}_d)F^*(\omega_d,\tilde{\omega}_c)F^*(\tilde{\omega}_d,\omega_c)}. \tag{3.14}$$

One way to simplify this expression is via assuming to have a symmetrical JSA $F(\omega_s,\omega_i) = F(\omega_i,\omega_s)$. This approximation holds because the JSA is strongly diagonal along the frequency axes $\omega_s = \omega_p - \omega_i$. By performing the Schmidt decomposition of the JSAs in this formula, $F(\omega_s,\omega_i) = \sum_n \sqrt{\Lambda_n} u_n(\omega_s)v_n(\omega_i)$, where Λ_n are eigenvalues, u_n and v_n are eigenfunctions of the Schmidt decomposition with respect to signal and idler photons respectively, we can immediately notice that the term in numerator tends to one, due to the normalization of the Schmidt eigenfunctions. On the other hand, the term in denominator can be expressed in terms of eigenvalues and eigenfunctions:

$$\int d\omega_b d\omega_c d\tilde{\omega}_b d\tilde{\omega}_c F(\omega_c,\omega_d)F(\tilde{\omega}_c,\tilde{\omega}_d)F^*(\omega_d,\tilde{\omega}_c)F^*(\tilde{\omega}_d,\omega_c) =$$
$$\sum_{\alpha\beta\gamma\delta} \sqrt{\Lambda_\alpha\Lambda_\beta\Lambda_\gamma\Lambda_\delta} \int d\omega_b d\omega_c d\tilde{\omega}_b d\tilde{\omega}_c u_\alpha(\omega_c)u_\beta(\tilde{\omega}_c)u^*_\gamma(\omega_d)u^*_\delta(\tilde{\omega}_d)v_\alpha(\omega_d)v_\beta(\tilde{\omega}_d)v^*_\delta(\omega_c)v^*_\gamma(\tilde{\omega}_c), \tag{3.15}$$

and taking advantage of the symmetry of the JSA we can assume that signal and idler photons have identical spectra and also $v \equiv u$, thereby using the orthonormality of the eigenfunctions:

$$\sum_{\alpha\beta\gamma\delta} \sqrt{\Lambda_\alpha\Lambda_\beta\Lambda_\gamma\Lambda_\delta}\delta_{\alpha\delta}\delta_{\beta\gamma}\delta_{\gamma\alpha}\delta_{\delta\beta} = \sum_k \Lambda_k^2. \tag{3.16}$$

The final probability can be finally expressed in terms of Schmidt eigenvalues:

$$P_{22} = \frac{1}{2+2\sum_n \Lambda_n^2}, \tag{3.17}$$

or in terms of Schmidt number

$$P_{22} = \frac{K}{2+2K}. \tag{3.18}$$

This formula proves that, by varying the Schmidt number, the probability P_{22} reaches 1/4 in the decorrelated single mode regime and 1/2 in the multimode regime, as predicted by our heuristic model in Section 3.1.2.

In order to exclude the dependence of P_{22} on the JSA shape beyond any doubts, a further (blue) curve in Fig.3.3a is plotted, showing the HOM curve generated by a state having pump bandwidth equal to 0.2 THz, even smaller than in state B. Comparing this blue line with the green dashed one, a similar antibunching behaviour is observed, although the JSI of the state described by the blue line would be more similar to state B, than C (or A). This highlights that there is no direct relation between JSA symmetry and antibunching peak.

Although our former argumentations seem to underestimate the link between the four-photon HOM and the JSA symmetry, this actually gains a fundamental relevance in P_{3113}. As shown in Fig. 3.3b, we can find a very interesting analogy between this probability and the ordinary P_{11} of the typical two-photon HOM interference. Indeed, as expected in the latter case, as long as the JSA is asymmetrical along the frequency diagonal (state A and C), P_{3113} does not reach zero due to the spectral distinguishability of signal and idler photons, whereas in both state B and the further theoretical state in blue line, a vanishing probability is observed.

Before concluding, we observe that $P_{4004} < 0.75$ in Fig. 3.3c, meaning that the so-structured interferometer cannot detect pure NOON state and post selection strategies would eventually be required.

3.1.5 Unbalanced beam splitter

Our argumentation above was prepared within a typical HOM framework, where a balanced beam splitter is utilized. Historically, the choice of a balanced BS was reasonably supported by the possibility to annul the coincidence probability P_{11} in the typical two-photon interference. However, although the choice of a balanced BS let us achieve fundamental informations in the four-photon interference (amply discussed above), one may also investigate a linear BS transformation which could annul P_{22} rather than P_{3113} when $\delta l = 0$. In order to get the corresponding values of the BS transmission and reflection coefficients which would annul P_{22}, we can exploit a simplest scenario, namely the interference of four plane waves in a BS when $\delta l = 0$. In this case, the output state is [122]:

$$\begin{aligned} |\psi_{afterBS}\rangle &= \sqrt{6}TR(|4_1, 0_2\rangle + |0_1, 4_2\rangle) \\ +\sqrt{6}TR(T-R)(|3_1, 1_2\rangle - |1_1, 3_2\rangle) &+ [(T-R)^2 - 2TR]|2_1, 2_2\rangle, \end{aligned} \tag{3.19}$$

where T and R are respectively the transmission and reflection coefficients of the BS. From this expression, it is clear why $P_{3113} = 0$ in case of balanced BS (T=R), moreover, by annulling the coefficient in front of $|2_1, 2_2\rangle$ and imposing at the same time that $R+T = 1$, we find that $T = (3+\sqrt{3})/6$ and R=$(3-\sqrt{3})/6$ (or viceversa). Within the framework of four-photon HOM interference via plane wave modes, this set of coefficients allows to achieve $P_{22} = 0$.

In our spectrally multimode scenario, we plot the probabilities in Fig.3.5 by setting the BS parameters calculated above. As expected, the new profiles look very different from the balanced BS case investigated in the last section. For instance, we notice that P_{22} can be drastically inhibited by reducing the amount of correlations, but we can not annul it though, because of the asymmetry of the JSA. This demonstrated that P_{22} is still strongly affected by the number of Schmidt modes, and in particular, stronger correlations between signal and idler photons break the similarity with the behaviour expected in case of plan wave modes. According to these results, even this specific set of T and R is not sufficient to annul P_{22}. This behaviour is experimentally confirmed in Fig.3.6, where results concerning the state A and C are compared with the theoretical ones.

Moreover, consequent changes are also observed in P_{3113} and P_{4004}. It is interesting to notice that the new choice of R and T modifies drastically P_{3113}, making its shape strongly dependent on the number of modes. One the other hand, P_{4004} keeps the same profile but reduces drastically the intensity with respect to the balanced case.

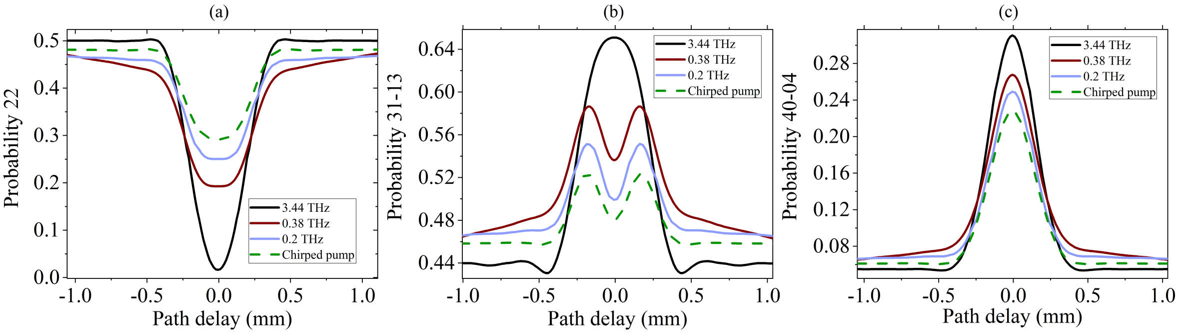

Figure 3.5: Unbalanced BS configuration. Theoretical coincidence probabilities to detect: (a) two photons per channel, (b) three photons in one channel and one photon in the other channel, (c) four photons in one channel for different pump spectral bandwidth (state A, B and C in black, red (dark gray) and dashed green respectively) [1].

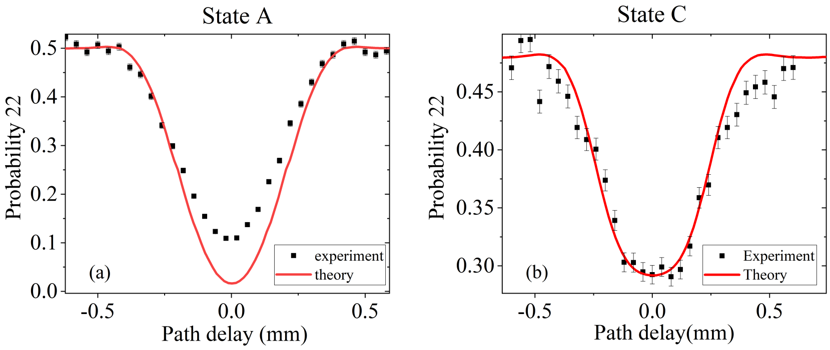

Figure 3.6: Theoretical and experimental P_{22} probabilities for states A, and C in the unbalanced BS configuration. Experimental points correspond to maximum counting rates of 5128 and 2094 per 60s for states A and C, respectively [1].

Finally the new profile of P_{22} in Fig.3.5a reminds the typical two-photon HOM dip of the P_{11} interference when a balanced BS set, and the comparison between such two probabilities is presented in Fig. 3.7. Here we can observe that the two profiles are extremely similar, though the dip of P_{22} is actually 7.5% broader with respect to P_{11}.

This makes P_{22} slightly less sensitive to the distinguishability of signal and idler spectra with respect to P_{11}.

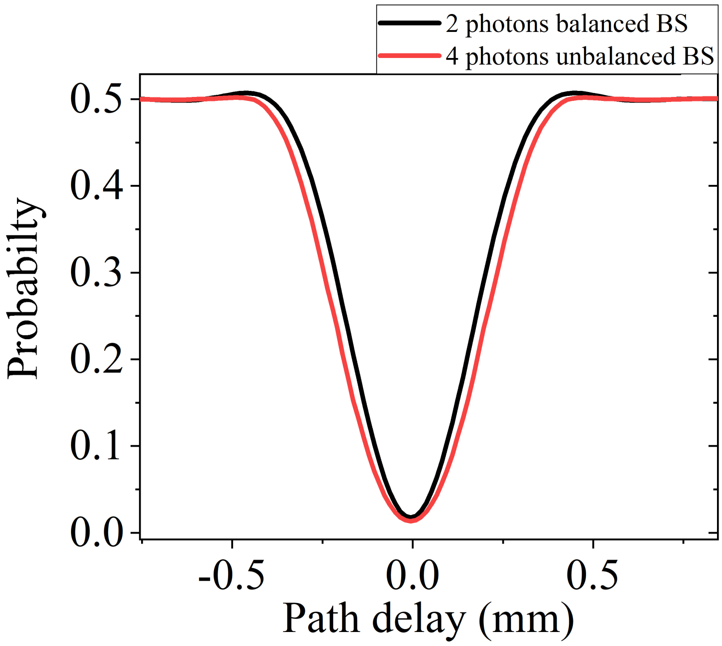

Figure 3.7: The two-photon HOM dip with a balanced BS and the four-photons HOM dip with an unbalanced BS in the single-mode regime: the pulse duration is 0.29 ps [1].

3.1.6 Conclusion

In this first section we designed the four-photon interference in a framework where the temporal correlations of the photon sources are taken into account. The four photons were generated by highly pumping the laser into a ppKTP waveguide, triggering the second order PDC effect and generating two photon couples. The scheme of the interferometer used along the chapter ensured the indistinguishability of photons in terms of polarization and allowed to investigate the coincidence probabilities for different time delays. The connection between the coincidence probability P_{22} and number of spectral/temporal modes was firstly estimated by making use of a simplified model, in which the JSA is sketched as a double-Gaussian function, afterwards, we prepared three states characterized by both specific JSA/JSI profiles and number of spectral modes. Hence, the connection between probability and Schmidt number was proven both theoretically and experimentally, showing that P_{22} runs from 0.25 to 0.5 by increasing the number of spectral mode, and an antibunching peak in the coincidence probability is observed. On the other hand, the role of the symmetry of the JSA merely concerns P_{3113}: the more symmetrical the JSA with respect to the frequency diagonal, the closer P_{3113} is to zero.

The flexibility of our scheme enables further interesting tests. For instance, we can try to make the profile of P_{22} similar to the two-photon coincidence probability P_{11} by altering the transmission and reflection parameters of the BS. A proper set of T and R turns the probability P_{22} to a dip curve. Similarly to P_{11}, the four photon probability P_{22}

cannot reach zero because the JSA lacks a symmetrical behaviour along the frequency antidiagonal. Furthermore, the presence of correlations causes a reduction of the visibility.

3.2 Spatial entanglement and four-photon Bell states

3.2.1 Maximization of the spatial entanglement

In the first part of this chapter we focused on the influence of the temporal Schmidt modes in the four photon interference, demonstrating theoretically how the Schmidt number is related to the coincidence probability. Vice versa, we can say that an antibunching behaviour of the coincidence probability is symptomatic of quantum correlations between the interacting photons.

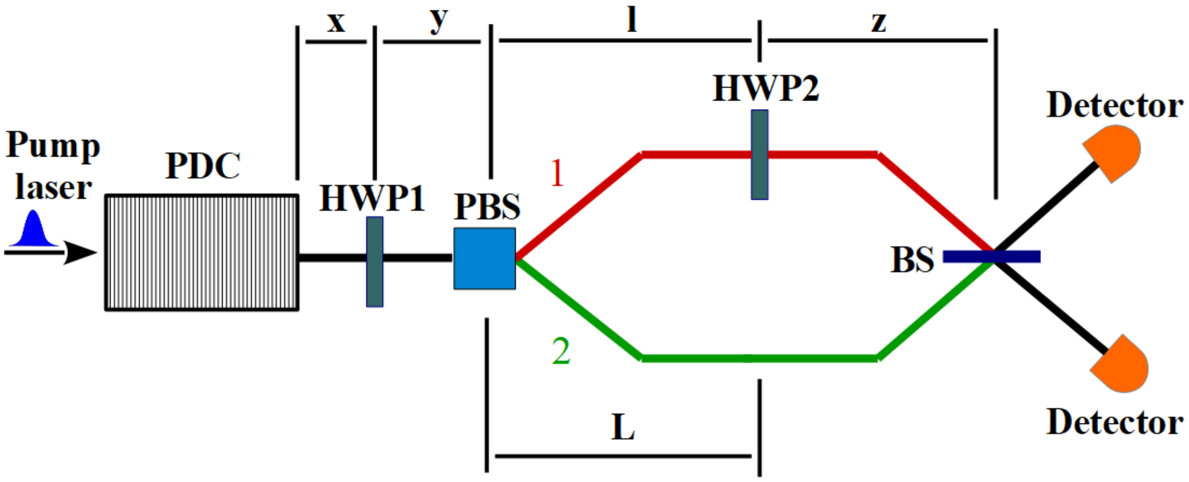

Figure 3.8: Schematic setup. Four photons are generated in the PDC section. For every photon, a first half-wave plate, HWP_1 creates a superposition of the vertical and the horizontal polarizations. A polarization beam slitter routs vertically and and horizontally polarized photons in two different spatial channels (red and green). The second half-wave plate, HWP_2, rotates the polarization in the first channel, such that all photons own the same polarization. A path length of the second channel compensates arising time delay between the signal and idler photons $L = l + \Delta l$. Finally, all photons interact in a beam splitter and are detected [2].

In this second part we want to investigate the consequence of the spatial entanglement between the two arms of the interferometer on the coincidence probabilities in Eqs.(3.5-3.7) [2]. The spatial entanglement can be triggered in the interferometer by performing a polarization rotation. To contextualise better what we plan to do, we show in Fig.3.8 the latest version of our interferometer, where a further HWP was added between the PDC section and the PBS [56]. As it can be seen, as long as the HWP is switched off (namely the converting parameter is equal to zero), this interferometer is indistinguishable from the one in Fig.3.1, and thus no additional information could be obtained. An identical scenario would be achieved if the new HWP perfectly converted the polarization of all signal and idler photons (the conversion parameter in this case would correspond to $\pi/2$), since a polarization switching would not influence the physics behind the interference process.

In order to explore new effects beyond the previous model, the choice of a converting parameter in some intermediate value between 0 and $\pi/2$ seems to be more tempting; this leads to a partial conversion of the polarization of signal and idler photons. The quantum state leaving the first HWP is therefore characterized by a superposition of vertical and horizontal polarized photons. When such state enters the PBS, this triggers the spacial entanglement by spatially separating not different polarized photons, but vertical from horizontal polarized parts of the same photon, for every signal and idler photon pair. In other words, if in the previous scheme we are able to distinguish signal and idler photons because of their polarization, in this scheme we have parts of the same photons in both channels.

In order to seek the proper converting parameter and optimize the amount of spatial entanglement in the interferometer, we start from the Hamiltonian in Eq.(3.1) and the new unitary transformation:

$$U = BS \cdot FP_3 \cdot HWP_2 \cdot FP_2 \cdot PBS \cdot FP_1 \cdot HWP_1 \cdot FP_0, \tag{3.20}$$

which differs from Eq.(3.2) because of the additional HWP_1 matrix describing the further HWP. As in the previous chapter, the action of the matrix U on the PDC state in the low gain regime yields the output state of the interferometer. Since the spatial entanglement occurs within the interferometer and not in the output, it seems more reasonable to firstly consider the quantum state inside the interferometer, namely before the beam splitter $|\psi_{beforeBS}\rangle$. The unitary transformation necessary to achieve this state clearly corresponds to Eq.(3.20) without the beam splitter matrix. Hence, the state inside the interferometer is:

$$|\psi_{beforeBS}\rangle = |\psi_{beforeBS}(22)\rangle + |\psi_{beforeBS}(4004)\rangle + |\psi_{beforeBS}(3113)\rangle, \tag{3.21}$$

where

$$\begin{aligned} |\psi_{beforeBS}(22)\rangle = \int & \mathsf{d}\omega_s \mathsf{d}\omega_i \mathsf{d}\tilde{\omega}_s \mathsf{d}\tilde{\omega}_i F(\omega_s,\omega_i) F(\tilde{\omega}_s,\tilde{\omega}_i) e^{i(\omega_s+\omega_i+\tilde{\omega}_s+\tilde{\omega}_i)(x+y+l)/c} \\ & \times \Big[- a_2^\dagger(\omega_s) a_1^\dagger(\omega_i) a_2^\dagger(\tilde{\omega}_s) a_1^\dagger(\tilde{\omega}_i) \sin^4\phi_1 e^{i(\omega_s+\tilde{\omega}_s)\frac{\Delta l}{c}} \\ & + a_2^\dagger(\omega_s) a_1^\dagger(\omega_i) a_1^\dagger(\tilde{\omega}_s) a_2^\dagger(\tilde{\omega}_i) \sin^2\phi_1 \cos^2\phi_1 e^{i(\omega_s+\tilde{\omega}_i)\frac{\Delta l}{c}} \\ & + a_1^\dagger(\omega_s) a_1^\dagger(\omega_i) a_2^\dagger(\tilde{\omega}_s) a_2^\dagger(\tilde{\omega}_i) \sin^2\phi_1 \cos^2\phi_1 e^{i(\tilde{\omega}_s+\tilde{\omega}_i)\frac{\Delta l}{c}} \\ & + a_2^\dagger(\omega_s) a_2^\dagger(\omega_i) a_1^\dagger(\tilde{\omega}_s) a_1^\dagger(\tilde{\omega}_i) \sin^2\phi_1 \cos^2\phi_1 e^{i(\omega_s+\omega_i)\frac{\Delta l}{c}} \\ & + a_1^\dagger(\omega_s) a_2^\dagger(\omega_i) a_2^\dagger(\tilde{\omega}_s) a_1^\dagger(\tilde{\omega}_i) \sin^2\phi_1 \cos^2\phi_1 e^{i(\omega_i+\tilde{\omega}_s)\frac{\Delta l}{c}} \\ & - a_1^\dagger(\omega_s) a_2^\dagger(\omega_i) a_1^\dagger(\tilde{\omega}_s) a_2^\dagger(\tilde{\omega}_i) \cos^4\phi_1 e^{i(\omega_i+\tilde{\omega}_i)\frac{\Delta l}{c}} \Big] |0\rangle, \end{aligned} \tag{3.22}$$

$$\begin{aligned}|\psi_{beforeBS}(4004)\rangle = \int & \mathsf{d}\omega_s \mathsf{d}\omega_i \mathsf{d}\tilde{\omega}_s \mathsf{d}\tilde{\omega}_i F(\omega_s,\omega_i)F(\tilde{\omega}_s,\tilde{\omega}_i)e^{i(\omega_s+\omega_i+\tilde{\omega}_s+\tilde{\omega}_i)(x+y+l)/c} \\ & \times\frac{\sin^2 2\phi_1}{4}\Big[a_1^\dagger(\omega_s)a_1^\dagger(\omega_i)a_1^\dagger(\tilde{\omega}_s)a_1^\dagger(\tilde{\omega}_i)+ \\ & a_2^\dagger(\omega_s)a_2^\dagger(\omega_i)a_2^\dagger(\tilde{\omega}_s)a_2^\dagger(\tilde{\omega}_i)e^{i(\omega_s+\omega_i+\tilde{\omega}_s+\tilde{\omega}_i)\frac{\Delta l}{c}}\Big]|0\rangle,\end{aligned} \tag{3.23}$$

$$\begin{aligned}|\psi_{beforeBS}(3113)\rangle = i\int & \mathsf{d}\omega_s \mathsf{d}\omega_i \mathsf{d}\tilde{\omega}_s \mathsf{d}\tilde{\omega}_i F(\omega_s,\omega_i)F(\tilde{\omega}_s,\tilde{\omega}_i)e^{i(\omega_s+\omega_i+\tilde{\omega}_s+\tilde{\omega}_i)(x+y+l)/c} \\ & \times\Big[-a_2^\dagger(\omega_s)a_1^\dagger(\omega_i)a_1^\dagger(\tilde{\omega}_s)a_1^\dagger(\tilde{\omega}_i)\sin^3\phi_1\cos\phi_1 e^{i\omega_s\frac{\Delta l}{c}} \\ & +a_1^\dagger(\omega_s)a_2^\dagger(\omega_i)a_2^\dagger(\tilde{\omega}_s)a_2^\dagger(\tilde{\omega}_i)\sin\phi_1\cos^3\phi_1 e^{i(\tilde{\omega}_s+\tilde{\omega}_i+\omega_s)\frac{\Delta l}{c}} \\ & -a_1^\dagger(\omega_s)a_1^\dagger(\omega_i)a_2^\dagger(\tilde{\omega}_s)a_1^\dagger(\tilde{\omega}_i)\sin^3\phi_1\cos\phi_1 e^{i\tilde{\omega}_s\frac{\Delta l}{c}} \\ & +a_2^\dagger(\omega_s)a_2^\dagger(\omega_i)a_1^\dagger(\tilde{\omega}_s)a_2^\dagger(\tilde{\omega}_i)\sin\phi_1\cos^3\phi_1 e^{i(\omega_s+\omega_i+\tilde{\omega}_s)\frac{\Delta l}{c}} \\ & +a_1^\dagger(\omega_s)a_2^\dagger(\omega_i)a_1^\dagger(\tilde{\omega}_s)a_1^\dagger(\tilde{\omega}_i)\sin\phi_1\cos^3\phi_1 e^{i\omega_i\frac{\Delta l}{c}} \\ & -a_2^\dagger(\omega_s)a_1^\dagger(\omega_i)a_2^\dagger(\tilde{\omega}_s)a_2^\dagger(\tilde{\omega}_i)\sin^3\phi_1\cos\phi_1 e^{i(\tilde{\omega}_s+\tilde{\omega}_i+\omega_i)\frac{\Delta l}{c}} \\ & +a_1^\dagger(\omega_s)a_1^\dagger(\omega_i)a_1^\dagger(\tilde{\omega}_s)a_2^\dagger(\tilde{\omega}_i)\sin\phi_1\cos^3\phi_1 e^{i\tilde{\omega}_i\frac{\Delta l}{c}} \\ & -a_2^\dagger(\omega_s)a_2^\dagger(\omega_i)a_2^\dagger(\tilde{\omega}_s)a_1^\dagger(\tilde{\omega}_i)\sin^3\phi_1\cos\phi_1 e^{i(\omega_s+\omega_i+\tilde{\omega}_i)\frac{\Delta l}{c}}\Big]|0\rangle,\end{aligned} \tag{3.24}$$

and where ϕ_1 is the converting parameter. These expressions can be rewritten in a more elegant and convenient way by introducing the set of Schmidt operators as in Eq.(2.36):

$$\begin{aligned}A_k^\dagger &= \int d\omega_s u_k(\omega_s)a^\dagger(\omega_s) \\ B_k^\dagger &= \int d\omega_i v_k(\omega_i)a^\dagger(\omega_i).\end{aligned} \tag{3.25}$$

and the set of path-depending Schmidt operators:

$$\begin{aligned}C_k^\dagger &= \int d\omega_s u_k(\omega_s)e^{i\omega_s\frac{\Delta l}{c}}a^\dagger(\omega_s), \\ D_k^\dagger &= \int d\omega_i v_k(\omega_i)e^{i\omega_i\frac{\Delta l}{c}}a^\dagger(\omega_i).\end{aligned} \tag{3.26}$$

It is clear that the path-depending operators in Eq. (3.26) converge to the set in Eq.(3.25) when $\delta l = 0$. By employing these set of operators, the three components of the output state before the BS are:

$$\begin{aligned}|\psi_{beforeBS}(22)\rangle = \sum_{k\tilde{k}}\sqrt{\lambda_k\lambda_{\tilde{k}}}\Big[& -C_{k_2}^\dagger B_{k_1}^\dagger C_{\tilde{k}_2}^\dagger B_{\tilde{k}_1}^\dagger\sin^4\phi_1 + C_{k_2}^\dagger B_{k_1}^\dagger A_{\tilde{k}_1}^\dagger D_{\tilde{k}_2}^\dagger\sin^2\phi_1\cos^2\phi_1 \\ & +A_{k_1}^\dagger B_{k_1}^\dagger C_{\tilde{k}_2}^\dagger D_{\tilde{k}_2}^\dagger\sin^2\phi_1\cos^2\phi_1 + C_{k_2}^\dagger D_{k_2}^\dagger A_{\tilde{k}_1}^\dagger B_{\tilde{k}_1}^\dagger\sin^2\phi_1\cos^2\phi_1 \\ & +A_{k_1}^\dagger D_{k_2}^\dagger C_{\tilde{k}_2}^\dagger B_{\tilde{k}_1}^\dagger\sin^2\phi_1\cos^2\phi_1 - A_{k_1}^\dagger D_{k_2}^\dagger A_{\tilde{k}_1}^\dagger D_{\tilde{k}_2}^\dagger\cos^4\phi_1\Big]|0\rangle,\end{aligned} \tag{3.27}$$

$$|\psi_{beforeBS}(4004)\rangle = \sum_{k\tilde{k}} \sqrt{\lambda_k \lambda_{\tilde{k}}} \sin^2\phi_1 \cos^2\phi_1 \Big[A^\dagger_{k_1} B^\dagger_{k_1} A^\dagger_{\tilde{k}_1} B^\dagger_{\tilde{k}_1} + C^\dagger_{k_2} D^\dagger_{k_2} C^\dagger_{\tilde{k}_2} D^\dagger_{\tilde{k}_2} \Big] |0\rangle, \tag{3.28}$$

$$\begin{aligned} |\psi_{beforeBS}(3113)\rangle = i \sum_{k\tilde{k}} \sqrt{\lambda_k \lambda_{\tilde{k}}} \\ \times \Big[- C^\dagger_{k_2} B^\dagger_{k_1} A^\dagger_{\tilde{k}_1} B^\dagger_{\tilde{k}_1} \sin^3\phi_1 \cos\phi_1 + C^\dagger_{k_1} B^\dagger_{k_2} C^\dagger_{\tilde{k}_2} D^\dagger_{\tilde{k}_2} \sin\phi_1 \cos^3\phi_1 \\ - A^\dagger_{k_1} B^\dagger_{k_1} C^\dagger_{\tilde{k}_2} B^\dagger_{\tilde{k}_1} \sin^3\phi_1 \cos\phi_1 + C^\dagger_{k_2} D^\dagger_{k_2} C^\dagger_{\tilde{k}_1} B^\dagger_{\tilde{k}_2} \sin\phi_1 \cos^3\phi_1 \\ + A^\dagger_{k_1} D^\dagger_{k_2} A^\dagger_{\tilde{k}_1} B^\dagger_{\tilde{k}_1} \sin\phi_1 \cos^3\phi_1 - A^\dagger_{k_2} D^\dagger_{k_1} C^\dagger_{\tilde{k}_2} D^\dagger_{\tilde{k}_2} \sin^3\phi_1 \cos\phi_1 \\ + A^\dagger_{k_1} B^\dagger_{k_1} A^\dagger_{\tilde{k}_1} D^\dagger_{\tilde{k}_2} \sin\phi_1 \cos^3\phi_1 - C^\dagger_{k_2} D^\dagger_{k_2} A^\dagger_{\tilde{k}_2} D^\dagger_{\tilde{k}_1} \sin^3\phi_1 \cos\phi_1 \Big] |0\rangle, \end{aligned} \tag{3.29}$$

We notice that most of these terms vanish either when $\phi_1 = 0$ or $\phi_1 = \pi/2$, confirming that these two scenarios are useless for triggering the spatial entanglement. The value of ϕ_1 we are looking for, maximises the degree of entanglement, which can thus be estimated by the Schmidt number. In case of spatial entanglement, in which we have a discrete number of spatial channels, this is $K = 1/Tr(\rho_r^2)$, where ρ_r is the reduced density matrix of the system. An explicit calculation of such matrix gives:

$$\rho_r = \begin{bmatrix} \frac{\cos^2\phi_1}{4}(5 - 2\cos 2\phi_1 + \cos 4\phi_1) & A(\phi_1, \Delta l) \\ A(\phi_1, \Delta l)^* & \frac{\sin^2\phi_1}{4}(5 + 2\cos 2\phi_1 + \cos 4\phi_1) \end{bmatrix}, \tag{3.30}$$

where

$$\begin{aligned} A(\phi_1, \Delta l) = \int \mathsf{d}\omega_s \mathsf{d}\omega_i \mathsf{d}\tilde{\omega}_s \mathsf{d}\tilde{\omega}_i \mid F(\omega_s, \omega_i) \mid^2 \mid F(\tilde{\omega}_s, \tilde{\omega}_i) \mid^2 \\ \times \Big[\sin^4\phi_1 \cos^4\phi_1 (e^{-i(\tilde{\omega}_s + \tilde{\omega}_i)\frac{\Delta l}{c}} + e^{-i(\omega_s + \omega_i)\frac{\Delta l}{c}}) \\ - \sin^2\phi_1 \cos^6\phi_1 e^{-i(\tilde{\omega}_s + \omega_i)\frac{\Delta l}{c}} - \sin^6\phi_1 \cos^2\phi_1 e^{-i(\omega_s + \tilde{\omega}_i)\frac{\Delta l}{c}} \\ - i \sin^5\phi_1 \cos^3\phi_1 e^{-i(\omega_s + \omega_i - \tilde{\omega}_i)\frac{\Delta l}{c}} + i \sin^7\phi_1 \cos\phi_1 e^{-i\tilde{\omega}_s \frac{\Delta l}{c}} \\ + i \sin^3\phi_1 \cos^5\phi_1 e^{-i(\tilde{\omega}_s + \tilde{\omega}_i - \omega_i)\frac{\Delta l}{c}} - i \sin\phi_1 \cos^7\phi_1 e^{-i\omega_s \frac{\Delta l}{c}} \Big], \end{aligned} \tag{3.31}$$

is a function that depends in principle on both the conversion parameter and path delay. However, as observed in Fig.3.9, the dependence on the path delay does not seem to condition the Schmidt number evidently. For the sake of clarity, this plot was realized assuming all frequency equal to $\omega_p/2$ and defining the optical phase $\varphi = \Delta l\ \omega_p/c$. Although this is a convenient approximation utilised just to plot the Schmidt number, it holds very well as long as $\Delta l \simeq 2\lambda_p$.

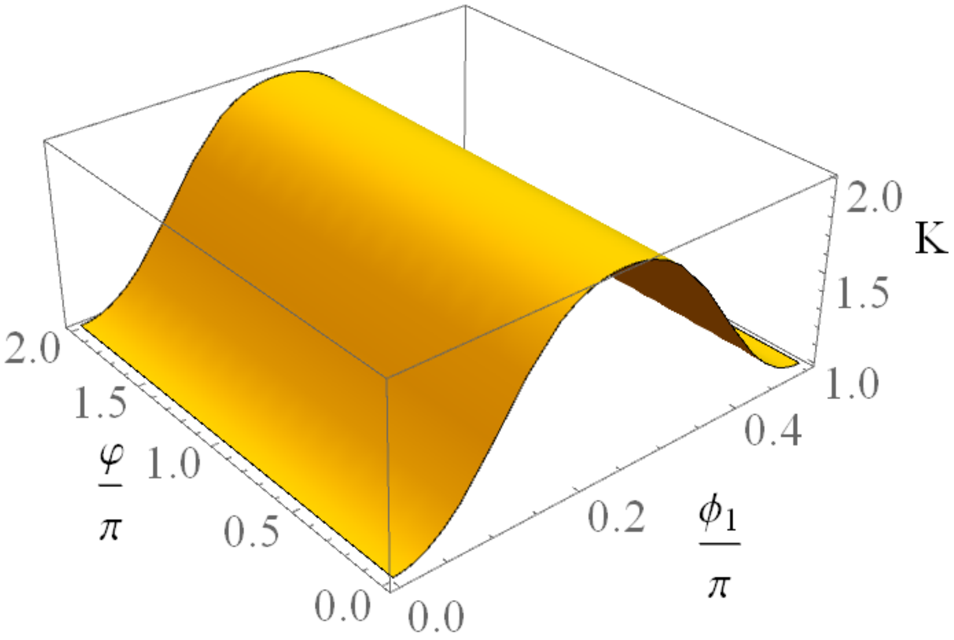

Figure 3.9: The Schmidt number K vs the conversion angle ϕ_1 and the optical phase $\varphi = \Delta L\ \omega_p/c$ [2].

Moreover we can fix $\Delta l = 0$, and the Schmidt number can be analytically calculated,

$$K(\phi_1) = \frac{128}{94 + 33\cos 4\phi_1 + 2\cos 8\phi_1 - \cos 12\phi_1}. \tag{3.32}$$

This function is maximized at $\phi_1 = \pi/4$, namely when the HWP_1 performs a half-conversion and all contributions in Eq.(3.27), Eq(3.28) and Eq.(3.29) gain the same weight. It should not look surprising that the maximal value reached by the Schmidt number is 2 for a bipartite system; a similar results was also observed in [56] for two photons. Anyway, this will be our start point for the next section, where the coincidence probabilities will be analysed.

3.2.2 Coincidence probabilities and structured oscillations

It was seen above that a further HWP can be exploited in order to maximise the spatial entanglement of the interferometer, and the best value of the conversion parameter was calculated. Now we can exploit the ansatz for estimating the coincidence probabilities, making use therefore of the full unitary transformation in Eq.(3.20). By applying the total matrix transformation of the interferometer on the initial PDC state, we gain the output state of the interferometer. The probabilities are therefore calculated by making use of Eq.(3.5), Eq.(3.6) and Eq.(3.7).

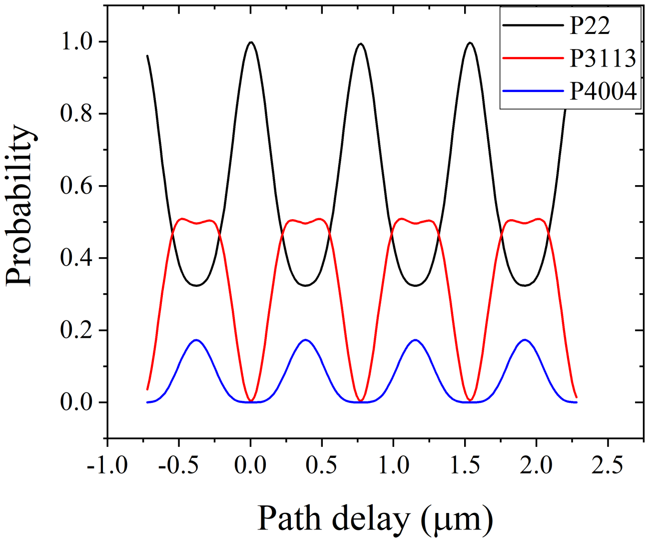

Figure 3.10: The zoom of the P_{22}, P_{3113} and P_{4004} probabilities around zero path delay. The PDC section length is $L = 8mm$, the pulse duration is $\tau = 0.29ps$, the pump wavelength is $\lambda_p = 766nm$ [2].

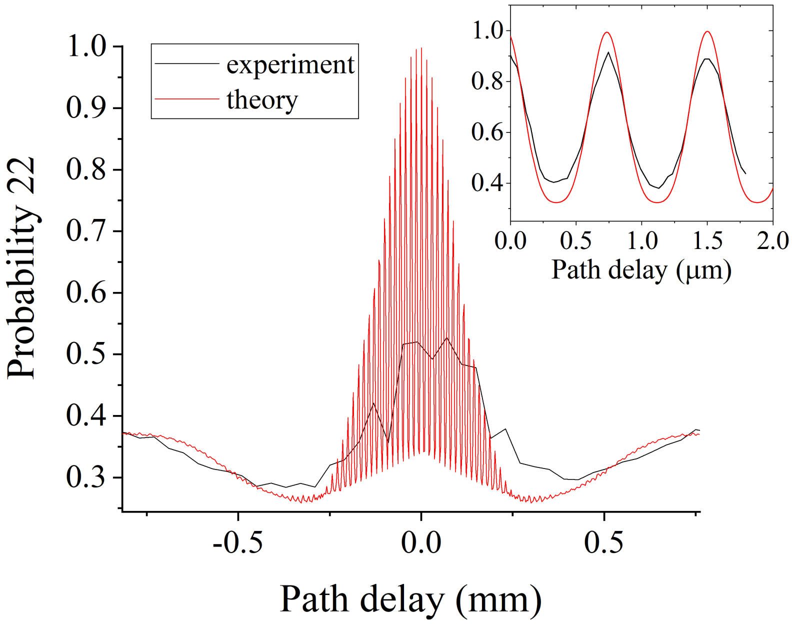

Figure 3.11: The probability to detect two photons in each channel for the conversion angle $\phi_1 = \pi/4$ in the single spectral mode regime. The red curve is theoretical calculations, while the black curve stands for the experimental data. The insert shows a zoom around zero time delay, namely the black curve in Fig.3.10 [2].

The interference pattern of all three probabilities in a small range around $\Delta l \approx 0$ is plotted in Fig.3.10, whereas both the whole trend and the fast oscillation around $\Delta l \approx 0$

of P_{22} were estimated and plotted both theoretically and experimentally[5] in Fig.3.11. The setup used to perform the measurements is described in Appendix B, whereas the experimental probability is calculated by the photon counts following the protocol described in Section 3.2.3. In these pictures, the effect of the spacial entanglement is evident: all probabilities are now characterized by oscillations with periodicity equal to λ_p and having a quite complex structure, not present in the previous set-up without HWP_1.

In order to understand better the structure of these oscillations in P_{22}, let us consider individually the contributions of Eq.(3.21), namely Eq.(3.27), Eq.(3.28) and Eq.(3.29), to the output probability. By letting these terms cross the beam splitter separately and calculating P_{22}, it can be seen that the first one, Eq.(3.27), yields the main trend of the curve without oscillation, whereas the fast fringes stem from Eq.(3.28) and Eq.(3.29). Although this strategy allows to decompose the contribution of Eq.(3.27), Eq.(3.28) and Eq.(3.29) to the coincidence probability, it does not clarify the structure of these oscillation fully.

Indeed, it turns out that Eq.(3.27) and Eq.(3.28) further interfere in the beam splitter, providing finally the structured oscillation shown in Fig.3.11 and this is due to the bosonic nature of light. To figure it out, we make use of a specific strategy: in one case we firstly let the contributions in Eq.(3.27), Eq.(3.28) and Eq.(3.29) cross the beam splitter individually, and then we sum them in pair (overlap); as a second case, we take directly pairs of them and calculate the interference in the beam splitter.

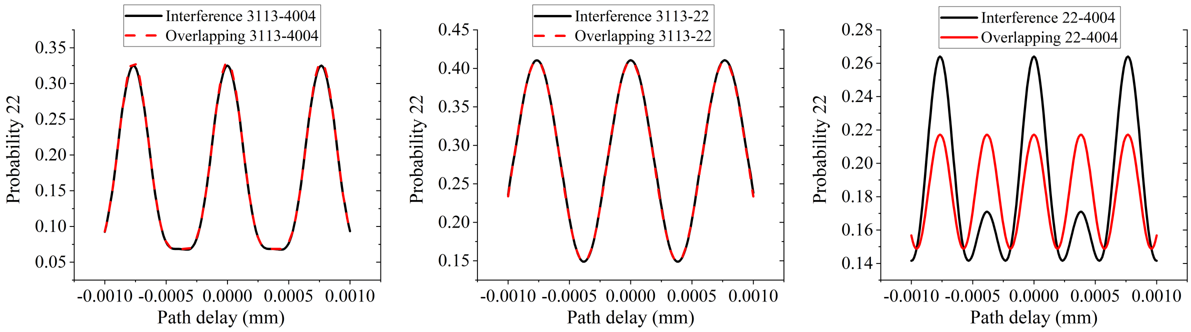

Figure 3.12: Comparison between the overlapping and the interference of Eq(3.27), Eq(3.28) and Eq(3.29) in the zero-delay region [2].

Results are plotted in Fig.3.12. This picture shows that an interference between Eq.(3.27) and Eq.(3.29) occurs, generating the peculiar oscillation given by the black curve in Fig.3.12c. This interference is caused by both the maximized spatial entanglement and the quantum nature of light. In the end of this chapter we will show that these oscillations can be manipulated by making the Schmidt mode of signal and idler indistinguishable.

---

[5] Although the oscillation is defined quite well in the insert, the experimental limitations did not allow us to reach the same precision in the larger range (see black curve in Fig.3.11). The main trend for $|\Delta l| \gg 0$ is however well depicted.

3.2.3 Normalization P_{22} probability

Along this chapter we had to deal with different set of experimental data, utilised for estimating coincidence probability P_{22}. Such experimental data, consisting of photon counts, had to be compared with the theoretical simulation. However, depending on which quantities we want to analyse as well as on which physical setup was exploited, the experimental data required a specific normalization strategy.

In case of Fig. 3.4 and Fig. 3.6, a simple way to compare the theoretical prediction with the data points consist merely of scaling the experimental curve with respect to the "infinity delay" line. Let us consider Fig. 3.6 as an example: it was theoretically known that the coincidence probability far from the interaction zone is 0.5 and this value is expected also experimentally. Hence, by opportunely rescaling the experimental counts with respect to 0.5 in the large delay zone, we were able to compare both width and visibility in the fully interaction zone. This method was satisfyingly employed for both Fig. 3.4 and Fig. 3.6.

However, due to the different experimental setup utilized to measure the coincidence probability P_{22} for $\delta l \gg 0$ and $\delta l \simeq 0$ in Fig. 3.11, a more complex normalization strategy was adopted. In particular, we need to find a way to connect these two experimental set of data and the theoretical simulation. Therefore, we start from Fig. B.1 in Appendix B, where we observe that the detection apparatus consists of two balanced beam splitters and a set of four detectors. We will indicate such detectors with A, B, C and D, coupling A and B (and therefore also C and D) in the same spatial channel. For any event, we have four photons crossing the PBS, which will be either distributed along the four channels, or lost. We indicate with c_{XY} the experimental number of coincidences between channel X and channel Y, and similarly we will do with c_{XYZ} and so on. These coincidences are connected with different quantities:

- total amount of generated photon;
- probability of one photon to not get lost due to losses effect;
- probability of one photon to leave one of the two channels of the PBS;
- probability of one photon to leave one of the two channels of the BS.

The third and the fourth quantities are known: the former were predicted theoretically along the text, whereas the latter stems from combinatorial considerations. Hence, from the experimental data we need to distinguish the amount of photons generated by the four-photon events from the two-photon, and estimate the loss rate. The latter can be simply modelled by assuming the loss effect described by additional beam splitters, whose transmission parameter η determines the probability to not loose the photon.

In order to exclude any influence of two-photon events, we are now able to write down and solve a couple of equations for c_{ABC} and c_{ABCD} in the far delay zone:

$$\langle c_{ABCD}(\delta l \gg 0)\rangle = \frac{1}{4}\eta^4 N_4 P_{22}^{th}; \tag{3.33}$$

$$\langle c_{ABC}(\delta l \gg 0)\rangle = N_4\left[\eta^4\left(\frac{3}{8}P_{13}^{th} + \frac{1}{8}P_{22}^{th}\right) + \eta^3(1-\eta)\left(\frac{1}{4}P_{13}^{th} + \frac{1}{4}P_{22}^{th}\right)\right], \tag{3.34}$$

where $P^{th}_{\alpha\beta}$ is the well-known theoretical probability to have α photons in one channel and β photons in the other channel of the PBS. Such equations allow us to estimate N_4 and η, the experimental parameters indicating the total number of photons stemming from four-photon events and the no-loss rate, respectively. It is clear that equations similar to Eq. (3.33) for c_{ABC} must be fulfilled for other coincidences, such as c_{ABD} or c_{ACD}. Since both N_4 and η do not depend on the internal phase of the interferometer, we just need to solve Eq. (3.33) in the zero delay zone:

$$\langle c_{ABCD}(\delta l \simeq 0)\rangle = \frac{1}{4}\eta^4 N_4 P^{ex}_{22}; \tag{3.35}$$

getting the normalization of the fast fringes pattern. Repeating this strategy for all detector combinations, we obtain $P^{max}_{22} \simeq 0.915$, around 10% less than the theoretical prediction.

3.2.4 Four-dimensional Bell state

When the design of the interferometer in Fig.3.8 was introduced, we struggled seeking the proper conversion parameter for the maximization of the spatial entanglement. In fact, the possibility to manipulate different parameters, such as the path length, the BS and the HWP parameters, enables the investigation of a discrete variety of interesting scenarios. In order to explore some of them analytically, we benefit from the fact that the period of oscillation of the internal phase in Eq.(3.26) is of the same magnitude of λ_p, namely much bigger than the size of the PDC spectrum $\Delta\lambda$. This means that the Schmidt modes in Eq.(3.26) scarcely depend on the oscillating terms and the phase can therefore be taken out of the integral:

$$\begin{aligned} C_k^\dagger &\approx e^{i\frac{\omega_p}{2}\frac{\Delta l}{c}} \int d\omega_s u_k(\omega_s) a^\dagger(\omega_s) = e^{i\frac{\omega_p}{2}\frac{\Delta l}{c}} A_k^\dagger, \\ D_k^\dagger &\approx e^{i\frac{\omega_p}{2}\frac{\Delta l}{c}} \int d\omega_i v_k(\omega_i) a^\dagger(\omega_i) = e^{i\frac{\omega_p}{2}\frac{\Delta l}{c}} B_k^\dagger. \end{aligned} \tag{3.36}$$

This makes the Schmidt modes C (B) and A (D) proportional. On the other hand, the distinguishability between A and B holds, due to the different group velocities between signal and idler photons. If we do not fix any specific values for all Δl, ϕ_1 and θ, the output state of the interferometer becomes:

$$\begin{aligned} |\psi\rangle = \Bigg[\sum_k \big(&A^\dagger_{k_2}(e^{\pi i\Delta l/\lambda_p}\cos\theta\sin\phi_1 - \cos\phi_1\sin\theta) \\ &-iA^\dagger_{k_1}(\cos\theta\cos\phi_1 + e^{\pi i\Delta l/\lambda_p}\sin\theta\sin\phi_1)\big) \\ &\big(B^\dagger_{k_1}(-ie^{\pi i\Delta l/\lambda_p}\cos\phi_1\sin\theta + i\cos\theta\sin\phi_1) \\ +B^\dagger_{k_2}(&e^{\pi i\Delta l/\lambda_p}\cos\theta\cos\phi_1 + \sin\theta\sin\phi_1)\big)\sqrt{\lambda_k}\Bigg]^2 |0\rangle. \end{aligned} \tag{3.37}$$

For the sake of simplicity it can be reduced by decreasing the number of spectral modes to 1 just by tuning opportunely the pulse duration[6]:

$$|\psi\rangle = \Bigg[\big(A_2^\dagger(e^{\pi i\Delta l/\lambda_p}\cos\theta\sin\phi_1 - \cos\phi_1\sin\theta) - iA_1^\dagger(\cos\theta\cos\phi_1 + e^{\pi i\Delta l/\lambda_p}\sin\theta\sin\phi_1)\big)$$

$$\big(B_1^\dagger(-ie^{\pi i\Delta l/\lambda_p}\cos\phi_1\sin\theta + i\cos\theta\sin\phi_1) + B_2^\dagger(e^{\pi i\Delta l/\lambda_p}\cos\theta\cos\phi_1 + \sin\theta\sin\phi_1)\big)\Bigg]^2|0\rangle. \tag{3.38}$$

This state will be the start point of the analysis in this section. By proper manipulating the parameters of the interferometer we can achieve different interesting state. As first case, we annul the path delay $\Delta l = 0$, which reduces the equation above to:

$$|\psi_{\Delta l=0}\rangle = \Big[(A_2^\dagger\sin(\phi_1-\theta) - iA_1^\dagger\cos(\phi_1-\theta))(iB_1^\dagger\sin(\phi_1-\theta) + B_2^\dagger\cos(\phi_1-\theta))\Big]^2|0\rangle. \tag{3.39}$$

Along the last section we fixed both $\phi_1 = \pi/4$ and $\theta = \pi/4$, and it turned out that P_{22} grew to 1. Looking at Eq.(3.39), it becomes clear that the condition $\phi_1 = \theta$ leads to the state $\big(A_1^\dagger B_2^\dagger\big)^2|0\rangle$, where both signal photons are found in the first output channel whereas both idler photons are in the second output channel. However, more interesting is the case achieved when $\phi_1 - \theta = \pi/4$. By rewriting the state Eq.(3.39) in the space of the Schmidt mode A and B we have:

$$\begin{aligned}|\psi_{\Delta l=0}\rangle &= \left[\frac{i}{2}(|g\rangle_A|r\rangle_B - |r\rangle_A|g\rangle_B) + \frac{1}{2}(|r\rangle_A|r\rangle_B + |g\rangle_A|g\rangle_B)\right]^2 \\ &= \frac{1}{2}(|\Phi^+\rangle - i|\Psi^-\rangle)^2,\end{aligned} \tag{3.40}$$

where r and g are the first and the second channel of the interferometer in Fig.3.8 respectively[7], whereas $|\Phi^+\rangle$ and $|\Psi^-\rangle$ are the Bell states defined in our notation as following:

$$\begin{aligned}|\Psi^+\rangle &= \frac{1}{\sqrt{2}}(|r\rangle_A|g\rangle_B + |g\rangle_A|r\rangle_B)\\ |\Psi^-\rangle &= \frac{1}{\sqrt{2}}(|r\rangle_A|g\rangle_B - |g\rangle_A|r\rangle_B)\\ |\Phi^+\rangle &= \frac{1}{\sqrt{2}}(|r\rangle_A|r\rangle_B + |g\rangle_A|g\rangle_B)\\ |\Phi^-\rangle &= \frac{1}{\sqrt{2}}(|r\rangle_A|r\rangle_B - |g\rangle_A|g\rangle_B).\end{aligned} \tag{3.41}$$

In other words, Eq.(3.40) shows that the manipulation of the internal parameter of the interferometer enables the realization of four dimensional Bell states. If we turn back to

---

[6] This can be easily done in ppKTP waveguide. Normally we would need a frequency filter to reduce the number of spectral modes.

[7] The names r and g come from the choice of colours red and green in Fig.3.8. Putting 1 and 2 could have looked confusing.

Eq.(3.38) and fix another path delay, namely $\Delta l = \lambda_p$, the output state becomes:

$$|\psi_{\Delta l=\lambda_p}\rangle = \big[-\big(A_2^\dagger \sin(\phi_1+\theta) + iA_1^\dagger \cos(\phi_1+\theta)\big)\big(iB_1^\dagger \sin(\phi_1+\theta) - B_2^\dagger \cos(\phi_1+\theta)\big)\big]^2|0\rangle, \tag{3.42}$$

and by introducing the Bell states of Eq.(3.41) as before the output state is reduced to:

$$|\psi_{\Delta l=\lambda_p}\rangle = \frac{1}{2}(|\Phi^+\rangle + i|\Psi^-\rangle)^2, \tag{3.43}$$

which stems from choosing $\phi_1 + \theta = \pi/4$. It is interesting to notice that both the states in Eq.(3.40) and Eq.(3.43) are achieved by fixing $\phi_1 = \pi/4$ and $\theta = 0$. In the framework of Section 3.2.2, these states are found within the interferometer (or simply by removing the BS at all), namely choosing $\phi_1 = \pi/4$ and $\theta = 0$.

The other way around, we both fix $\phi_1 = \pi/4$ and $\theta = 0$ and test the output state at two further values of path delay, namely $\Delta l = \lambda_p/2$ and $\Delta l = 3\lambda_p/2$, obtaining:

$$|\psi_{\Delta l=\frac{\lambda_p}{2}}\rangle = \frac{1}{2}(|\Phi^-\rangle + |\Psi^-\rangle)^2, \tag{3.44}$$

$$|\psi_{\Delta l=\frac{3\lambda_p}{2}}\rangle = \frac{1}{2}(|\Phi^-\rangle - |\Psi^-\rangle)^2. \tag{3.45}$$

An overlook of the last equations lets us state that, already in Section 3.2.2, we were able to generate products of Bell states inside the interferometer such as $|\Phi^+\rangle$ and $|\Psi^-\rangle$, or $|\Phi^-\rangle$ and $|\Psi^-\rangle$ alternately. This type of states can be expressed in terms of a four-qubit Bell Gem introduced in [114] and [115]:

$$\begin{aligned}
G_1^\pm &= \frac{1}{\sqrt{2}}(|\Phi^+\rangle|\Phi^+\rangle \pm |\Phi^-\rangle|\Phi^-\rangle),\\
G_2^\pm &= \frac{1}{\sqrt{2}}(|\Psi^+\rangle|\Psi^+\rangle \pm |\Psi^-\rangle|\Psi^-\rangle)\\
G_3^\pm &= \frac{1}{\sqrt{2}}(|\Phi^+\rangle|\Phi^-\rangle \pm |\Phi^-\rangle|\Phi^+\rangle),\\
G_4^\pm &= \frac{1}{\sqrt{2}}(|\Phi^+\rangle|\Psi^+\rangle \pm |\Psi^+\rangle|\Phi^+\rangle),\\
G_5^\pm &= \frac{1}{\sqrt{2}}(|\Phi^+\rangle|\Psi^-\rangle \pm |\Psi^-\rangle|\Phi^+\rangle),\\
G_6^\pm &= \frac{1}{\sqrt{2}}(|\Phi^-\rangle|\Psi^+\rangle \pm |\Psi^+\rangle|\Phi^-\rangle),\\
G_7^\pm &= \frac{1}{\sqrt{2}}(|\Phi^-\rangle|\Psi^-\rangle \pm |\Psi^-\rangle|\Phi^-\rangle),\\
G_8^\pm &= \frac{1}{\sqrt{2}}(|\Psi^+\rangle|\Psi^-\rangle \pm |\Psi^-\rangle|\Psi^+\rangle),
\end{aligned} \tag{3.46}$$

which is a high-dimensional Bell state basis. For instance, in terms of Bell Gem states Eq.(3.40) becomes:

$$\begin{aligned}
|\psi\rangle_{\Delta l=0} &= \frac{1}{2}\big(|\Phi^+\rangle|\Phi^+\rangle - |\Psi^-\rangle|\Psi^-\rangle - i(|\Phi^+\rangle|\Psi^-\rangle + |\Psi^-\rangle|\Phi^+\rangle)\big)\\
&= \frac{1}{2\sqrt{2}}(G_1^+ - G_1^- + G_2^- - G_2^+) - \frac{i}{\sqrt{2}}G_5^+,
\end{aligned} \tag{3.47}$$

whereas Eq.(3.44) turns into:

$$
\begin{aligned}
|\psi\rangle_{\Delta l=\lambda_p} = \frac{1}{2}\big(&|\Phi^-\rangle|\Phi^-\rangle + |\Psi^-\rangle|\Psi^-\rangle + |\Phi^-\rangle|\Psi^-\rangle + |\Psi^-\rangle|\Phi^+\rangle\big) \\
&= \frac{1}{2\sqrt{2}}(G_1^+ - G_1^- - G_2^- + G_2^+) + \frac{1}{\sqrt{2}}G_7^- .
\end{aligned}
\tag{3.48}
$$

We conclude this section by noting that the term in brackets in Eq.(3.47) is a combination of states having an even number of photons in both channels of the interferometer, whereas G_5^+ actually coincides with the state $|\psi_{beforeBS}(3113)\rangle$ in Eq.(3.29) when $\Delta l = 0$, $\phi_1 = \pi/4$ and $\theta = 0$. This state, is characterized by a high degree of entanglement, and in principle it can be isolated by post-selection measurement.

3.2.5 Compensation of group velocities and faster oscillations

In Section 3.2.2 it was proven that the presence of spatial entanglement inside the interferometer leads to coincidence probabilities characterized by fast oscillating profiles, whose period is proportional to λ_p. The structure of these oscillations strongly depends on the degree of distinguishability of signal and idler photons. The oscillating patterns in Fig.3.10 were achieved using a partially single mode source, whose signal and idler output photons were spectrally distinguishable: the modulus, as well as the real and the imaginary part of the Schmidt modes of signal photons were enough different from idlers, moreover the JSA was far to be symmetrical along the $\omega_s - \omega_i$ axes. In this section we want to observe how these patterns vary when signal and idler photons tend to get identical by making their spectra indistinguishable.

As a first step, we can increase the degree of spectral correlation, for instance enhancing the pump pulse duration and making the JSA strongly symmetrical along the frequencies axis. This ensures the spectral indistinguishability of signal and idler photons being the modulus of the Schmidt modes identical, namely $|u_k(\omega_s)|^2 = |v_k(\omega_i)|^2$. Although this procedure enhances the degree of spectral indistinguishability of signal and idler photons, we can still distinguish them because the real and the imaginary part are still partially different and this is due to the dispersion along the waveguide. Indeed, a time delay due to the different group velocities between ordinary and extraordinary polarizations is experienced by all photons. Such delay modifies the global phase of the JSA and is not detectable in the output spectrum.

In order to balance this discrepancy, we imagine to put a further perfectly converting HWP immediately after the PDC section, followed by a non-poled KTP crystal having length $L_{pdc}/2$ (Fig.3.13). Since photons are supposed to be generated in the middle of the PDC section, the time delay accumulated by walking through the source is fully compensated when photons leave the jointed crystal, thereby making both real and imaginary part of $u_k(\omega_s)$ and $v_k(\omega_i)$ identical.

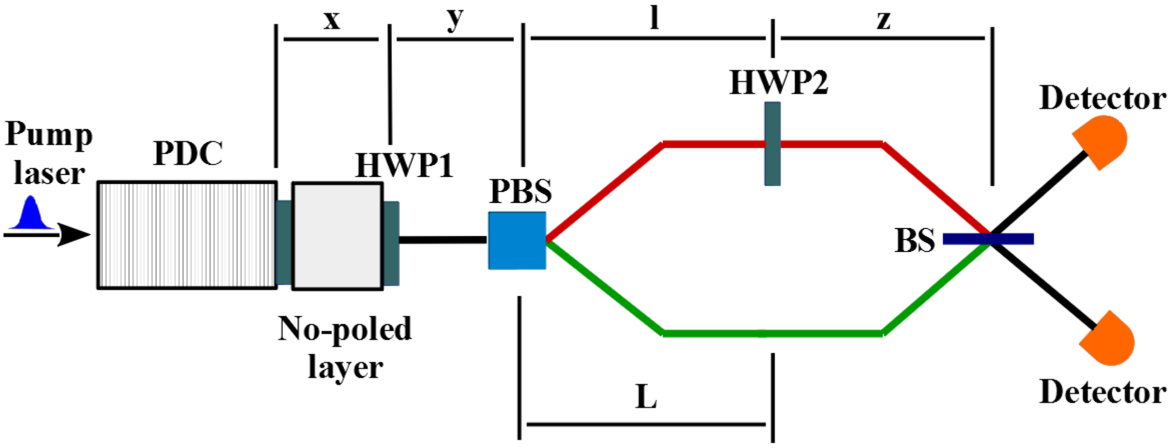

Figure 3.13: Schematic setup with compensator. A further HWP as well as a non-poled KTP crystal are jointed in order to compensate the discrepancy in the signal-idler group velocities [2].

Mathematically this modification can be carried out in two equivalent ways. For instance, one can add a further HWP matrix in Eq.(3.20) and modify the matrix FP_0 congruently, namely including the refractive index of KTP. Alternatively, one can add a phase term in the JSA as follow:

$$F(\omega_s,\omega_i) = e^{-(\omega_s+\omega_i-\omega_p)\tau^2/2}\,\mathrm{sinc}\left[\frac{\Delta\beta L}{2}\right] e^{i\frac{L}{2}(\Delta\beta+\bar{k})}, \tag{3.49}$$

where $\bar{k} = -k_e(\omega_s) - k_o(\omega_i)$ contain the refractive index for both signal and idler photons, keeping into account the polarization conversion.

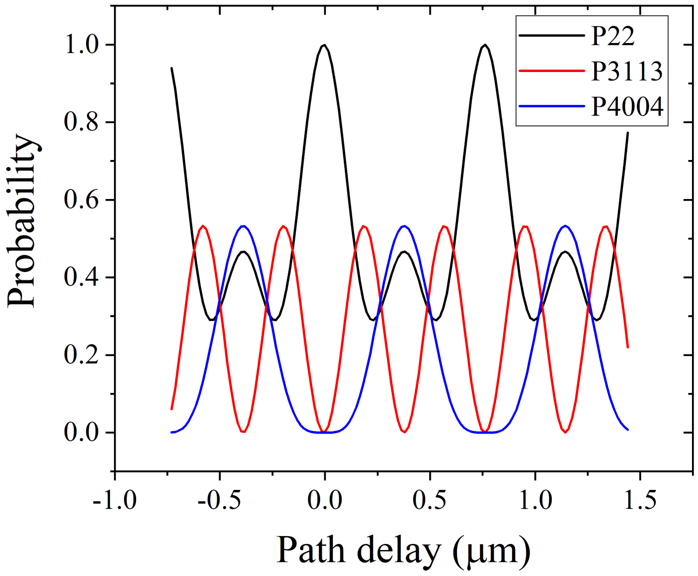

Figure 3.14: The zoom of the P_{22}, P_{3113} and P_{4004} probabilities in the configuration described by the identical signal-idler Schmidt operators. Pulse duration $\tau = 10ps$ [2].

Resuming, by enhancing the symmetry of the JSA and modifying the interferometer we can make the Schmidt operators of signal and idler identical, and the output probabilities can be calculated. If we fix $\phi_1 = \theta = \pi/4$ (same conditions used in Section 3.2.2), the output state of the interferometer becomes:

$$|\psi\rangle = |\psi(22)\rangle + |\psi(4004)\rangle + |\psi(3113)\rangle, \tag{3.50}$$

where

$$\begin{aligned} |\psi(22)\rangle = &-\frac{e^{2\pi i\Delta l/\lambda_p}}{4}\sum_{k\tilde{k}}\sqrt{\lambda_k\lambda_{\tilde{k}}} \\ &\times\left[\sin^2\left(\frac{\pi\Delta l}{\lambda_p}\right)\left({A^\dagger_{k_1}}^2{A^\dagger_{\tilde{k}_2}}^2 + {A^\dagger_{\tilde{k}_1}}^2{A^\dagger_{k_2}}^2\right) + 4\cos^2\left(\frac{\pi\Delta l}{\lambda_p}\right)A^\dagger_{k_1}A^\dagger_{\tilde{k}_1}A^\dagger_{k_2}A^\dagger_{\tilde{k}_2}\right]|0\rangle, \end{aligned} \tag{3.51}$$

$$|\psi(4004)\rangle = -\frac{e^{2\pi i\Delta l/\lambda_p}}{4}\sum_{k\tilde{k}}\sqrt{\lambda_k\lambda_{\tilde{k}}}\sin^2\left(\frac{\pi\Delta l}{\lambda_p}\right)\left({A^\dagger_{k_2}}^2{A^\dagger_{\tilde{k}_2}}^2 + {A^\dagger_{k_1}}^2{A^\dagger_{\tilde{k}_1}}^2\right)|0\rangle, \tag{3.52}$$

$$\begin{aligned} |\psi(3113)\rangle = &-\frac{e^{2\pi i\Delta l/\lambda_p}}{4}\left[\sum_{k\tilde{k}}\sqrt{\lambda_k\lambda_{\tilde{k}}}\sin^2\left(\frac{2\pi\Delta l}{\lambda_p}\right)\right. \\ &\left.\times\left({A^\dagger_{k_1}}^2A^\dagger_{\tilde{k}_1}A^\dagger_{\tilde{k}_2} + A^\dagger_{k_1}A^\dagger_{k_2}{A^\dagger_{\tilde{k}_1}}^2 + {A^\dagger_{k_2}}^2A^\dagger_{\tilde{k}_2}A^\dagger_{\tilde{k}_1} + {A^\dagger_{\tilde{k}_2}}^2A^\dagger_{k_2}A^\dagger_{k_1}\right)|0\rangle.\right. \end{aligned} \tag{3.53}$$

From these formulas and from Fig.3.14, the new period of oscillation can be immediately estimated from the oscillating functions. In particular, one can see that for both P_{22} and P_{4004} the period of oscillation still corresponds to λ_p like in section 3.2.2, however, more interesting is the oscillation period of P_{3113}, which is now half smaller, namely equal to $\lambda_p/2$. Thus, it turns out that in this current scheme we can get interfering fringes whose oscillation period is smaller than the pump wavelength. On the other hand, we can see that every time $\Delta l = (2m+1)\lambda_p/2$ is fulfilled, where m is an integer number, a balanced superimposition of the original input state and the NOON state with n=4 is generated.

3.2.6 Conclusion

The presence of an additional HWP in front of the PBS leads to a wide range of new interesting results. By properly manipulating the further conversion parameter, we could trigger and maximize the spatial entanglement between the two arms of the interferometer, with drastic consequences in the coincidence probabilities. The most evident change is the presence of structured fast oscillations in all P_{22}, P_{3113} and P_{4004}, whose periodicity corresponds to the pump length. Moreover, the structure of such oscillations, observed also experimentally, presents irregular shapes and this is determined by additional interference processes on the BS between states inside the interferometer having even number of photons. This phenomenon is related to the quantum nature of light.

More generally, we could take advantage of the possibility to manipulate different parameters, such as the PC conversion constant and the reflectivity of the BS. This strategy offered more perspectives of investigation and allowed us to achieve new results, such as the possibility to generate combinations of four dimensional Bell states, which can be isolated via post-selection measurements and used as start point for more complex entangled structures.

Finally, by adding another HWP followed by a piece of non-poled KTP waveguide and using pump laser with a narrow bandwidth, we were able to create a set of spectrally identical photons (and having also the same polarization), and split them in the two channels of the interferometer. The full indistinguishability as well as the presence of spatial entanglement inside the interferometer drastically alter the shape of the interference pattern, whose oscillation period is even twice faster than the pump wavelength λ_p. This result is quite interesting, since it can enable future high-precision measurements.

Chapter 4

The spectrally multimode integrated SU(1,1) interferometer

Testing and optimizing different interferometer designs in order to achieve high precision measurements is one of the main goal of quantum metrology [55]. We already experienced that modelling and engineering an interferometer with high performances fundamentally means facing the problem of noise reduction in phase sensing tests. In particular, we have seen that part of this noise is due to the use of radiation having classical correlations within the interferometer. In quantum metrology as well as in quantum lithography, the reduction of this noise is formally expressed by overcoming the shot-noise limit [67, 77, 85], or in other words by ensuring that the dependence of the phase sensitivity in the interferometer decays faster than $1/\sqrt{N_{in}}$, where N_{in} is the number of photons inside the interferometer. In a typical Mach-Zehnder design, this can be done by exploiting exotic quantum photon states, such us squeezed light or NOON states [8]. On the other hand, we mentioned that sometimes the employment of such quantum light allows to reach (but not beat) a second limit of interferometry, called Heisenberg limit, which stems from the employment of quantum electromagnetic fields and is proportional to the inverse of N_{in} [65].

In this context, the introduction of the SU(1,1) interferometer was a strategic point, since the sensitivity of this device is strongly immune to external losses [80,81], moreover, it is able to overcome the SNL even via the use of vacuum and coherent states as input light [66, 71, 123].

However, this primordial analysis must now be tested in realistic frameworks. Indeed, it becomes more evident that the boost of the current technology points out the requirement of punctual and modern schemes, which must face the experimental support as well as the progressively stronger request of optimization and miniaturization, especially (for our purposes) in quantum metrology.

In our SU(1,1) investigation, a conceptual start point is hence the elaboration of new theoretical models taking into account the spectral properties of the radiation generated by the non-linear amplifiers [124]. Such models permit further employments of the SU(1,1) interferometers beyond the phase sensing, for instance in state engineering scenarios [125–127].

The second point is the development of this device in an integrated platforms [128,129].

The integration of systems previously explored in bulk is an interesting technique already used for other scopes, such as boson sampling [130], quantum walk [131] and Hong-Ou-Mandel interference [132, 133], and it seems to be promising also in non-linear quantum interferometry. The installation of the interferometer into an integrated platform ensures a smaller footprint and enables a progressive miniaturization of the device. Along this chapter, we will see how to model an integrated SU(1,1) interferometer in a KTP platform and how to take advantage from the spectral features of this device for maximizing the phase sensing efficiency.

4.1 The integrated interferometer and phase sensing tests

The most logical way to start this analysis is via introducing a more detailed description of the optical parametric amplifiers, namely the squeezing process within the interferometer. Since the SU(1,1) interferometer was firstly designed, different theoretical works in literature have approached this device by exploiting a relatively simple model, fully described in Section 2.2.6, in which the optical parametric amplifiers are typically devised as two squeezers without any spectral characterization. Yet from an experimental point of view, an empirical test over the results achieved by employing this model is quite challenging and one may encounter a lot of difficulties: indeed, typical optical parametric amplifiers used in lab do not generate simple plane waves mode photons spontaneously but photons having complex spectral profiles, i.e. characterized by a specific polarization and a well defined set of independent spectral modes, sometimes (also along this work) called Schmidt modes. Gradually it has become obvious that the inclusion of spatial [52, 134, 135] and spectral modes [79, 136, 137] in the description of the SU(1,1) interferometer not only improves the accuracy of the theoretical models drastically, but also pave the way to a more detailed investigation of the performance of the tested interferometer itself.

Along this work, we saw that the presence of spectral modes plays a crucial rule in linear interferometry when four photons interfere in HOM devices. The fundamental question of this chapter is: do the spectral features of the photon sources have any influence also in the performance of an integrated SU(1,1) interferometer?

4.1.1 JSA construction: first design

In order to answer the question above, let us start from the simplest scheme of integrated SU(1,1) interferometer illustrated in Fig.4.1 which can be imagined; it will be used as a model in the first part of this chapter. It basically consists of two identical spatially separated Type-II PDC sources, in particular we will use two ppKTP waveguides, wherein a phase modulator acting only on idler photon induces a modulation on the output radiation. The dynamics of the process is therefore relatively simple and it does not differ so much from what we have seen in Section 2.2.6: an incoming pump laser generates the signal-idler photon pair in the first waveguide; along the propagation path between the two waveguides the idler photon experiences a phase shift; in the second waveguide both photons interact with each other and finally the signal photon is finally detected. It is expected that a variation of the phase undergone by the idler photon leads to a modulation of the output light intensity because of the interference process.

In order to mathematically investigate this system, first of all we have to abandon the strategy commonly used in literature and employed in Section 2.2.6. Indeed, this relatively simple matrix approach is based on the assumption that temporal/spectral features of photons are irrelevant along the interference process, thus they might simply be ignored, thereby mathematically dealing with single mode Fock states and expressing the photon sources in terms of single mode squeezers (or two-mode squeezers in case of distinguished signal and idler photons).

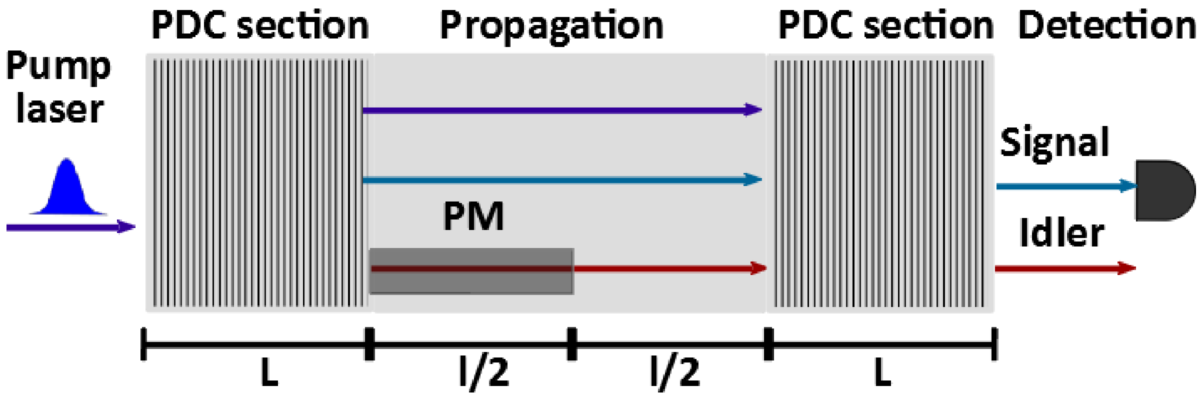

Figure 4.1: A schematic model of the collinear integrated SU(1,1) interferometer. An incoming pump laser interacts with a periodic poled PDC section, generating a signal-idler photon pairs. In the propagation path, idler photon undergoes a phase modulation (PM). Afterwards, both the generated photons and the pump beam interact in the second PDC section. Finally, the signal photon is detected. Different colours for signal and idler photons are used in order to distinguish vertical and horizontal polarizations [3].

An attempt of inserting the spectral properties of squeezers in the matrix approach would cause some difficulties. The first problem is an undefined expansion of the vector basis. Indeed, the most reasonable vector basis as a replacement of Eq.(2.69) would be the Schmidt basis, being this the most straightforward way to mathematically express the PDC as a squeezing transformation of the SU(1,1) interferometer, as it was seen in Section 2.1.3. Unfortunately, the elegance of this choice is not compensated by a straightforward ease of calculations, since the Schmidt basis consists in principle of infinite elements (although in a realistic case the effective number of modes could amount to the order of magnitude of around hundreds or even thousands modes). The second mathematical difficulty, which is even more critical, stems from the dispersion: photons propagating along such structure experience different group velocities inducing an alteration of the mode structure: along the propagation, the spectral modes of both photons undergo modifications on their profiles, and consequently the output modes of the second waveguide are quite different from those modes coming out from one waveguide. Another way to express this concept is: the doubling of the length of the interferometer leads to a different JSA and therefore to another set of spectral modes in the output with respect to the single waveguide modes. A proper matrix strategy should therefore include a vector basis having size tending to infinity and, and it should take dispersion into account, for instance via adding basis transformation matrices. Definitely not the most straightforward way to approach this system.

The strategy we want to utilise here is partially based on the procedure developed by Klyshko in 1993, used to analyse the effect of parametric scattering in a multilayer medium [138]. The main idea of this strategy consists of describing the phase matching function in a medium characterized by variations of refractive indices along the propagation direction (which will be z henceforth). According to this theory, one can hence express the JSA of the SU(1,1) interferometer we are investigating as the JSA of a biphoton state:

$$F(\omega_s, \omega_i) = C\alpha(\omega_s, \omega_i) f(\omega_s, \omega_i) \tag{4.1}$$

where C is the normalization parameter, whereas the phase matching function is expressed as:

$$f(\omega_s, \omega_i) = \frac{1}{2L} \int_0^{2L+l} dz\, g(z)\, e^{i\int_0^z d\xi \Delta k(\xi)}, \tag{4.2}$$

where $g(z)$ is the spatial profile of the second-order nonlinear susceptibility [139], l is the distance between two PDC sections, $\Delta k(\xi)$ is the phase matching profile. The function $f(\omega_s, \omega_i)$ describes the evolution of the phase matching along the SU(1,1) interferometer consisting of two periodic poled waveguides of length L, separated by a non-poled region of length l. Such expression is generalized with respect to the version proposed by Klyshko, and it takes into account the eventual modifications of the wave vectors along the whole waveguide [42, 140]. In this framework, the function $g(z)$ is

$$g(z) = \begin{cases} square_\Lambda(z) & 0 < z < L \vee L + l < z < 2L + l \\ 1 & L < z < l + L \end{cases}, \tag{4.3}$$

where $square_\Lambda(z)$ is the periodic square function that oscillates between -1 and +1 with periodicity Λ, determines the grating along the interferometer. Since our SU(1,1) interferometer consists of two periodic poled sections which are spatially separated, in order to calculate the proper JSA we Fourier expand the grate in Eq.(4.3) and split the phase matching function of Eq.(4.2) in three parts:

$$f(\omega_s, \omega_i) = \int_0^L dz\, e^{i\frac{2\pi z}{\Lambda}} e^{i\int_0^z d\xi \Delta k} + \int_L^{L+l} dz\, e^{i\int_0^z d\xi \Delta k} + \int_{L+l}^{2L+l} dz\, e^{i\frac{2\pi z}{\Lambda}} e^{i\int_0^z d\xi \Delta k} \tag{4.4}$$

The first integral, concerning the first periodically poled section, is already well known:

$$\frac{1}{2L} \int_0^L dk g(z) e^{i\int_0^z d\xi \Delta k} = \frac{1}{2L} \int_0^L dk e^{\frac{2\pi}{\Lambda}} e^{i\Delta k z} = \frac{e^{i\Delta\beta L} - 1}{2\Delta\beta L} = \mathrm{sinc}\left[\frac{\Delta\beta L}{2}\right] e^{i\frac{\Delta\beta L}{2}}. \tag{4.5}$$

Due to the absence of the poling period in the propagation region, the phase matching condition within the second integration in Eq.(4.4) is not closed and this makes the integrand a fast oscillating function, and for this reason we neglect this contribution. On the other hand, the third integral is calculated:

$$\begin{aligned}\int_{L+l}^{2L+l} dz\, e^{i\frac{2\pi z}{\Lambda}} e^{i\int_0^z d\xi \Delta k} &= e^{i\frac{(\Delta k+\Delta k')l}{2}} e^{i\Delta k L} \int_{L+l}^{2L+l} dz\, e^{i\frac{2\pi z}{\Lambda}} e^{i\Delta k(z-l-L)} \\ = e^{i\Delta k L} e^{i\frac{(\Delta k+\Delta k')l}{2}} e^{i\frac{2\pi(L+l)}{\Lambda}} \int_0^L dq\, e^{i\frac{2\pi q}{\Lambda}} e^{i\Delta k q} &= e^{i\Delta\beta L} e^{i\frac{(\Delta\beta+\Delta\beta')l}{2}} \frac{e^{i\Delta\beta L}-1}{2\Delta\beta L} \\ &= \operatorname{sinc}\left[\frac{\Delta\beta L}{2}\right] e^{i\Delta\beta L} e^{i\frac{(\Delta\beta+\Delta\beta')l}{2}},\end{aligned} \tag{4.6}$$

and it concerns the second periodically poled section. This term contains information about the phase modulation in the term $\Delta\beta' = k_o(\omega_p) - k_o(\omega_s) - k_e'(\omega_i) + 2\pi/\Lambda$, namely the phase mismatch in the modulator region. The term $k_e'(\omega_i)$ represents the modification of the wave vector of idler photon following the phase variation. Experimentally, the phase shift can be achieved via electrooptic modulation, namely by making use of an external voltage which acts on the refractive index of extraordinary polarized photon. Mathematically, this means that the difference between $\Delta\beta$ and $\Delta\beta'$ is solely due to the variation of the wave vector $k_e(\omega_i)$, therefore the phase matching in the modulator region can be written as:

$$\frac{\Delta\beta' l}{2} = \frac{\Delta\beta l}{2} + \frac{k_e(\omega_i)l - k_e'(\omega_i)l}{2} = \frac{\Delta\beta l}{2} + \frac{\delta k_e(\omega_i)l}{2}. \tag{4.7}$$

This formula helps us to define a proper adimensional phase variable $\phi = \delta k_e(\omega_p/2)l/2$, so that we can express Eq.(4.7) in terms of a mathematically manipulable parameter:

$$\frac{\Delta\beta' l}{2} = \frac{\Delta\beta l}{2} + \frac{\delta k_e(\omega_i)\phi}{\delta k_e(\omega_p/2)}. \tag{4.8}$$

By summing Eq.(4.5) and Eq.(4.6) in Eq.(4.1), we finally obtain the JSA of the whole SU(1,1) interferometer:

$$\begin{aligned}F(\omega_s,\omega_i) &= \frac{C}{2L}\alpha(\omega_s,\omega_i) \int_0^L dz\, g(z)\, e^{i\int_0^z d\xi\Delta k} \\ &= 2C\alpha(\omega_s,\omega_i) \operatorname{sinc}\left[\frac{\Delta\beta L}{2}\right] \cos\left(\frac{2\Delta\beta L + \Delta\beta l + \Delta\beta' l}{4}\right) e^{i(\Delta\beta L + \Delta\beta l/4 + \Delta\beta' l/4)},\end{aligned} \tag{4.9}$$

where the interference pattern is determined by scanning the adimensional parameter ϕ.

It is interesting to notice that, fixing $l = 0$, Eq.(4.9) exactly provides the JSA of a PDC effect generated by a waveguide having length $2L$:

$$F(\omega_s,\omega_i) = C\alpha(\omega_s,\omega_i) \operatorname{sinc}(\Delta\beta L) e^{i\Delta\beta L}, \tag{4.10}$$

which is characterized by a narrower JSA in comparison with the single crystal JSA[1].

By enhancing the voltage we can induce the phase shift between signal and idler photons, modulating the output radiation. In this framework, we can plot the evolution

---

[1] This argument holds because we assume that the last part of the grating of the first waveguide perfectly matches the grate in the beginning of the second waveguide.

of the JSI when the phase ϕ runs from 0 to 2π. This is done in Fig.4.2, where we observe the profile of the JSI for different phases.

It should not be surprising that in the degeneracy frequency $\omega_p/2$ the JSI reaches the maximum value at $\phi = 0$ and drops to zero at $\phi = \pi$. At the degeneracy point, the phase matching relation is perfectly fulfilled because of the poling period, and the JSA is merely modulated as $\cos(\phi/2)$.

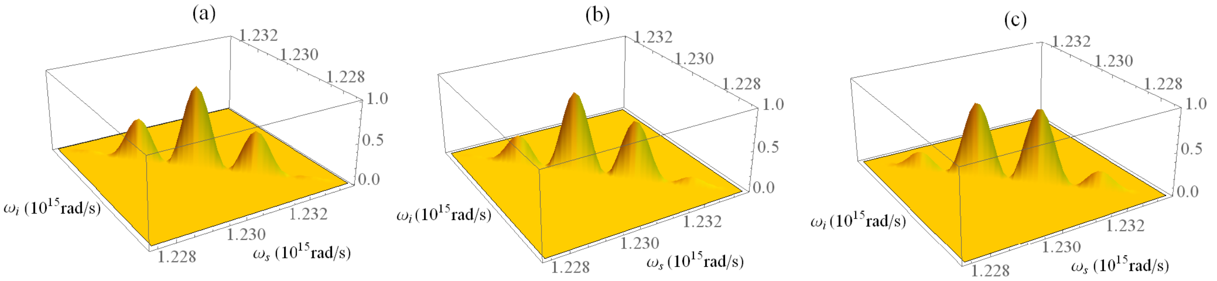

Figure 4.2: The joint spectral intensity $|F(\omega_s, \omega_i)|^2$ depending on the phase implemented by the phase modulator: (a) $\phi = 0$, (b) $\phi = \pi/2$ and (c) $\phi = \pi$. The following parameters are chosen: the CW laser, the KTP (potassium titanyl phosphate) platform, the pump wavelength $\lambda_p = 766nm$, the crystal length $L = 8mm$, the distance between the two poling sections $l = 10mm$, the period of poling $\Lambda = 126\mu m$ [3].

However, for frequencies far from the degeneracy this argument does not hold any more, and although Eq.(4.9) shows the possibility to modulate JSA and consequently to manipulate the spectral mode distribution, there is no way to drastically attenuate the light intensity coming out of the interferometer in this design, as expected in a perfect interference process. Thus, the extremely low visibility caused by the non-perfect interference expected in the photon counting makes the estimation of the phase sensitivity unworthy. A very narrow filter around the central frequency might solve the problem, but this solution would attenuate the influence of the spectral features we are determined to investigate. Along the next section this problem will be solved by using an alternative and more efficient strategy.

4.1.2 JSA construction: second design

The model introduced above, which is the straightforward realization of the theoretical SU(1,1) interferometer design on a realistic platform, despite the intuitive structure and simplicity, does not allow to perform an interference with high visibility, since only the central frequency is subject to a total attenuation at $\phi = \pi$. On the contrary, the phase shift merely induces a modulation of the JSI at other frequencies. Physically, the dispersion caused by the different group velocities between signal and idler photons during the propagation along the device dramatically attenuates the interference, since their temporal envelopes do not match.

The key point of this section is thus to compensate the group velocities between signal and idler photons, thereby matching the envelopes in the second periodic poled section and attenuating the visibility of all frequencies. An elegant way to achieve this result is via inserting a polarization converter in the centre of the interferometer, as shown in Fig. 4.3. An intuitive physical explanation is following: since the polarization determines the group velocity experienced by each photon, we switch the polarizations of both photons in the middle of the interferometer, so that the faster photon becomes the slowest and vice versa, thereby matching the temporal envelopes of both photons in the middle of the second periodic poled section. Finally, the additional phase undergone by idler photon will determine the constructive or destructive interference.

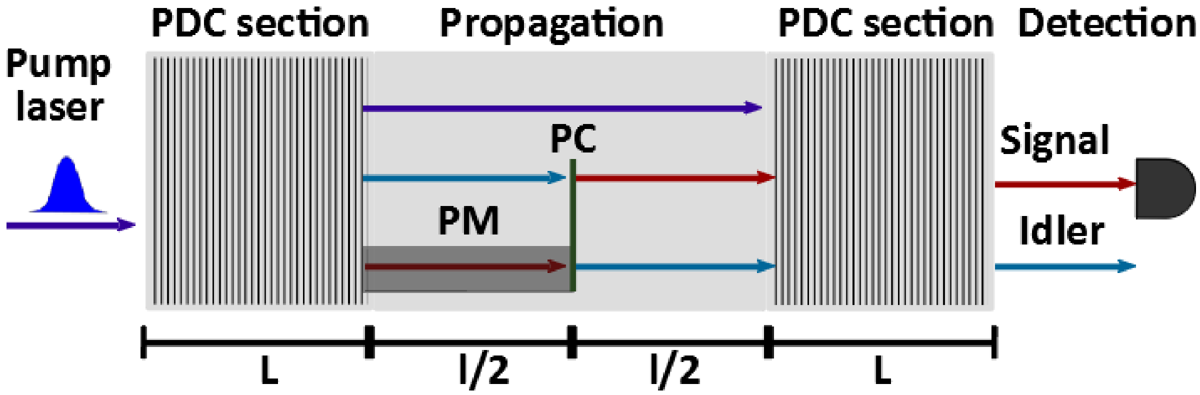

Figure 4.3: A schematic model of the integrated SU(1,1) interferometer with the time delay compensation. An incoming pump laser interacts with a periodic poled PDC section, where signal-idler photons pairs are generated. The idler photon undergoes a phase modulation (PM). Afterwards, a polarization converter (PC) located in the middle of the device switches polarizations of signal and idler photons. Finally, all beams interact in the second PDC section. In the end, the signal photon is detected. Different colours are used in order to distinguish vertical (red) and horizontal (blue) polarizations [3].

In order to justify this strategy mathematically, we start by calculating the JSA of the interferometer proceeding as before, hence obtaining:

$$\begin{aligned} F(\omega_s,\omega_i) = \frac{C}{2}\alpha(\omega_s,\omega_i)\Bigg[&\operatorname{sinc}\left[\frac{\Delta\beta L}{2}\right]e^{i\Delta\beta L/2} + \operatorname{sinc}\left[\frac{\overline{\Delta\beta}L}{2}\right] \\ &\times \exp\left\{i\left(\frac{\overline{\Delta\beta}L}{2} + \Delta\beta L + \frac{(\Delta\beta' + \overline{\Delta\beta})l}{2}\right)\right\}\Bigg], \end{aligned} \tag{4.11}$$

where $\overline{\Delta\beta} = k_o(\omega_p) - k_e(\omega_s) - k_o(\omega_i) + 2\pi/\Lambda$ is the phase matching after the polarization switch. It is evident that this JSA is strongly different with respect to Eq.(4.9), especially because of the introduction of $\overline{\Delta\beta}$. This term will be determinant in the realization of the interference processes with high visibility, and will play a fundamental role in the evaluation and optimization of the phase sensitivity of the device.

In order to demonstrate that the presence of $\overline{\Delta\beta}$ modifies the JSA enabling an interference scenario with high visibility, we can firstly perform a Taylor expansion of the phase matching $\Delta\beta$ around $\omega_p/2$ [141,142]. Assuming to have high correlations between signal and idler, so that $\omega_i = \omega_p - \omega_s$, we can express the phase matching in terms of signal photon:

$$\Delta\beta \approx \underbrace{k_o(\omega_p) - k_o(\omega_p/2) - k_e(\omega_p/2) + \frac{2\pi}{\Lambda}}_{=0} \\ -\frac{\partial k_e}{\partial\omega}(\omega_p/2)(\omega_s - \omega_p/2) - \frac{\partial k_o}{\partial\omega}(\omega_p/2)(\omega_s - \omega_p/2), \tag{4.12}$$

and, by introducing both the detuning $\Omega = \omega_s - \omega_p/2$ and the group velocity $v = \partial\omega/\partial k$, it can be rewritten:

$$\Delta\beta \approx -\frac{\Omega}{v_e(\omega_p/2)} + \frac{\Omega}{v_o(\omega_p/2)}. \tag{4.13}$$

Analogously, we use the same procedure for $\overline{\Delta\beta}$, achieving:

$$\overline{\Delta\beta} \approx -\frac{\Omega}{v_o(\omega_p/2)} + \frac{\Omega}{v_e(\omega_p/2)}. \tag{4.14}$$

By comparing Eq.4.13 with Eq.4.14 we finally obtain

$$\overline{\Delta\beta} \simeq -\Delta\beta. \tag{4.15}$$

It is worthy to notice that the Tailor expansion makes sure that this relation holds not only at $\omega_p/2$, but also in its contour. Quantum correlations between signal and idler photons can be achieved, for instance, by employing a CW laser. This choice also prevents an additional delay compensation between the generated photons and the pump laser, and makes the stretching of the pump itself negligible. Substituting Eq.(4.15) in the expression of the JSA we have

$$F(\omega_s, \omega_i, \phi) \simeq C\,\delta(\omega_p - \omega_s - \omega_i)\,\mathrm{sinc}\left(\frac{\Delta\beta L}{2}\right)\cos\left(\frac{\delta k_e(\omega_i)\phi}{2\delta k_e(\omega_p/2)}\right)e^{\frac{i}{2}(\Delta\beta L + \delta k_e(\omega_p/2)l/2)}, \tag{4.16}$$

where $\delta(\omega_p - \omega_s - \omega_i)$ is the Dirac delta function describing the CW laser. In our calculations the CW regime is numerically simulated by setting a pump with a very large pulse duration, thereby covering the whole interferometer.

The peculiarity of the JSA in Eq.(4.16) is that,as long as $\frac{\delta k_e(\omega_i)}{\delta k_e(\omega_p/2)} \simeq 1$ holds, it corresponds to the two-photon amplitude of a single PDC source entirely modulated by a factor $\cos(\phi/2)$, namely in the contour of $\omega_p/2$. The timing compensation yielded by the presence of the PC along with the high correlations due to the CW laser enable the modulation of the whole JSA, which vanishes at $\phi = \pi$ entirely, in deep contrast to the former model introduced in the previous section.

It is worthy to emphasize that the employment of the CW laser is actually a crucial point of our argumentation. In principle, along this manuscript we experienced two different strategies for reaching a high correlation between signal and idler photons. Indeed, beside the tuning of the pulse duration, in Section 3.1.3 we made use of a special pulsed pump having a quadratic phase. In that scenario, we were able to increase the degree of correlation between signal and idler photons without reducing the spectral bandwidth

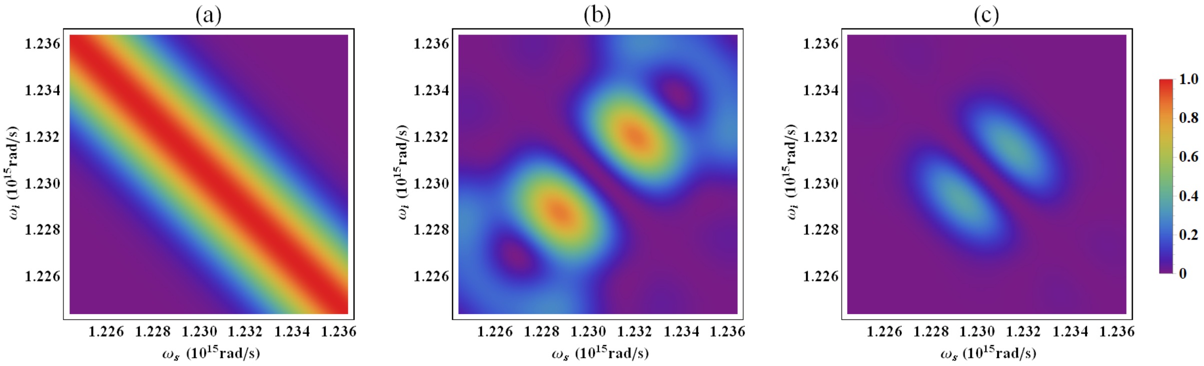

Figure 4.4: Normalized to one (a) the pump spectral bandwidth $\alpha(\omega_s, \omega_i)$, (b) the phase matching function $f(\omega_s, \omega_i)$ and (c) the joint spectral intensity $|F(\omega_s, \omega_i)|^2$ in the single-mode regime when $\phi \simeq \pi$. The pulse duration is $\tau = 0.35ps$, the length of the crystal is $L = 8mm$. By increasing the pulse duration, $\alpha(\omega_s, \omega_i)$ gets narrower with respect to the $\omega_s = \omega_p - \omega_i$ diagonal, this leads to zero overlap between $\alpha(\omega_s, \omega_i)$ and $f(\omega_s, \omega_i)$ and purely destructive interference [3].

of the pump laser. However, this choice is not preferable in this case; and on the contrary, the biphoton state of the interferometer itself suggests to increase the correlations between signal and idler photons by drastically reducing the pump bandwidth, namely via utilizing a CW laser.

We base the employment of the CW laser on the spectral analysis of the SU(1,1) interferometer, starting from Fig. 4.4. The picture shows the pump spectrum, the phase matching function and the JSI of the SU(1,1) interferometer modelled in Fig.4.3 at $\phi = \pi$ when a pulsed pump spectrally described by Fig.4.4a crosses the two PDC sections. The peculiar shape of the phase matching function in Fig.4.4b stems from the natural positive orientation of the phase matching of KTP on the $\omega_s{-}\omega_i$ diagram as well as the modification imprinted by the presence of the PC. The dip along the antidiagonal $\omega_s = \omega_p - \omega_i$ appears at $\phi = \pi$, following the additional phase modulation experienced by idler photon. Due to its large spectral bandwidth, the overlapping between the pulsed pump in Fig. 4.4a and the lobes of the phase matching function in Fig. 4.4b determines the presence of residual photon, whose non-vanishing JSI is depicted in Fig. 4.4c. The choice of a CW laser becomes intuitively clear: it enables the pump profile to fit into the antidiagonal dip of the phase matching function, thereby reducing the overlap dramatically and consequently almost annulling the output number of photons. Next section we demonstrate that by phase scanning the photon number with respect to the phase ϕ we will trace an interference curve with maximized visibility, which is a necessary condition for having high sensitivity [55].

4.1.3 The interference pattern

In the last section we delineated the profile of the JSA and consequently the expression of the biphoton state, now we can use them as start point for visualizing the interference pattern, namely the oscillating output intensity in the range $\phi \in [0 - 2\pi]$. This can be done by estimating the output number of photons in relation to the phase. In order to calculate the photon number, we proceed as in Section 2.1.3. From the expression of the

JSA in Eq.(4.11) we performed the Schmidt decomposition, so that we can decompose the JSA in terms of eigenvalues $\lambda_k(\phi)$, and spectral modes $u_k(\omega_s, \phi)$ and $v_k(\omega_i, \phi)$ for signal and idler respectively, which are dependent on the parameter ϕ:

$$F(\omega_s, \omega_i, \phi) = \sum_k \sqrt{\lambda_k(\phi)} u_k(\omega_s, \phi) v_k(\omega_i, \phi). \tag{4.17}$$

By introducing the input Schmidt operators as in Section 2.1.3 and then solving the coupled Heisenberg equations with the use of the Bogolyubov transformations, we obtain the output Schmidt operators of the SU(1,1) interferometer:

$$\begin{aligned} A_k^{out} &= A_k^{in} \cosh \gamma_k(\phi) + (B_k^{\dagger})^{in} \sinh \gamma_k(\phi), \\ B_k^{out} &= B_k^{in} \cosh \gamma_k(\phi) + (A_k^{\dagger})^{in} \sinh \gamma_k(\phi). \end{aligned} \tag{4.18}$$

where $\gamma_k(\phi) = 2G(\phi)\sqrt{\lambda_k(\phi)}$ and $G(\phi) = \int C(\phi)\Gamma dt$ is the experimental gain. An equivalent set of Heisenberg equations can be solved for the annihilation and creation operators in the plane wave modes:

$$\begin{aligned} a^{out}(\omega_s) &= a^{in}(\omega_s) \\ +\sum_k u_k(\omega_s, \phi) &\left[A_k^{in} \left(\cosh \left[G(\phi)\sqrt{\lambda_k(\phi)} \right] - 1 \right) + (B_k^{\dagger})^{in} \sinh \left[G(\phi)\sqrt{\lambda_k(\phi)} \right] \right], \\ b^{out}(\omega_i) &= b^{in}(\omega_i) \\ +\sum_k v_k(\omega_i, \phi) &\left[B_k^{in} \left(\cosh \left[G(\phi)\sqrt{\lambda_k(\phi)} \right] - 1 \right) + (A_k^{\dagger})^{in} \sinh \left[G(\phi)\sqrt{\lambda_k(\phi)} \right] \right]. \end{aligned} \tag{4.19}$$

The set of operators in Eq.(4.19) will be utilized soon, when the investigation of the SU(1,1) interferometer will be extended to filtering and seeding scenarios.

It is important to observe that the Schmidt modes calculated starting from the JSA in Eq. (4.11) are drastically different from the modes expected by the JSA in Eq.(4.9). Indeed, the spectral modes in the current scheme are closely similar to the modes originated by a single periodic poled waveguide. This is not surprising, being the JSA in Eq.(4.16) equivalent to Eq.(2.31) and parametrically modulated by a factor scarcely dependent on the frequency, as it was already mentioned above.

Once the Schmidt operators are defined, we can proceed calculating the output photon number of the SU(1,1) interferometer:

$$\langle N_s(\phi) \rangle = \sum_k \sinh^2 \gamma_k(\phi). \tag{4.20}$$

This expression strictly depends on the spectral features of the PDC processes and it is parametrically modulated by the phase ϕ, which determines the interference pattern. We plot the expression above at different ϕ in Fig.4.5.

The picture represents the photon number when a CW laser and a pump laser with the same bandwidth as in Fig 4.4a are utilized. It is evident that the employment of CW laser has a positive effect on the interference curve: the number of photons drops close to zero at $\phi = \pi$, leading to a maximization of the visibility. On the contrary, the red curve suffers a clear lack of visibility stemming from residual photons, whose JSA at $\phi = \pi$ is depicted in Fig.4.4c. The different trends remarked in such curves have crucial consequences in the phase sensing estimation, as it will be seen in the next section.

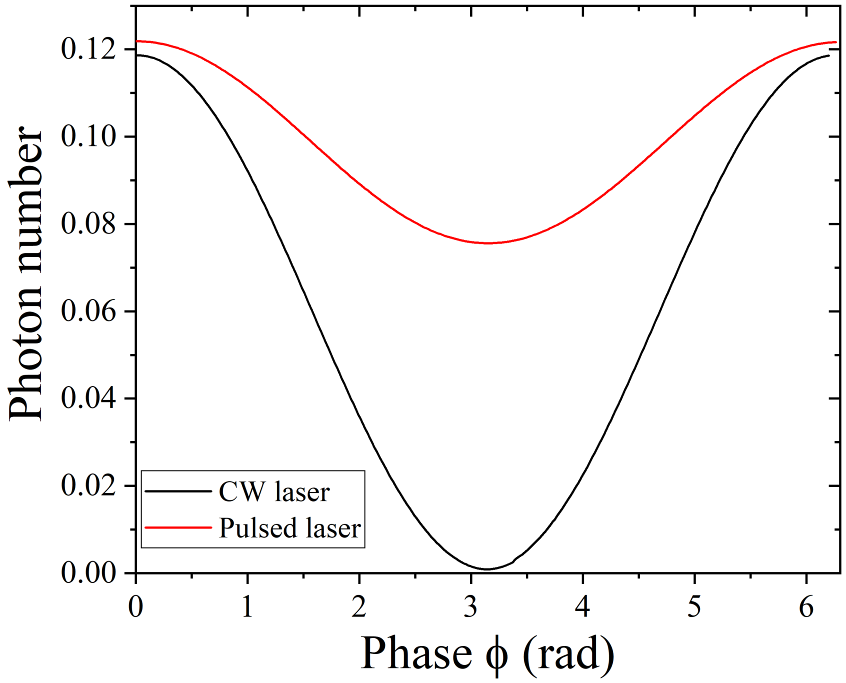

Figure 4.5: The comparison between the number of photons in the case of pulsed laser (the pulse duration $\tau = 0.35ps$, red line) and CW regime. In order to have a situation with the resulting number of photons being nearly identical at $\phi = 0$, different pump intensities are used for the two pumping regimes. The following parameters are chosen: $L = 8mm$, $\lambda_p = 766nm$, $l = 10mm$, $\Lambda = 126\mu m$ [3].

The trend in Fig.4.5 clearly demonstrates how the visibility of the interference pattern can be drastically improved by making use of CW laser. On the contrary, the intensity of the output light can be controlled by the parametric gain of the process. In this work, the parametric gain is defined as $\gamma = 2G(0)\sqrt{\lambda_1(0)}$, namely the squeezing parameter of the interferometer at $\phi = 0$ calculated with respect to the first spectral mode. We can numerically manipulate it by varying the coupling constant Γ, enabling to span a range of mean photon number between $\langle N(\phi = 0)\rangle \approx 0.12$ for $\gamma \simeq 0.04$ and $\langle N(\phi = 0)\rangle \approx 10^9$ for $\gamma \simeq 10.0$.

4.1.4 Estimation of the phase sensitivity

Along this chapter we formulated the mathematical model to describe an integrated SU(1,1) interferometer, showing that we can maximize the visibility of the interference pattern via spectral engineering of the photon state. The high visibility of the interference pattern eases an enhancement of the phase scanning accuracy beyond the SNL [55]. In this section we want to investigate the performance of this device by estimating the phase sensitivity with respect to the phase ϕ.

As already exposed in the first part of this work, the start point in the calculation of the phase sensitivity of the SU(1,1) interferometer is the formula given in Eq.(2.57), where the signal photon number operator $\hat{N}_s$ takes the place of the generic observable $\hat{O}$. However, differently from Section 2.2.6, the output operators of the interferometer coincide with the output Schmidt operators of PDC processes given in Eq.(4.18).

The two necessary elements to estimate the phase sensitivity are therefore the variance and the derivative of the average number of photons, which was already calculated in the previous section. From Eq.4.20 we can immediately calculate the derivative:

$$\begin{aligned}\frac{d\langle N\rangle}{d\phi} &= \sum_k \sinh\left[2G(\phi)\sqrt{\lambda_k(\phi)}\right] \\ &\times \left(\frac{dG(\phi)}{d\phi}\sqrt{\lambda_k(\phi)} + \frac{G(\phi)}{2\sqrt{\lambda_k(\phi)}}\frac{d\lambda_k(\phi)}{d\phi}\right),\end{aligned} \tag{4.21}$$

whereas the variance is:

$$\langle\Delta^2 N\rangle = \sum_k \sinh^2\left[G(\phi)\sqrt{\lambda_k(\phi)}\right]\cosh^2\left[G(\phi)\sqrt{\lambda_k(\phi)}\right]. \tag{4.22}$$

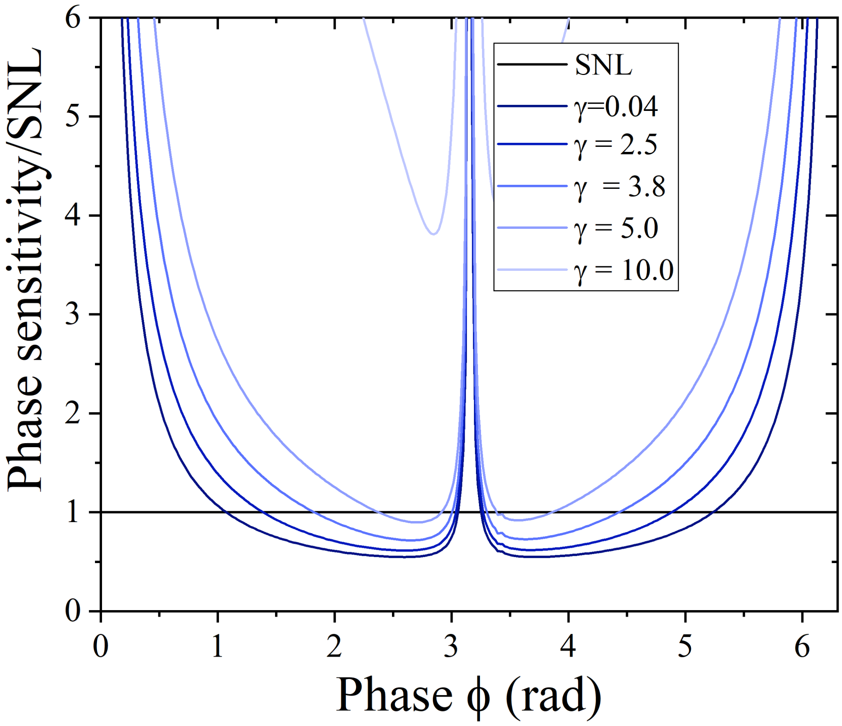

Figure 4.6: Phase sensitivity in relation with the phase at different gain. The SNL is plotted in black [3].

The normalized phase sensitivity of the SU(1,1) interferometer is plotted for different gain in Fig.4.6. Our analysis shows that the sensitivity achieved by this device is comparable with and even overcomes the SNL. In order to demonstrate this point, we compare the phase sensitivity achieved by using Eq.(2.57) with the SNL calculated for this interferometer via Eq.(2.58), where the internal number of photons corresponds to

$$\langle N_{in} \rangle = \sum_k \sinh^2 \left[G_1 \sqrt{\eta_k} \right], \tag{4.23}$$

where η_k are the Schmidt eigenvalues of the single periodically poled waveguide. In this expression $G_1 = \int C_1(\Gamma/2)dt$, is the experimental gain of one PDC and it is taken into account that the coupling constant of a single PDC section is twice smaller than the coupling constant of the double-PDC-section of the SU(1,1) interferometer; in this notation, C_1 is the normalization constant corresponding to the JSA of a single PDC section.

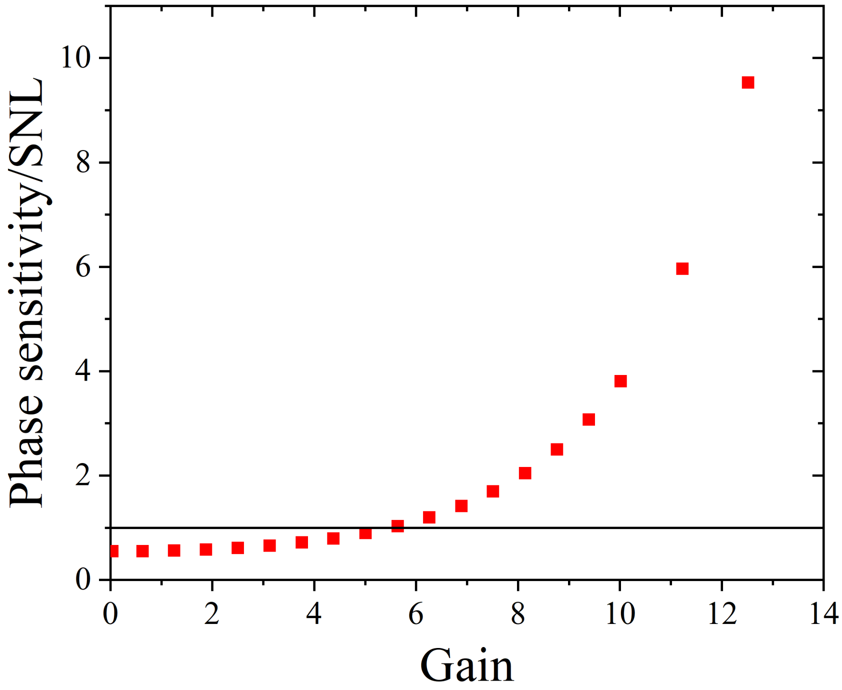

Figure 4.7: The minimum values of the normalized phase sensitivity presented in Fig.4.6 versus gain γ. The higher the gain, the faster the phase sensitivity grows. The SNL is plotted in black [3].

This is one of the main results of this work. In fact, according to this analysis we can state that it is possible to realize an integrated SU(1,1) interferometer whose phase sensitivity overcomes the SNL. Furthermore, the trend of the curves in Fig.4.6, and in particular the presence of the central peak at $\phi = \pi$, highlights the deep differences between the previous results presented in literature [66, 71, 78, 123] and the new results derived by the realistic model we delineated in this chapter. In this framework, the presence of this peak is due to fact that the relation $\overline{\Delta\beta} \simeq -\Delta\beta$ does not hold for higher order of the Taylor expansion, nor for high frequency detuning, namely $|\Omega| \gg 0$. As a consequence, residual photons emerge, causing the non-perfect interference and therefore also the non-vanishing photon number and variance in Eqs.(4.20) and (4.22) respectively. On the contrary, the derivative of the number of photon in Eq.(4.21) is exactly zero, making the phase sensitivity diverging at $\phi = \pi$. In this context it becomes clear that, despite our efforts, material dispersion still plays a crucial role in the modelling of realistic SU(1,1) interferometer, hindering the possibility of having a perfect interference and therefore higher sensitivity.

Explicit dependence on the gain

The graphs in Fig.4.6 evidently show that the interferometer can work beating the SNL, but it also presents a gradual worsening of the phase sensitivity for higher gain, until the curve entirely lies above the black line of the shot noise limit. A better perspective of this behaviour is traced by Fig.4.7, where the minimum of the normalized phase sensitivity is plotted at different gains.

The behaviour of the phase sensitivity at increasing gain can be analytically clarified. For the sake of simplicity, let us first distinguish two regimes: the low gain regime $G(0)\sqrt{\lambda_1(0)} \ll 1$, from the high gain regime, in which $G(0)\sqrt{\lambda_1(0)} \gg 1$. These two conditions are reached by manipulating the coupling constant Γ opportunely.

In case of low gain, both the output number of photons in Eq.(4.20) and the internal photon number in Eq.(4.23) can be Taylor expanded with respect to Γ, obtaining

$$\langle N(\phi)\rangle \simeq G^2(\phi)\sum_k \lambda_k(\phi) = G^2(\phi), \tag{4.24}$$

and

$$\langle N_{in}\rangle \simeq G_1^2 \sum_k \eta_k = G_1^2, \tag{4.25}$$

respectively. Similarly, we can apply a Taylor expansion on the variance,

$$\langle \Delta^2 N\rangle \simeq G^2(\phi)\sum_k \lambda_k(\phi) = G^2(\phi). \tag{4.26}$$

In all Eqs.(4.24) to (4.26) we took advantage of the normalization of the Schmidt eigenvalues. Also, it seems convenient to assume $C_1 \approx C(0)$ and $\lambda_k(0) \approx \eta_k$. These assumptions are based on the fact that the JSA in Eq.(4.16) at $\phi = 0$ in formally identical to the JSA of one PDC waveguide. By both calculating the new derivative of the photon state from Eq.(4.24) and assuming for the sake of simplicity $G(\phi) = G(0)|\cos(\phi/2)|$ (this expression holds at $0 < \phi < \pi$ in the low gain regime), we finally obtain the expression of the normalized phase sensitivity in the low gain regime:

$$\frac{\langle \Delta\phi\rangle}{\langle \Delta\phi_{SNL}\rangle} \approx \left| \frac{G(0)}{4}\left(\frac{\partial G(\phi)}{\partial \phi}\right)^{-1} \right| \approx \frac{1}{2\sin(\phi/2)}. \tag{4.27}$$

Such expression can be minimized in the proximity of $\phi = \pi$, reaching the value 0.5 for very low gain, as shown in Fig.4.7. Moreover, we notice that in the low gain regime there is no dependence of the normalized phase sensitivity on the parametric gain γ.

In order to investigate the behaviour of the normalized phase sensitivity in the high gain regime, we have to proceed in two different ways. In fact, in this regime the contribution of the first Schmidt mode becomes dominant, following a redistribution of the mode weights, namely the eigenvalues [52]. This allows us to momentarily reduce the amount of modes and focus our argumentation on the first Schmidt mode. This induces an underestimation of both photon numbers in Eqs.(4.20) and (4.23), becoming respectively

$$\langle N_s(\phi)\rangle \approx \sinh^2\left[G(\phi)\sqrt{\lambda_1(\phi)}\right], \tag{4.28}$$

and

$$\langle N_{in}\rangle \approx \sinh^2\left[G_1\sqrt{\eta_1}\right], \tag{4.29}$$

as well as of the variance in Eq.(4.13), whose expression is reduced to

$$\langle \Delta^2 N\rangle \approx \sinh^2\left[G(\phi)\sqrt{\lambda_1(\phi)}\right]\cosh^2\left[G(\phi)\sqrt{\lambda_1(\phi)}\right]. \tag{4.30}$$

By taking again advantage of the shape of the JSA in Eq.(4.16) at $\phi = 0$, we can write $C_1 \approx C(0)$ and $\lambda_k(0) \approx \eta_k$, and the parametric gain can be therefore expressed in terms of both single- and double-PDC parameters as

$$\gamma = G(0)\sqrt{\lambda_1(0)} \simeq 2G_1\sqrt{\eta_1}. \tag{4.31}$$

Finally, the modulation of the JSA in Eq.(4.16) by $\cos(\phi/2)$ allows us to write $G(\phi)\sqrt{\lambda_1(\phi)} \approx \gamma|\cos(\phi/2)|$, and we can rewrite the normalized phase sensitivity as

$$\frac{\Delta\phi}{\Delta\phi_{SNL}} \approx \frac{\sinh[\gamma/2]}{\gamma\sin(\phi/2)}. \tag{4.32}$$

Although this expression can explain the exponential growth of the curve in Fig.4.7, the strategy here adopted does not hold for any value of ϕ. Indeed, in the proximity of $\phi = \pi$ a flattening of the distribution of the eigenvalues occurs, causing all modes to contribute with the same weight. However, since the underestimation of the Schmidt modes is not fruitful around $\phi = \pi$, we can resort to another trick, namely overestimating the weight of the modes. In particular, we assume to have only K modes having all eigenvalue $\lambda_1(\phi)$. In this framework, $K = 1/(\sum_k \Lambda_k^2)$ is the effective number of modes (the Schmidt number) and

$$\Lambda_k = \frac{\sinh^2\left[G(\phi)\sqrt{\lambda_k(\phi)}\right]}{\sum_k \sinh^2\left[G(\phi)\sqrt{\lambda_k(\phi)}\right]} \tag{4.33}$$

is the new set of Schmidt coefficients taking into account the redistribution of the weights in the high gain regime [136]. This strategy allows us to rewrite both the photon number and the variance as

$$\langle N(\phi)\rangle \approx K\sinh^2\left[G(\phi)\sqrt{\lambda_1(\phi)}\right], \tag{4.34}$$

and

$$\langle \Delta^2 N\rangle = K\sinh^2\left[G(\phi)\sqrt{\lambda_1(\phi)}\right]\cosh^2\left[G(\phi)\sqrt{\lambda_1(\phi)}\right]. \tag{4.35}$$

We apply the same procedure to the SNL, obtain an expression for the internal number of photons very similar to Eq.(4.34). We conclude observing that the new strategy leads to the same expression achieved in Eq.(4.32). The optimization of this formula occurs in the proximity of $\phi = \pi$, and the behaviour of the normalized phase sensitivity can be finally rewritten by

$$\frac{\Delta\phi}{\Delta\phi_{SNL}} \approx \frac{\sinh[\gamma/2]}{\gamma}. \tag{4.36}$$

The expression above fully resumes the trend of the normalized phase sensitivity plotted in Fig.4.7: in the low gain, it tends to a constant value, i.e it does not dependent on the gain. On the contrary, it grows exponentially for higher gain beyond the SNL.

4.1.5 Filtering the JSA

Along this work the choice of the PDC as part of the SU(1,1) interferometer was supported because of the possibility to generate squeezing states in realistic experimental scenarios. Although this was helpful for the accomplishment of an accurate analysis of the realistic SU(1,1) interferometer, we faced that the presence of the spectra of both signal and idler photon drastically complicates the analysis of the performance of the interferometer. Yet it has become clear that a deep knowledge of the spectral features of the output radiation offers more perspectives in the improvement of the phase sensitivity. In this section we want to figure out whether the manipulation of the photon spectra has any influence on the phase sensitivity. In particular, we will test the performance of the interferometer after the filtering of a specific frequency range.

In principle, according to the results of last two sections, a sort of improvement has to be expected. Indeed, it was claimed that the presence of the central peak in Fig.4.6 was in good part due to the presence of residual photons for high detuning $|\Omega| \gg 0$. By filtering out high-detuned frequencies we expect a reduction of the output intensity which is more remarkable in the proximity of $\phi = \pi$, where the interference pattern is more sensible to the presence of red and blue (with respect to $\omega_p/2$) photons. In the end, the filter should cause a slight enhancement of the visibility and therefore an improvement of the phase sensitivity.

In order to demonstrate the validity of our hypothesis, we estimate the phase sensitivity of the SU(1,1) interferometer when only a specific portion of the spectrum is counted, whereas the leftover radiation is filtered out. Mathematically, this means to calculate both the photon number and the variance in one specific range of frequency. In this framework, the employment of the output Schmidt operators is not fruitful, since they are already integrated with respect to the whole frequency range. On the contrary, we make use of the plane wave basis introduced in Eq.(2.44) [52], and integrate the average of the signal photon number in a specific range of frequency around $\omega_p/2$:

$$\begin{aligned}\langle N_s(\phi)\rangle &= \int_{\omega_p/2-\delta}^{\omega_p/2+\delta} d\omega_s \langle a_s^{\dagger out}(\omega_s) a_s^{out}(\omega_s)\rangle \\ &= \sum_k \sinh^2\gamma_k \int_{\omega_p/2-\delta}^{\omega_p/2+\delta} d\omega_s |u_k(\omega_s,\phi)|^2,\end{aligned} \tag{4.37}$$

where δ determines the filter bandwidth and $\gamma_k = G(\phi)\sqrt{\lambda_k(\phi)}$. The variance is calculated

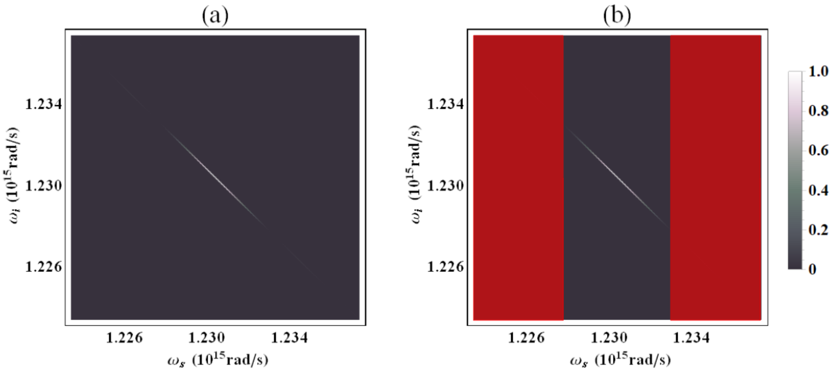

Figure 4.8: The normalized JSI at $\phi = 0$: (a) without filter, (b) with the filter (bandwidth $5.71{\cdot}10^{12}$ rad/s) [3].

following the same procedure:

$$\begin{aligned}\langle \Delta^2 N_s(\phi)\rangle &= \langle N_s(\phi)\rangle \\ +\sum_{kk'} &\left| \int_{\omega_p/2-\delta}^{\omega_p/2+\delta} d\omega_s u_k^*(\omega_s,\phi) u_{k'}(\omega_s,\phi) \sinh\gamma_k \sinh\gamma_{k'} \right|^2, \end{aligned} \tag{4.38}$$

where the first term corresponds to Eq.(4.37). The phase sensitivity can be evaluated via Eq.(2.57), calculating firstly the derivative of Eq.(4.37).

Before giving an estimation of the phase sensitivity in comparison with the SNL, it is fundamental to recount also the internal number of photons following the filtering. In this circumstance, this number corresponds to the photons leaving a single PDC section and subjected to a band-pass filter before entering the phase modulator, namely

$$\langle N_{in}\rangle = \sum_k \sinh^2[G_1\sqrt{\eta_k}] \int_{\omega_p/2-\delta}^{\omega_p/2+\delta} d\omega_s |\bar{u}_k(\omega_s)|^2, \tag{4.39}$$

where $\bar{u}_k(\omega_s)$ is the orthonormal set of signal Schmidt modes corresponding to a single periodic poled waveguide.

The specific filter we used in our model, applied on the signal photon, covers the main body of the JSA around $\omega_p/2$ (see Fig.4.8a) and cuts the side-lobes of the sinc function (Fig.4.8b). In this case, the selected filter bandwidth is $2\delta = 5.71 \cdot 10^{12} rad/s$. As mentioned in the beginning of this section and shown in Fig.4.8b, this choice allows us to exclude the portion of radiation having large detuning. The phase sensitivity calculated via Eq.(2.57) and normalized by the SNL calculated via Eq.(4.39) is plotted for different gains in Fig.4.9.

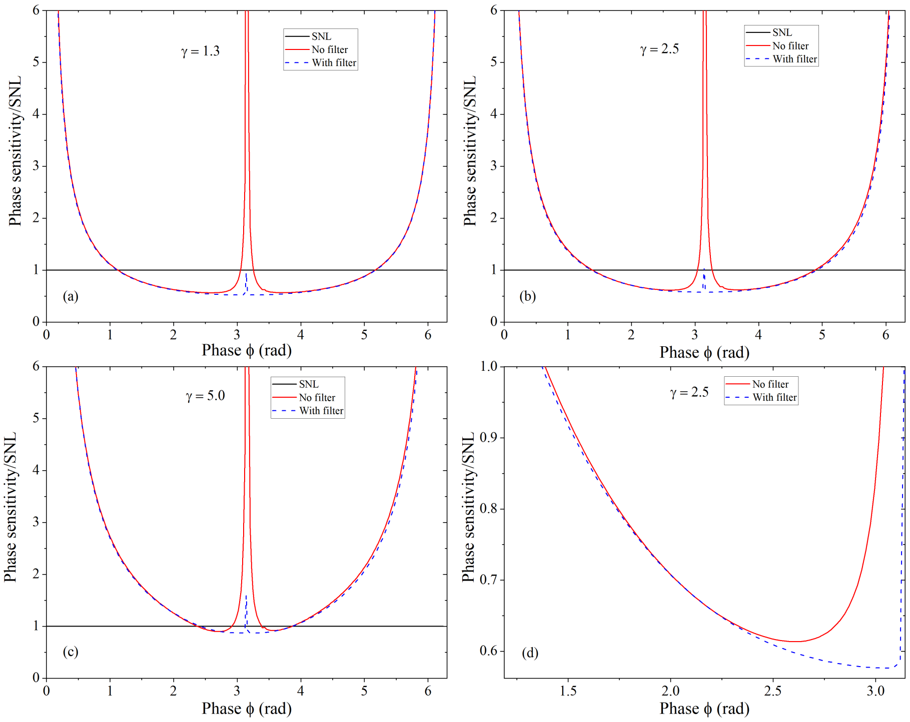

Figure 4.9: The normalized phase sensitivity with and without a filter for different gains: (a) $\gamma = 1.3$, (b) $\gamma = 2.5$ and (c) $\gamma = 5.0$. (d) The zoom of the supersensitivity region for $\gamma = 2.5$. The solid red line shows the case without a filter, the dashed blue line presents the filter case [3].

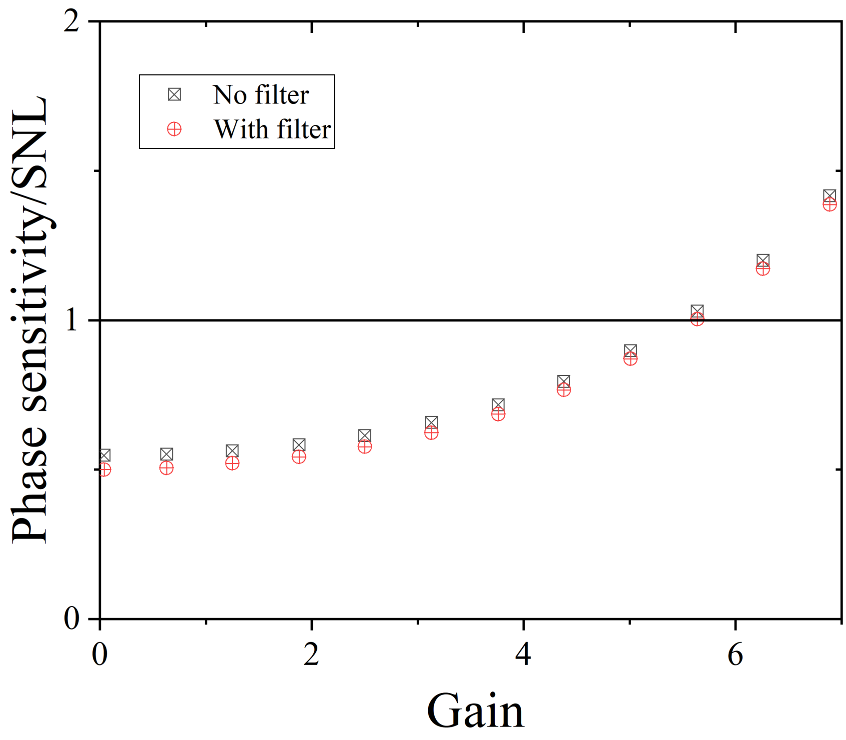

Figure 4.10: The minimum values of the normalized phase sensitivity versus gain γ with and without the use of the filter. The SNL is represented by a solid black line [3].

From the comparison with the no-filter case in Section 4.1.4, these graphs bring to light the overlap of the no-filter (red) curve and the filter (dotted blue) curve as long as the phase ϕ assumes values far from π. This behaviour is not surprising: as long as $\phi \neq \pi$, the JSA holds its shape in Fig.4.8a and both variance and photon number keep their functional trend with respect to the phase.

On the contrary, in proximity of π the phase sensitivity experiences a new trend. In particular, Fig.4.9d highlights the drastic reduction of the peak width, inducing both a deepening of the minimum of the curve and a widening of the supersensitivity range, hence a global improvement of the phase sensitivity. As mentioned in the beginning of this section, this result stems from the reduction of the remarkable influence of high-detuned frequencies in the photon counting, quite determinant at $\phi \simeq \pi$. However, the central peak at $\phi = \pi$ cannot vanish at all. Although the filter drastically suppresses part of the fluctuation of the JSA for high frequency detuning, some noise remains around $\omega_p/2$, stemming also from second order effects.

Finally, the minima of the phase sensitivity curves is plotted for different gain in Fig.4.10. Here the comparison shows the improvement of the sensitivity in case of filtering by comparison with the no-filer case. However, the exponential worsening at higher gain persists, until the phase sensitivity lies entirely over the SNL line.

4.1.6 Conclusion

The complexity of the system we are testing along this chapter, mainly due to the spectral features of the photon sources as well as our design in a integrated device, required a detailed analysis of the JSA, mostly focussed on an accurate phase matching construction.

As first configuration, we described the JSA of a integrated SU(1,1) merely consisting of two periodic poled PDC sections, spatially separated by a non-poled section made of the same material (KTP). Although this intuitive model allows to achieve a modulation of the JSA, it is not particularly fruitful for phase sensing tests, because the interference fringes stemming from the modulation of the photon number would have a very scarce visibility.

In order to drastically increase the visibility of the intensity modulation, a structural change of the SU(1,1) interferometer was performed, in particular, a polarization converted was added along the waveguide in order to reduce the mismatch of signal and idler photons caused by dispersion. The modifications on the phase matching function due to the presence of the PC, along with the use of a CW laser, cause a drastic improvement of the fringe visibility, illustrated by a photon number profile tending to zero at $\phi = \pi$. Consequently, the phase sensitivity calculation yielded promising results, in which the phase sensitivity of the SU(1,1) interferometer beats the SNL and a wide supersensitivity region is achieved.

Finally, we explored the effect of both different gains and filters. It was seen that the normalized phase sensitivity increases for higher gain with a damped exponential trend. On the other hand, filtering the JSA seems to induce positive effects, corresponding to both a broadening and a deepening of the supersensitivity region with respect to the no-filter case.

4.2 Seeding the multimode SU(1,1) interferometer

4.2.1 Introduction to the seeding strategies

The transition from a single-mode to the multimode description of the SU(1,1) interferometer along this chapter was quite challenging and has highlighted the presence of many problems and difficulties to take into account. Another element we still have to consider in our multimode framework is the possibility of seeding the interferometer. We already know that the use of seeds in interference scenarios is a common practice in quantum interferometry and quantum metrology. In this section we will see that the concept of seeding the spectrally multimode interferometer is a non-trivial point that must be clarified.

The seeding of the SU(1,1) interferometer was introduced along this work in Section 2.2.6, where a coherent state was used as seed in the single mode description. It is clear that the presence of a seed can modify the outcome of the phase sensing test. For instance, in [71] the coherent state applied in one of the two channel of the interferometer makes the supersensitivity region narrower in comparison with the no seeding case. However, other tests like in [66] or [78] show that coherent states as seed certainly allows to break the SNL, getting a even better phase sensitivity for higher gain. This argument holds when different seeding states are used in the input doors as well, for instance a mix of coherent and squeezed states as suggested in [123].

It is clear that, once the deep differences with respect to the single mode investigation are clarified, we should wonder how we can introduce the seed in the multimode framework and which kind of benefits we can achieve from this choice. In fact, the number of seeding combinations in a spectrally multimode framework is effectively countless. We can notice that the orthonormality of the Schmidt modes as well as the spectra of both signal and idler photons put forth several seeding scenarios, which could not be explored in the single mode framework. In simple words, the multimode SU(1,1) interferometer makes the seeding choice far to be a trivial issue.

By taking advantages of the complexity of our system, we will test two specific strategies: "mode seeding" and "frequency seeding". The former consists of an input state in the Schmidt basis, in particular we create a seed state in one of the spectral modes of the interferometer. In future, one can imagine to extend this case by selecting combinations of different modes. The latest concerns the presence of an input plane wave mode at one selected frequency. A more general case can be analysed in future work, where multicolour seeds can be envisaged.

Lastly, the possibility of seeding the mutimode SU(1,1) interferometer opens the door to the use of alternative detection strategies, which drastically amplify the possible scenarios to explore. In this section, we will mainly focus on two detection strategies. The first one, which will be develop in the first part of the section and already extensively utilized along this work, is the direct detection. The second one, which will be introduced properly in the last part of this section, is the homodyne detection. In all cases we will consider seeding inputs in the signal mode of the interferometer.

4.2.2 Direct detection

The first strategy we are going to test was called "mode seeding" and consists in preparing an input state in one of the spectral mode of the interferometer[2]. More precisely, we will seed the first Schmidt mode with one photon and with a bright coherent state.

Seeding the first Schmidt mode with one photon

As first case, let us suppose to seed one channel of the interferometer with only one photon in the first Schmidt mode. This can be mathematically expressed as:

$$|\psi\rangle_{in} = |1\rangle_{A_1}|0\rangle_{A_{n\neq 1}}|0\rangle_{B_n}, \tag{4.40}$$

where we explicitly indicated the presence of one photon in the first channel of the interferometer prepared in the first Schmidt mode. All other input modes are not seeded. Since we did not change the detection strategy, we can make use of the same procedure used so far. We can therefore start calculating the number of photons:

$$\langle N\rangle = \sum_k \sinh^2\gamma_k + 1 + \sinh^2\gamma_1 \tag{4.41}$$

where $\gamma_k = 2G(\phi)\sqrt{\lambda_k(\phi)}$. In this formula we can immediately recognise the first term, being the vacuum contribution already known in Eq.(4.20), whereas both second and last term are direct consequences of the seeding choice: the second term merely corresponds to the additional photon due to the seeding, and the last term identifies the surplus of photons due to te interaction of such photon with the sources. Naturally, further changes are also observed in the photon variance:

$$\langle\Delta^2 N\rangle = \sum_k \sinh^2\gamma_k\cosh^2\gamma_k + \sinh^2\gamma_1\cosh^2\gamma_1, \tag{4.42}$$

where the last term raises because of the seeding choice.

By performing the derivative of Eq.(4.41), we are now able to calculate the normalized phase sensitivity, which is plotted in Fig.4.11. Although this picture seems to present results comparable with Fig.4.6, a worsening in the phase sensitivity is immediately observable, and it becomes even more clear by looking at Fig.(4.12), where we plotted the minimum of the phase sensitivity by fixing different gains. In particular, it is evident a divergent trend for small gain, in contrast with the no seeding case.

---

[2] It is crucial to notice that all output Schmidt mode profiles depend on the phase. This dependence becomes more evident for values around $\phi = \pi$, namely when the light intensity dramatically drops and spectral irregular behaviours emerge, and this should be taken into account in eventual future experimental testing.

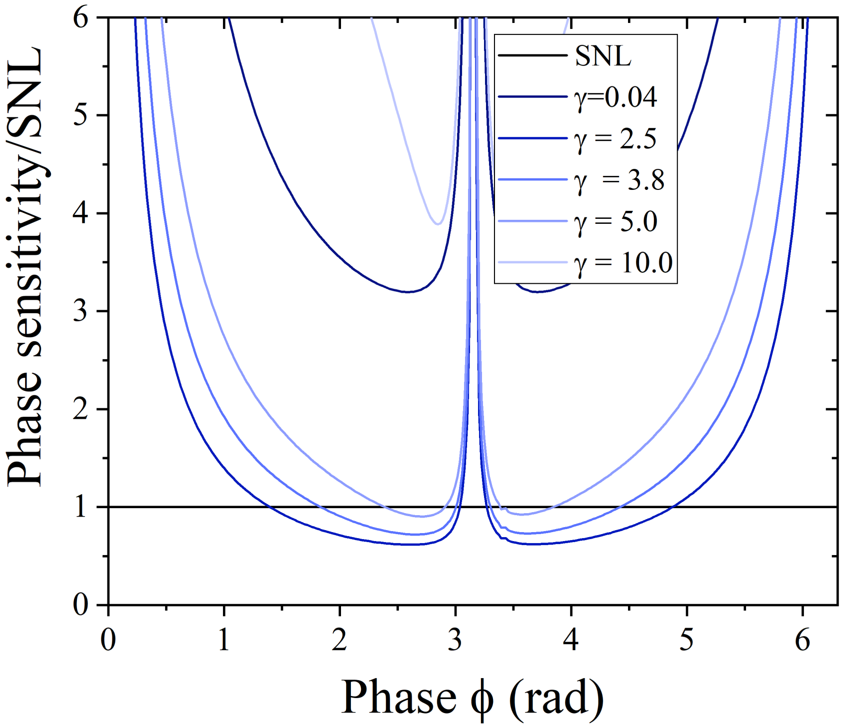

Figure 4.11: Phase sensitivity in relation with the phase at different gain when the first mode is seeded with 1 photon. The SNL is plotted in black. Length of the PDC sections was $L_{PDC} = 8mm$, pump laser wavelength $\lambda_p = 766nm$, pulse duration $t = 100ps$ [3].

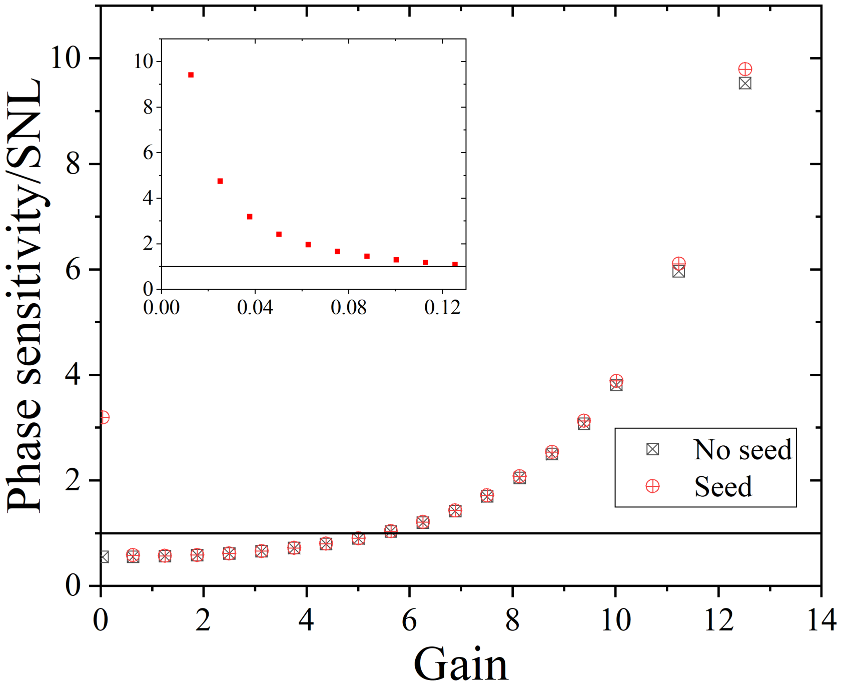

Figure 4.12: The phase sensitivity trend in Fig.4.11 at the point of minimum with respect to the gain (red circles) compared to the no-seeding case (black squares). The SNL is plotted in black. The insert shows the zoom of the phase sensitivity in the seeded case for small gains [3].

This behaviour mathematically stems from the combination of different factors: by calculating the shot noise limit,

$$\Delta\phi_{SNL} = \frac{1}{\sqrt{1 + \sinh^2[G_{sc}\sqrt{\eta_1}] + \sum_k \sinh^2[G_{sc}\sqrt{\eta_k}]}}, \tag{4.43}$$

we can see that for lower gain the second and the third term inside the square root become negligible, and the SNL tends to the unity. On the other hand, the phase sensitivity still scales as $1/\Gamma$, as we proved in Section 4.1.4. This explains why the normalized phase sensitivity diverges for low gain. The divergence for higher gain is still motivated by the fact that the normalized phase sensitivity function grows exponentially, and the presence of one additional photon in the high gain regime does not lead to any dramatic changes.

Seeding the first Schmidt mode with a coherent state

The case analysed above demonstrates that working in the Schmidt basis is conceptually similar to having an infinite set of inputs for both doors of the interferometer. These inputs can be treated independently, and one can use different statistics for seeding them individually. As a further example, our next step consists in using a coherent state rather than a single photon seed. In order to investigate this case mathematically, we start again defining the current input state:

$$|\psi\rangle_{in} = |\alpha\rangle_{A_1}|0\rangle_{A_{n\neq 1}}|0\rangle_{B_n}, \tag{4.44}$$

where α^2 is a real parameter corresponding to the number of coherent photons, having therefore a Poissonian distribution. We assume that the number of coherent photons are equal to one million henceforth. We expect that such huge value drastically modify the outcome. Indeed, the difference becomes significant by looking at the photon number,

$$\langle N\rangle = \sum_k \sinh^2\gamma_k + |\alpha|^2 + \alpha^2\sinh^2\gamma_1, \tag{4.45}$$

where we can immediately see that last two terms are predominant with respect to the fist one due to the presence of α^2. In a low gain regime, the first term becomes negligible. Instead, we need to strongly pump the PDC in order to make the second term negligible. Similar considerations can be done by looking at the internal number of photons, contained in the shot noise limit:

$$\Delta\phi_{SNL} = \frac{1}{\sqrt{\alpha^2\cosh^2[G_1\sqrt{\eta_1}] + \sum_k \sinh^2[G_1\sqrt{\eta_k}]}}, \tag{4.46}$$

where it is clear that the first term inside the square root is dominant in the low and middle gain regime. Another remarkable difference with respect to the single photon seeding is the variance:

$$\langle\Delta^2 N\rangle = \sum_k \sinh^2\gamma_k\cosh^2\gamma_k + \alpha^2\cosh^2\gamma_1\cosh 2\gamma_1, \tag{4.47}$$

where the second term looks very different from the relative one in Eq.(4.42). However, as it is shown in Fig.4.13 this choice does not provide any meaningful outcome. Despite the possibility of modifying the output by varying the gain parameter, all values of the phase sensitivity lies above the SNL, making this seeding choice unworthy with this type of detection.

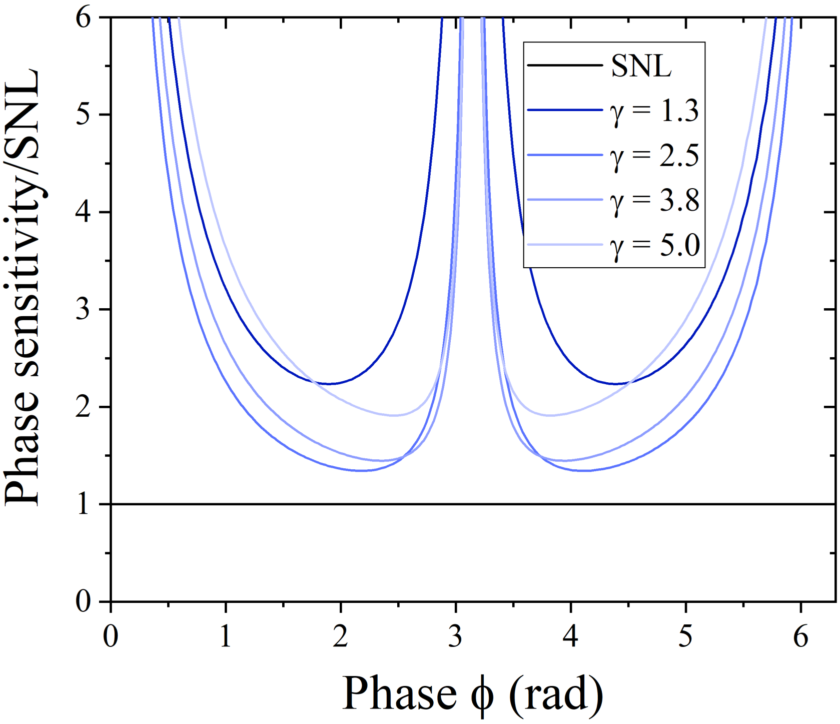

Figure 4.13: The normalized phase sensitivity on the phase for different gains. The first Schmidt mode of the signal photon is seeded with an intense coherent state having $|\alpha|^2 = 10^6$ photons. The SNL is represented by a solid black line [3].

This behaviour is proved mathematically, by making use of the assumption $\alpha^2 \gg \sum_k \sinh^2 \gamma_k$, namely imposing that the number of coherent photons is much higher than the number of squeezing photons generated by the PDC. This approximation holds in both low and middle gain regimes, which are the regimes we are interesting in, being the phase sensitivity divergent for higher gains. We can therefore firstly calculate the derivative of N, which is:

$$\left|\frac{\partial\langle N\rangle}{\partial\phi}\right| \approx |\alpha|^2 \cosh 2\gamma_1 \frac{\partial\gamma_1}{\partial\phi}, \tag{4.48}$$

whereas the variance is reduced to:

$$\langle\Delta^2 N\rangle \approx |\alpha|^2 \cosh^2\gamma_1 \cosh 2\gamma_1. \tag{4.49}$$

In this regime, also the SNL can be approximated:

$$\Delta\phi_{SNL} \approx \frac{1}{\sqrt{\alpha^2 \cosh^2[C\sqrt{\eta_1}]}}, \tag{4.50}$$

and by collecting all these elements we can write down a reduced expression of the normalized phase sensitivity:

$$\frac{\Delta^2\phi}{\Delta^2\phi_{SNL}} \approx (1+\coth^2\gamma_1)\cosh^2\left[G_1\sqrt{\eta_1}\right]\left|\frac{\partial\gamma_1}{\partial\phi}\right|^{-2}. \tag{4.51}$$

The similarity between the JSA in Eq.(4.16) at $\phi = 0$ and the JSA of a single waveguide offers us the possibility to assume $\lambda_1(0) \simeq \eta_1$ and $G(0) \simeq 2G_1$; hence the gain γ can be expressed as $\gamma \simeq 2G_1\sqrt{\eta_1}$. Moreover, the modulation of the gain can be simplified as $\gamma_1 \approx \gamma|\cos(\phi/2)|$, therefore in the range $\{0-\pi\}$ we have

$$\frac{\Delta^2\phi}{\Delta^2\phi_{SNL}} \approx \frac{4\left(1+\coth^2[\gamma\cos(\phi/2)]\right)\cosh^2[\gamma/2]}{\gamma^2\sin^2(\phi/2)}. \tag{4.52}$$

and a plot of this formula (or alternatively a calculation of the minimum point with respect to the variable ϕ) shows that there is no value of γ letting the phase sensitivity overcome the SNL.

A last chance to get an improvement of the supersensitivity region with this seeding choice is given by a different detection strategy, which will be the topic of next section.

4.2.3 Homodyne detection

The possibility of seeding encourages us to explore other suitable solutions for estimating the phase sensitivity of the multimode SU(1,1) interferometer. One way is to take advantage of coherent seeding states by adopting another detection strategy, for instance the homodyne detection. The first consequence linked with this choice, is the modification of the definition of phase sensitivity, which is not related to the photon number anymore but to the homodyne operator:

$$\Delta\phi = \left|\frac{|\Delta H_d|}{\partial\langle H_d\rangle/\partial\phi}\right|. \tag{4.53}$$

Along this section we will experience that the form of such operator depends on the seeding state of the interferometer. In Section 2.2.4, and more precisely in Eq.(2.68), it was seen that the homodyne operator H_d is linearly proportional to the creation and annihilation operators; this forces us to deal with coherent input states, i.e. eigenstates of a and $a^\dagger$, since the mean values of H_d would return zero in case of seeded Fock states.

It is important to recall that the homodyne detection makes uses of an additional beam, called local oscillator. In our multimode scenario, it is crucial to make sure that the output light of the SU(1,1) interferometer and the local oscillator are spectrally matched. In order to ensure this, both the LO and the signal leaving the interferometer undergo the same filtering.

The spectral characteristic of the filters are modelled in accordance with the different types of seeding states. We will consider two cases: firstly, we will use for the last time the seed in the first Schmidt mode, while in the last example we will consider a passband filter around the central frequency of generated squeezed light. We stress that the SNL calculation takes these modifications into account as well: the mean number of photons in the SNL corresponds to the number of signal photons generated by a single periodically poled waveguide, averaged with respect to the input seeding state, and then filtered to match the spectral properties of the output squeezed light.

Seeding the first Schmidt mode with a coherent state

As first case, we consider a seed state like Eq.(4.44), where the first Schmidt mode contains $\alpha^2 = 10^6$ Poissonian distributed photons, with again $\alpha \in \mathbb{R}$. The detection scheme is sketched in Fig. 4.14.

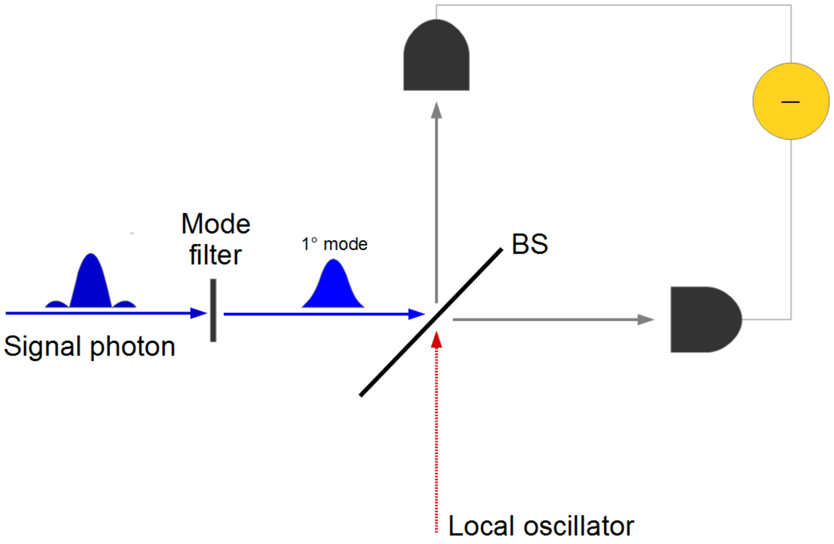

Figure 4.14: Filter in the first Schmidt mode A_1 and homodyne detection scheme. The LO spectrum is characterized by the same frequency distribution.

In this model, the signal photon leaving the interferometer passes through a filter, where all but the first Schmidt mode is filtered out. In this way, the spectrally single mode signal photon is subject to the homodyne detection: the incoming radiation interacts in a balanced BS with the local oscillator characterized by the same frequency range of signal; then, both beams leaving the BS reach two detectors, and the intensity difference between the detected radiation is estimated. Mathematically, by indicating with b, c, and d the annihilation operators of the LO and the two output BS channels respectively, this is resumed by

$$c_1^\dagger c_1 - d_1^\dagger d_1 = A_1^\dagger b_1 - b_1^\dagger A_1, \tag{4.54}$$

where the index 1 stems from the filter with respect to the first Schmidt mode. By tracing out the LO and rewriting we get an expression for the homodyne operator

$$\hat{H}_d = |\beta_{lo}| \left(e^{i\theta_a} \hat{A}_1^{out} + e^{-i\theta_a} \left[\hat{A}_1^{out} \right]^\dagger \right), \tag{4.55}$$

where we introduced $|\beta_{lo}|$ and θ_a, namely the amplitude and the phase of the local oscillator described by the coherent state $||\beta_{lo}|e^{i\theta_a}\rangle_{A_1}$. As already mentioned, the spectral bandwidth of the LO matches the bandwidth of the first Schmidt mode.

By following the usual procedure, in order to estimate the phase sensitivity we need to calculate the average value of Eq.(4.55):

$$\langle \hat{H}_d \rangle = 2|\beta_{lo}| \cos\theta_a \cosh\gamma_1, \tag{4.56}$$

the variance of the homodyne operator:

$$\langle \Delta^2 H_d \rangle = |\beta_{lo}|^2 \cosh 2\gamma_1, \tag{4.57}$$

and the expression of the SNL:

$$\Delta\phi_{SNL} = \frac{1}{\sqrt{1 + \sinh^2[C_1\sqrt{\eta_1}] + \sinh^2[C_1\sqrt{\eta_1}]}}. \tag{4.58}$$

The normalized phase sensitivity can be optimized for $\theta_a = 0$, and its trend is very closely described by Fig. 4.13. This means that this seeding does not show a supersensitivity region. This last test concludes the experience of seeding the first Schmidt mode.

Seeding the central frequency $\omega_p/2$

The second seeding case we want to investigate via homodyne detection concerns an input state characterized by a coherent state in the central frequency $\omega_p/2$. The adapted scheme is sketched in Fig. 4.15.

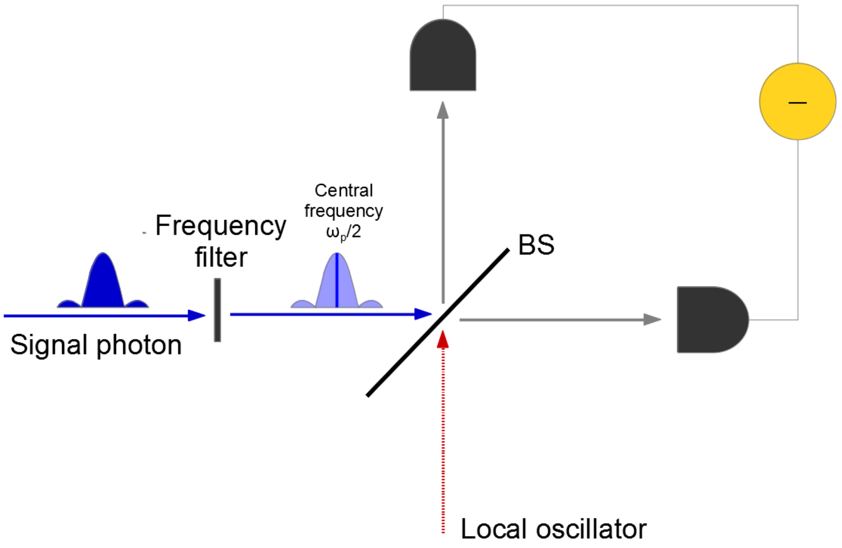

Figure 4.15: Filter in the central frequency $\omega_p/1$ and homodyne detection scheme. The LO is set in the same frequency of signal photon.

In this new scenario, the light leaving one of the two channels of the interferometer is subjected to a frequency filter, isolating the central frequency $\omega_p/2$. We make sure again that the range of frequencies of the LO and the output signal match.

Mathematically, the input state of the detection scheme is described by

$$|\psi\rangle_{in} = \int d\omega_s \delta(\omega_s - \omega_p/2)|\alpha\rangle_{\omega_s}|0\rangle_{\omega_i}, \tag{4.59}$$

where the coherent state contains again one million photons. Following the typical procedure already used in Eq.(4.55), we firstly need to calculate the difference between the detected intensities:

$$c^\dagger c - d^\dagger d = -i(a^{out})^\dagger \left(\frac{\omega_p}{2}\right) b + i b^\dagger a^{out} \left(\frac{\omega_p}{2}\right), \tag{4.60}$$

where $a^{out}(\omega_p/2)$ and $(a^{out})^\dagger(\omega_p/2)$ are the annihilation and creation operators expressed in the plane wave mode at the filtered central frequency, introduced in Eq.(2.44). Hence, we can now trace the LO information out and define the new homodyne operator:

$$\hat{H}_d = |\beta_{lo}| \left(e^{i\theta_a} \hat{a}^{out} \left(\frac{\omega_p}{2}\right) + e^{-i\theta_a} \left[\hat{a}^{out} \left(\frac{\omega_p}{2}\right)\right]^\dagger \right), \tag{4.61}$$

so that we can calculate its average value,

$$\langle \hat{H}_d \rangle = 2\alpha |\beta_{lo}| \cos\theta_a \left(1 + \sum_k \left| u_k \left(\frac{\omega_p}{2}\right)\right|^2 (\cosh\gamma_k - 1) \right), \tag{4.62}$$

and the variance,

$$\langle \Delta^2 \hat{H}_d \rangle = |\beta_{lo}|^2 \left(1 + 2\sum_k \left| u_k \left(\frac{\omega_p}{2}\right)\right|^2 \left| v_k \left(\frac{\omega_p}{2}\right)\right|^2 \sinh^2\gamma_k \right). \tag{4.63}$$

The shot noise limit is calculated by counting the internal number of photons subject to the same filter:

$$\begin{aligned} N_{in} = \alpha^2 + \sum_k \left| \bar{u}_k \left(\frac{\omega_p}{2}\right)\right|^2 \sinh^2[G_1\sqrt{\eta_k}] + 2\alpha^2 \sum_k \left| \bar{u}_k \left(\frac{\omega_p}{2}\right)\right|^2 (\cosh[G_1\sqrt{\eta_k}] - 1) \\ + \alpha^2 \left[\sum_k \left| \bar{u}_k \left(\frac{\omega_p}{2}\right)\right|^2 (\cosh[G_1\sqrt{\eta_k}] - 1) \right]^2 . \end{aligned} \tag{4.64}$$

By carrying the derivative of Eq.(4.62) we can estimate the normalized phase sensitivity of the SU(1,1) interferometer, which is optimized for $\theta_a = 0$, and finally plotted in Fig.4.16. The minimum values of the phase sensitivity for different gains are presented in Fig.4.17.

Also this seeding strategy does not lead to any advantage with respect to the no-seed case investigated in the beginning of this chapter. In particular, we do not observe any supersensitivity for any values of the phase. The possible reason explaining the lack of supersensitivity in all cases analysed above is that the seed in only one input channel of the interferometer with a high number of photons creates an imbalance between signal and idler photons, leading to a weakening of their correlations. This would cause a reduction of the phase sensitivity.

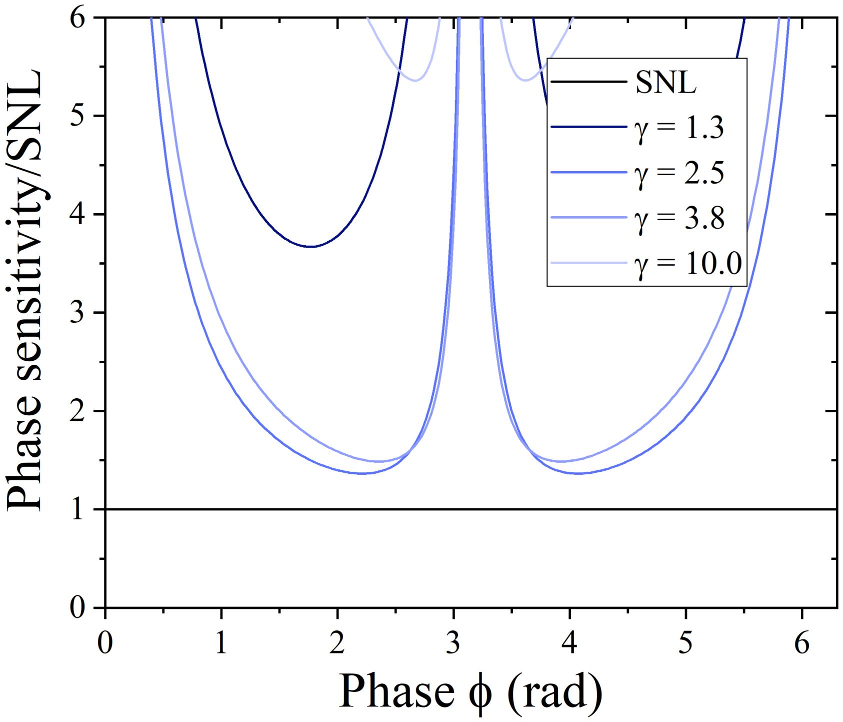

Figure 4.16: The normalized phase sensitivity in relation to the phase. The plane wave mode with the frequency $\omega_p/2$ is seeded by the intense coherent light having $|\alpha|^2 = 10^6$ photons. The SNL is represented by a solid black line [3].

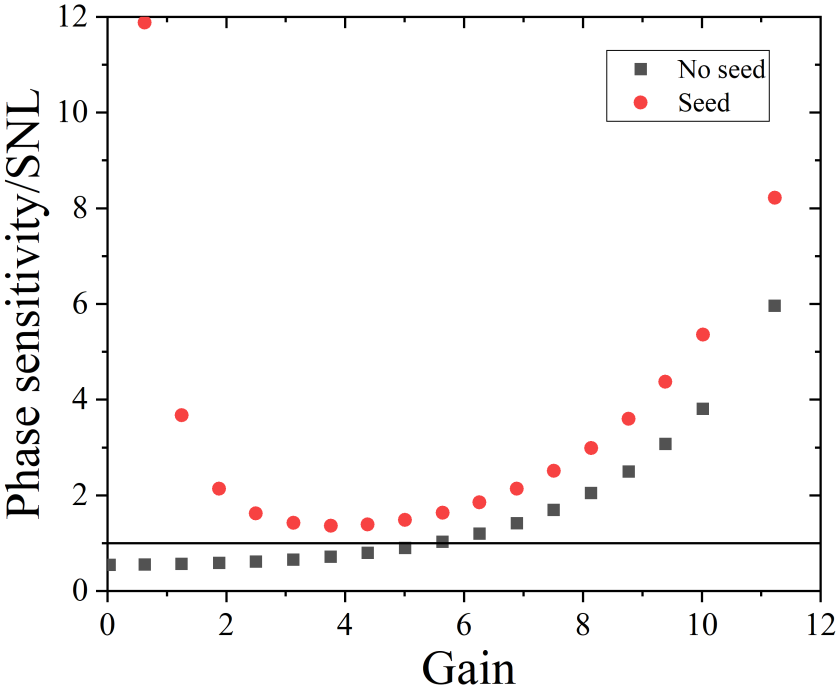

Figure 4.17: The minimum values of the normalized phase sensitivity presented in Fig. 4.16 versus gain (red circles) compared to the no-seeding case (black squares). The SNL is plotted in black [3].

4.2.4 Conclusion

In linear interferometry seeding is a fundamental way to test the interferometer: an example was the Mach-Zehnde interferometer in Section 2.2.5. In contrast, it was seen that the use of nonlinear optical parametric amplifiers ensures the presence of photons inside the interferometer even without any seeds. However, also in nonlinear interferometry one can imagine to elaborate a seeding strategy in order to test the performances of the interferometer.

One of the most interesting advantages of including the spectral information of the photon sources in the phase sensing investigation is the possibility of accessing to a large selections of seeding strategies: examples are polarization seeding, frequency seeding, spectral mode seeding, and so on.

In our investigation, we opted for two specific choices: selecting one input channel of the interferometer, we seeded once the first Schmidt mode, and then the central frequency of the PDC. The first Schmidt mode seeding was tested in different schemes: with the employment of the direct detection we seeded the interferometer with both one photon and a bright coherent state. The latest case was tested also with the homodyne detection. In all cases, a worsening of the phase sensitivity was observed with respect the no-seed case. The seed in the central frequency, calculated only via homodyne detection, leaded to similar results. The worsening of the normalized phase sensitivity is due to the reduction of correlation between signal and idler photons, caused by the disparity in the number of signal and idler photons.

Chapter 5

Conclusion and Outlook

In this thesis we investigated the influence of the spectral features of the light in different interference scenarios. We considered both linear and nonlinear interference frameworks, using parametric down conversion (PDC) effect as spectrally multimode photon source.

The material of the waveguide where the PDC effect occurs played a fundamental role along this work, so the choice was largely pondered. In the end, we conveniently opted for periodic poled Potassium titanyl phosphate (ppKTP) waveguide. This choice gained different advantages inherently our scopes. Firstly, KTP is a nonlinear material presenting the phase matching function almost diagonally oriented in the spectral domain. By opportunely tailoring the pump laser, this allows to have an almost circular joint spectral intensity (JSI), meaning that we can reduce the number of spectral modes to one without making use of particular filters. By reducing the pump bandwidth, we were able to increase both the symmetry of the JSI along the signal-idler antidiagonal and the number of spectral modes.

The first part of this manuscript was focussed on a specific linear interference framework, in particular we extended the design typically used in the two-photon Hong-Ou-Mandel (HOM) interference by enhancing the number of photons up to four. Mathematically, this was done by Taylor expanding the PDC state up to the second order, where two pairs of signal-idler photons are created.

We manipulated the amount of correlation between the two photons either by increasing the pulse duration of the pump laser (shrinking of the spectral bandwidth), and consequently by increasing the symmetry of the JSI, or by adding a quadratic phase in the pump spectral function and therefore holding the asymmetry with respect the antidiagonal in the frequency diagram: this choice allows to identify the origin of the deformation of P_{22} univocally. Although we would spontaneously tend to associate the probability of having two photons in both outputs of the interferometer P_{22} to the well known coincidence P_{11} of the two photon interference, in case of balanced BS these two probabilities do not show similar profiles at all. Moreover, this difference is accentuated by the further dependence of P_{22} on the number of temporal modes. Indeed, by increasing the Schmidt number either via reducing the pump bandwidth or via the presence of the quadratic phase in the pump profile, the probability presents a gradual enhancement of the central point at zero time delay, triggering a transition from a bunching deep to an antibunching peak. The experiments clearly showed this transition, in good agreement with our theoretical analysis. Instead, both visual and physical similarities with respect to the two-photon HOM dip were observed in the probability of having an odd number of photons in both channel, P_{3113}. Moreover, also in this probability curve the dip lies at or slightly over zero, depending on whether the spectra of signal and idler photons are identical or not.

In order to make the coincidence probability P_{22} comparable to the typical two-photons HOM dip P_{11}, specific values of transmission and reflection coefficients were set in the BS. The similarity between the two curves holds in the single mode regime, even showing a soft improvement of the visibility in P_{22}. However, stronger correlations between signal and idler photons break this similarity: the two-photon dip reaches its minimum point at zero, whereas the visibility of P_{22} decreases for higher correlations.

The four-photon HOM interference via state engineering prompted further investigations in the context of the spatial entanglement. This can be achieved by triggering a superposition of the two orthogonal polarizations before the light entering the interferometer. Due to the entanglement between the two channels of the interferometer, the coincidence probability changed dramatically, and in particular, fast oscillations came out. By a further analysis we noticed that the complex structure of these oscillations is connected with a hidden interference occurring between the terms inside the interferometer characterized by an even number of photons in each channel. However, the possibility to control the various elements guided us to exploit the potentiality of our interferometer. For instance, we could build different combinations of four dimensional Bell states by properly manipulating both the conversion parameter of the polarization converter and the transmission/reflection coefficient of the beam splitter.

Furthermore, we demonstrated that by making both the real and the imaginary part of the spectra of both signal and idler photons identical, we were able to generate fringe pattern whose period is reduced up to the half of the pump wavelength. It is also quite interesting to notice that this new pattern enables to create a balanced overlap between the initial state with two photons in both input channels and a NOON state with N=4. This superposition is not localized at zero time delay, but it occurs periodically in the coincidence probability.

In the second main part of this thesis, we adapt the theory of the Schmidt decomposition in PDC waveguide to the formalism of quantum metrology. More specifically, we elaborated an integrated nonlinear interferometer based on two realistic PDC platforms employed as optical parametric amplifiers (OPA). A preliminary analysis clearly showed that a rough adaption of the theoretical scheme typically explored in literature (OPA+phase modulator+OPA) does not allow to achieve an appropriate degree of visibility in the interference pattern. This is due to the presence of dispersion inside the interferometer, which needs to be attenuated in order to maximize the visibility. Therefore, in the proposed design of the SU(1,1) interferometer, we were able to strongly attenuated the dispersion, and therefore drastically enhanced the visibility. As a consequence of that, the interferometer could work in a supersensitivity regime. Moreover, we were able to improve the performance of the device by the employment of designed filters.

Finally, although the spectral features of the interferometer enable the exploration of a large spectra of seeding strategies, our current results clearly showed that we can achieve the best performance of the interferometer with vacuum seed. However, the seeds we used were localized in only one arm of the interferometer. This inevitably leads to the reduction of correlations between the two channels of the interferometer and consequently a worsening of the phase sensitivity. Hence, we do not exclude that the performance of the interferometer could be improved with different seeding strategies, holding the correlation between the two photons. This can be done by seeding both arms of the interferometer opportunely.

In the end, we can state that in all cases explored in this thesis we were able to manipulate the interference pattern and, more generally, the performance of the interferometer by an accurate spectral investigation of the photon source. In particular, in our analysis it emerged that the simultaneous work of both controlling the photon correlations via a punctual state engineering, along with a proper implementation of the design of the interferometer, allows to implement more accurate theoretical models for describing a large selection of interference scenarios. Therefore, the results contained in this thesis demonstrated that the inclusion of a spectral analysis of the photon state, and hence of the photon source, surely provides interesting perspectives and opens new frontiers in quantum interferometry, integrated photonics and quantum metrology.

Appendix A

Experimental set-up: Four photon interference

In this Appendix we want to present the experiment scheme used to get the photon counts in Fig.(3.4) and Fig.(3.6), namely for both balanced and unbalanced configuration of BS.

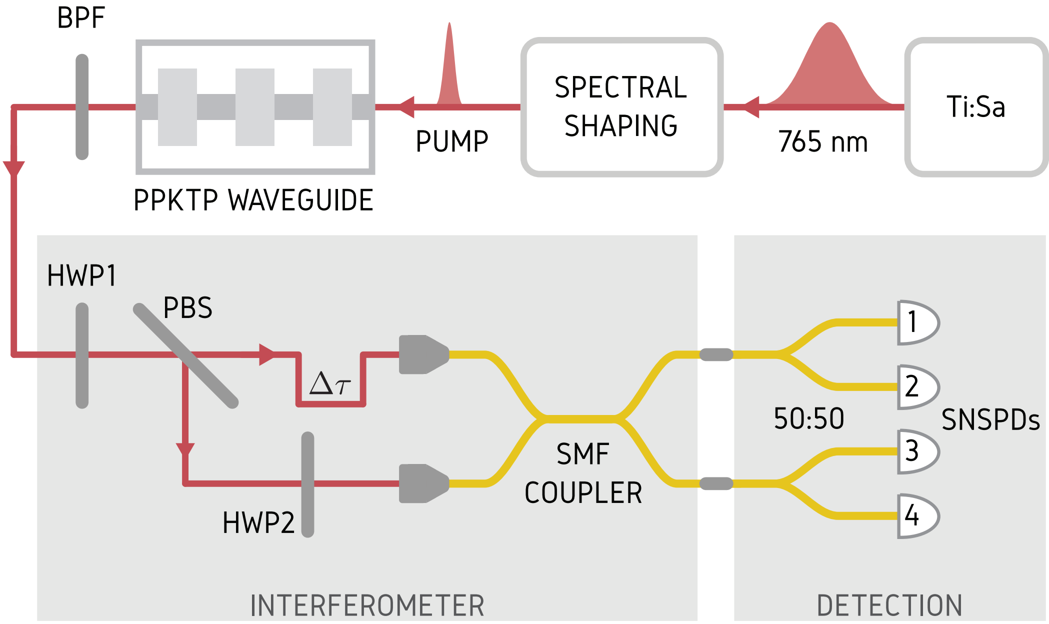

Figure A.1: Experimental setup. A femtosecond titanium:sapphire (Ti:Sa) oscillator with repetition rate of 80 MHz is used to pump a PPKTP waveguide designed for type-II PDC. For spectral shaping of the pump, we use a spatial light modulator (SLM) in a folded 4f setup to shape the desired spectral amplitude and phase. An 8 nm wide bandpass filter (BPF) centred at 1532 nm was used to block the pump and phasematching side-lobes. The orthogonally polarized PDC photons were sent to the interferometer setup where we used a polarising beamsplitter (PBS), a half waveplate (HWP), and an adjustable time delay stage $\Delta\tau$ to control the interference. Then the photons were sent to a single-mode fibre coupler with an adjustable coupling ratio where interference happens. Each output port of the fibre coupler is then connected to a balanced fibre splitter followed by superconducting nanowire single photon detectors (SNSPD).

Such scheme is sketched in Fig.A.1 in details [1]. In order to investigate the impact of time-frequency correlations of the state on the four-photon interference, an engineered, programmable PDC source was employed. The source is a ppKTP waveguide having length $8mm$, engineered to the symmetric group velocity matching condition which allows us to flexibly control the frequency correlation between signal and idler photons by modulating the pump pulses only [45,121]. The source consists of a Ti:Sa oscillator emitting ultrashort pulses, tuned in terms of amplitude and phase by a pulse shaper based on a spatial light modulator in a 4f setup. Pulses generated by this configuration are characterized by bandwidths range from 0.3 to 40 ps.

Lastly, the choice of the pump power had to be functional to the theoretical model. For instance, in order to partially inhibit the generation of higher order photon numbers and eventual time ordering effects, a low pump energy, around 6.5 pJ, was used to generate an amount of down-converted photon approximately equal 0.02 per pulse. Such configuration allows to make the second order PDC effect (four photon generation) about 50 times more effective than the third order (six photons generation).

The experimental parameters used to define states A, B and C are listed in Table.A.1.

	State A	State B	State C
	pump field amplitude setting		
$\Delta\lambda_{\text{pump}}$ (nm)	1.8	0.2	1.8
$\Delta\omega_{\text{pump}}$ (THz)	3.479	0.386	3.44
D (ps^2)	0	0	1.9
Δt_{pump} (ps)	0.14	1.29	6.62
	correlation function and Schmidt number		
$g^{(2)}(\tau = 0)$	1.897 ± 0.011	1.233 ± 0.010	1.108 ± 0.003
$K = \frac{1}{g^{(2)}-1}$	1.11	4.29	9.25
	$P_{1,1}$ interference		
$V_{\text{th.}}$ (%)	92.7	100.0	92.7
$V_{\text{exp.}}$ (%)	90.7±0.5	92.7±0.7	90.2±0.8
$\Delta L_{\text{th.}}$ (mm)	0.368	0.341	0.368
$\Delta L_{\text{exp.}}$ (mm)	0.381±0.003	0.358±0.004	0.373±0.005

Table A.1: Overview of studied PDC states. Δ denotes the standard deviation; V denotes the visibility and ΔL denotes the standard deviation of $P_{1,1}$ interference, calculated with a Gaussian fit function to the theory and experiment.

Appendix B

Experimental set-up: spatial entanglement generation

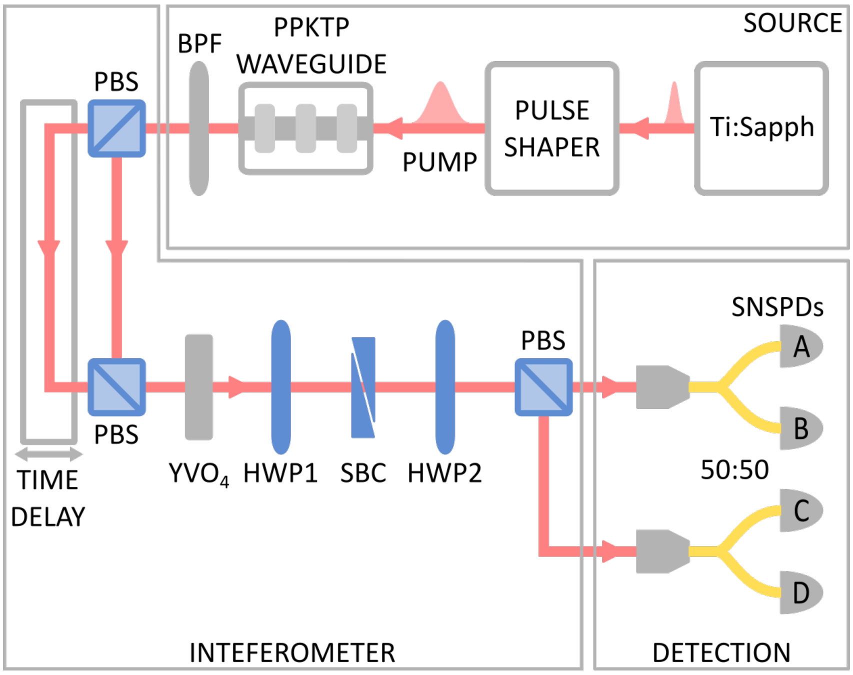

Figure B.1: Experimental setup. A femtosecond titanium:sapphire (Ti:Sapph) oscillator with repetition rate of 80 MHz is used to pump a PPKTP waveguide designed for type-II PDC. We use a pulse shaper to set the desired spectral amplitude and phase of the pump pulses. An 8 nm wide bandpass filter (BPF) centered at 1532 nm was used to block the pump and phasematching side-lobes. The signal and idler photon coarse time delay is set with a linear translation stage. A 1.5 mm long YVO_4 crystal is used to compensate for the time delay between signal and idler photons, when the translation stage is set to zero delay. We use a common-path setup to interfere PDC photons where we scan the time delay using a soleil-babinet compensator (SBC). This is followed by half-wave plates HWP_1 and HWP_2, which are set to 22.5°, and a polarizing beamsplitter (PBS). This interferometer is equivalent to the setup shown in Fig. 3.8. Photons are then coupled to balanced single-mode fiber splitters followed by four superconducting nanowire single photon detectors (SNSPD).

In order to accurately scan the probability P_{22} in Fig. 3.11 two different but equivalent experimental set-up were required. Due to the evident similarities between the two schemes in Fig. 3.1 and Fig. 3.8, the first apparatus is already described in Appendix A, where the first HWP is here switched on, and the conversion parameter is fixed to $\phi_1 = \pi/4$. Such set-up allows to measure the coincidence probability also for large path delay, with width about 20 mm, but it does not provide useful information when $\Delta l \approx 0$.

The presence of a further element (a second HWP) as well as the higher precision required to scan the fast fringes in the interference pattern, force us to use an additional and more stable apparatus, illustrated and fully described in Fig. B.1; however, despite the evident structural differences, it can be demonstrated that such new apparatus is fully equivalent to Fig. 3.8. The presence of a soleil-babinet compensator ensures a major stability and a better performance in phasing for small range around $\Delta = 0$. Such experimental scheme was hence used to scan the fast fringes in the insert of Fig. 3.11, and can be utilized to test also the interference pattern in Fig. 3.14.

Acknowledgements

If I had the chance to have a conversation with that long-haired guy getting his Master in Physics, who was me, five years ago, I would not have few problems convincing him that he is going to pursue the doctoral degree in Germany, having the opportunity to travel and knowing literally hundreds of people from the whole world. Probably it would be easier for him to believe that the entire world will face a pandemic shattering all aspects of mankind. Ok, probably I would not mention it.

In any cases, I definitely would explain him that all these important experiences were possible thanks to the crucial support of many people during these years of PhD.

That is why, first of all, I want to thank my supervisor Polina. She was the person who believed in me, giving the opportunity to start my career as researcher. She is a very kind and patient person. I cannot even count how many times I annoyed her for any clarifications, debates and explanations. Her constant presence was fundamental in all aspects of my research.

Along with Polina, I want to thank both Prof. Christine Silberhorn and Prof. Torsten Meier for their contributions to my professional education. Fortunately, I had the opportunity to take advantages of their deep experience in both experimental and theoretical aspects of quantum optics. Besides, all meetings I had with their work groups were definitely formative. I want to thank my historical office mate Wolf, with whom I had interesting conversation, as well as the other people from the corridor, in particular Agnieszka, Daniel and Matthias.

The academic environment enables new connections beyond the working goals. About that, a special thanks is for Simone. Her empathy and availability were an enormous help inside (and also outside) the university. I would like to thank my Russian college Matvei in Russian, but since he does not like my pronunciation, so I will do it in English.

There is a common belief claiming that Italians are everywhere all over the world. In this case, it was a luck for me to meet my old university college Marcello, and know Matteo, whose professional and empathic support was of critical importance, especially in the last part of my PhD experience.

Now it is time to take a look beyond the university campus.

Surely, the first person I have to thank is F. Christine. She was essentially my German sister, and I really do not know how I could have managed this time in Paderborn without her psychological and pragmatic help. Moreover, if I was able to overcome the linguistic barrier and learn German, it was thanks to her.

The second person I want to thank is Andrea, the Italian whom I spent most of my recent time with. I am quite confident of believing that we were the only guys in the whole NRW spending evenings in an Irish pubs talking about mathematics, history, philosophy

and Italian memes.

Beyond the German borders, I want to thank people who were virtually and sometimes also physically close to me.

I want to thank Anna for being daily present. Fortunately, the technology of last century could reduce our distance, at least spiritually. We shared a lot in the last part of my PhD and her presence became crucial.

Now it is time to mention my historical friends from Sicily, Antongiacomo and Giovanni B. I hope we will have the opportunity to spend time together in the future as we did in the last fifteen years.

Thanks to my old friends from the university: the nerdy "dwarf" Simona (for external readers: this is only a devoted way to call her); my greatest fan (I know you are...) Nicola, and Angela, the only brave friend visiting me in Paderborn.

I had the pleasure to have many other friends supporting me from my home land. For instance, I want to mention Virginia, Giovanni I., Genny, Viviana and Francesco, whom I know from so many years.

Last but not least I want to thank my family. I am quite sure that the best present I can give them is making them proud of me and my accomplishments.

Bibliography

[1] A. Ferreri, V. Ansari, C. Silberhorn, and P. R. Sharapova, “Temporally multimode four-photon hong-ou-mandel interference,” *Physical Review A*, vol. 100, p. 053829, Nov 2019.

[2] A. Ferreri, V. Ansari, B. Brecht, C. Silberhorn, and P. R. Sharapova, “Spatial entanglement and state engineering via four-photon hong–ou–mandel interference,” *Quantum Science and Technology*, vol. 5, p. 045020, sep 2020.

[3] A. Ferreri, M. Santandrea, M. Stefszky, K. H. Luo, H. Herrmann, C. Silberhorn, and P. R. Sharapova, “Spectrally multimode integrated su (1, 1) interferometer,” *arXiv preprint arXiv:2012.03751*, 2020.

[4] S. Haroche, J. Raimond, and O. U. Press, *Exploring the Quantum: Atoms, Cavities, and Photons*. Oxford Graduate Texts, OUP Oxford, 2006.

[5] C.-K. Hong, Z.-Y. Ou, and L. Mandel, “Measurement of subpicosecond time intervals between two photons by interference,” *Physical Review Letters*, vol. 59, no. 18, p. 2044, 1987.

[6] J.-W. Pan, Z.-B. Chen, C.-Y. Lu, H. Weinfurter, A. Zeilinger, and M. Żukowski, “Multiphoton entanglement and interferometry,” *Reviews of Modern Physics*, vol. 84, pp. 777–838, May 2012.

[7] P. Bertet, S. Osnaghi, A. Rauschenbeutel, G. Nogues, A. Auffeves, M. Brune, J. Raimond, and S. Haroche, “A complementarity experiment with an interferometer at the quantum–classical boundary,” *Nature*, vol. 411, no. 6834, pp. 166–170, 2001.

[8] J. P. Dowling, “Quantum optical metrology - the lowdown on high-n00n states,” *Contemporary Physics*, vol. 49, no. 2, pp. 125–143, 2008.

[9] T. Kim, O. Pfister, M. J. Holland, J. Noh, and J. L. Hall, “Influence of decorrelation on heisenberg-limited interferometry with quantum correlated photons,” *Physical Review A*, vol. 57, pp. 4004–4013, May 1998.

[10] I. Ruo Berchera, I. P. Degiovanni, S. Olivares, and M. Genovese, “Quantum light in coupled interferometers for quantum gravity tests,” *Physical Review Letters*, vol. 110, p. 213601, May 2013.

[11] C. Couteau, “Spontaneous parametric down-conversion,” *Contemporary Physics*, vol. 59, no. 3, pp. 291–304, 2018.

[12] S. Carrasco, A. V. Sergienko, B. E. A. Saleh, M. C. Teich, J. P. Torres, and L. Torner, "Spectral engineering of entangled two-photon states," *Physical Review A*, vol. 73, p. 063802, Jun 2006.

[13] A. V. Sergienko, M. Atatüre, Z. Walton, G. Jaeger, B. E. A. Saleh, and M. C. Teich, "Quantum cryptography using femtosecond-pulsed parametric down-conversion," *Physical Review A*, vol. 60, pp. R2622–R2625, Oct 1999.

[14] Y. Luo and K. T. Chan, "Quantum cryptography with entangled multiphotons of the same polarization," *Physical Review A*, vol. 70, p. 042302, Oct 2004.

[15] A. S. Solntsev, A. A. Sukhorukov, D. N. Neshev, and Y. S. Kivshar, "Spontaneous parametric down-conversion and quantum walks in arrays of quadratic nonlinear waveguides," *Physical Review Letters*, vol. 108, p. 023601, Jan 2012.

[16] H. Defienne, M. Barbieri, I. A. Walmsley, B. J. Smith, and S. Gigan, "Two-photon quantum walk in a multimode fiber," *Science Advances*, vol. 2, no. 1, 2016.

[17] R. Ghosh, C. K. Hong, Z. Y. Ou, and L. Mandel, "Interference of two photons in parametric down conversion," *Physical Review A*, vol. 34, pp. 3962–3968, Nov 1986.

[18] Y. H. Shih, A. V. Sergienko, M. H. Rubin, T. E. Kiess, and C. O. Alley, "Two-photon entanglement in type-ii parametric down-conversion," *Physical Review A*, vol. 50, pp. 23–28, Jul 1994.

[19] M. H. Rubin, D. N. Klyshko, Y. H. Shih, and A. V. Sergienko, "Theory of two-photon entanglement in type-ii optical parametric down-conversion," *Physical Review A*, vol. 50, pp. 5122–5133, Dec 1994.

[20] T. E. Keller and M. H. Rubin, "Theory of two-photon entanglement for spontaneous parametric down-conversion driven by a narrow pump pulse," *Physical Review A*, vol. 56, pp. 1534–1541, Aug 1997.

[21] S. Walborn, C. Monken, S. PÃ¡dua, and P. Souto Ribeiro, "Spatial correlations in parametric down-conversion," *Physics Reports*, vol. 495, no. 4, pp. 87 – 139, 2010.

[22] M. H. Rubin, "Transverse correlation in optical spontaneous parametric down-conversion," *Physical Review A*, vol. 54, pp. 5349–5360, Dec 1996.

[23] L.-A. Wu, H. J. Kimble, J. L. Hall, and H. Wu, "Generation of squeezed states by parametric down conversion," *Physical Review Letters*, vol. 57, pp. 2520–2523, Nov 1986.

[24] J. D. Jackson, *Classical electrodynamics*. Wiley, 1999.

[25] K. J. Blow, R. Loudon, S. J. D. Phoenix, and T. J. Shepherd, "Continuum fields in quantum optics," *Physical Review A*, vol. 42, pp. 4102–4114, Oct 1990.

[26] E. M. Purcell, *Spontaneous Emission Probabilities at Radio Frequencies*, pp. 839–839. Boston, MA: Springer US, 1995.

[27] A. Ferreri, M. Domina, L. Rizzuto, and R. Passante, “Spontaneous emission of an atom near an oscillating mirror,” *Symmetry*, vol. 11, no. 11, 2019.

[28] M. Chaichian, M. M. Sheikh-Jabbari, and A. Tureanu, “Hydrogen atom spectrum and the lamb shift in noncommutative qed,” *Physical Review Letters*, vol. 86, pp. 2716–2719, Mar 2001.

[29] W. Johnson and G. Soff, “The lamb shift in hydrogen-like atoms $1 \leq z \leq 110$,” *Atomic Data and Nuclear Data Tables*, vol. 33, no. 3, pp. 405 – 446, 1985.

[30] H. B. Casimir, “On the attraction between two perfectly conducting plates,” *Front. Phys.*, vol. 100, pp. 61–63, 1948.

[31] J. Schwinger, L. L. DeRaad, and K. A. Milton, “Casimir effect in dielectrics,” *Annals of Physics*, vol. 115, no. 1, pp. 1 – 23, 1978.

[32] P. Kumar, “Quantum frequency conversion,” *Optics Letters*, vol. 15, pp. 1476–1478, Dec 1990.

[33] A. Christ, B. Brecht, W. Mauerer, and C. Silberhorn, “Theory of quantum frequency conversion and type-II parametric down-conversion in the high-gain regime,” *New Journal of Physics*, vol. 15, p. 053038, may 2013.

[34] W. H. Louisell, A. Yariv, and A. E. Siegman, “Quantum fluctuations and noise in parametric processes. i.,” *Physical Review*, vol. 124, pp. 1646–1654, Dec 1961.

[35] B. R. Mollow, “Photon correlations in the parametric frequency splitting of light,” *Physical Review A*, vol. 8, pp. 2684–2694, Nov 1973.

[36] R. E. Slusher, L. W. Hollberg, B. Yurke, J. C. Mertz, and J. F. Valley, “Observation of squeezed states generated by four-wave mixing in an optical cavity,” *Physical Review Letters*, vol. 55, pp. 2409–2412, Nov 1985.

[37] R. Loudon, *The quantum theory of light.* OUP Oxford, 2000.

[38] J. J. Sakurai, *Modern Quantum Mechanics.* Revised edition, August 1993.

[39] N. Quesada and J. E. Sipe, “Effects of time ordering in quantum nonlinear optics,” *Physical Review A*, vol. 90, p. 063840, Dec 2014.

[40] J. A. Armstrong, N. Bloembergen, J. Ducuing, and P. S. Pershan, “Interactions between light waves in a nonlinear dielectric,” *Physical Review*, vol. 127, pp. 1918–1939, Sep 1962.

[41] M. M. Fejer, G. A. Magel, D. H. Jundt, and R. L. Byer, “Quasi-phase-matched second harmonic generation: tuning and tolerances,” *IEEE Journal of Quantum Electronics*, vol. 28, pp. 2631–2654, Nov 1992.

[42] M. Santandrea, M. Stefszky, V. Ansari, and C. Silberhorn, “Fabrication limits of waveguides in nonlinear crystals and their impact on quantum optics applications,” *New Journal of Physics*, vol. 21, p. 033038, mar 2019.

[43] G. A. Magel, M. M. Fejer, and R. L. Byer, "Quasi-phase-matched second-harmonic generation of blue light in periodically poled linbo3," *Applied Physics Letters*, vol. 56, no. 2, pp. 108–110, 1990.

[44] M. Fiorentino, S. M. Spillane, R. G. Beausoleil, T. D. Roberts, P. Battle, and M. W. Munro, "Spontaneous parametric down-conversion in periodically poled ktp waveguides and bulk crystals," *Optics Express*, vol. 15, pp. 7479–7488, Jun 2007.

[45] G. Harder, V. Ansari, B. Brecht, T. Dirmeier, C. Marquardt, and C. Silberhorn, "An optimized photon pair source for quantum circuits," *Optics Express*, vol. 21, no. 12, pp. 13975–13985, 2013.

[46] C. K. Law, I. A. Walmsley, and J. H. Eberly, "Continuous frequency entanglement: Effective finite hilbert space and entropy control," *Physical Review Letters*, vol. 84, pp. 5304–5307, Jun 2000.

[47] P. P. Rohde, W. Mauerer, and C. Silberhorn, "Spectral structure and decompositions of optical states, and their applications," *New Journal of Physics*, vol. 9, pp. 91–91, apr 2007.

[48] V. Ansari, J. M. Donohue, B. Brecht, and C. Silberhorn, "Tailoring nonlinear processes for quantum optics with pulsed temporal-mode encodings," *Optica*, vol. 5, pp. 534–550, May 2018.

[49] V. Ansari, J. M. Donohue, M. Allgaier, L. Sansoni, B. Brecht, J. Roslund, N. Treps, G. Harder, and C. Silberhorn, "Tomography and purification of the temporal-mode structure of quantum light," *Physical Review Letters*, vol. 120, p. 213601, May 2018.

[50] V. Ansari, G. Harder, M. Allgaier, B. Brecht, and C. Silberhorn, "Temporal-mode measurement tomography of a quantum pulse gate," *Physical Review A*, vol. 96, p. 063817, Dec 2017.

[51] B. Brecht, D. V. Reddy, C. Silberhorn, and M. G. Raymer, "Photon temporal modes: A complete framework for quantum information science," *Physical Review X*, vol. 5, p. 041017, Oct 2015.

[52] P. Sharapova, A. M. Pérez, O. V. Tikhonova, and M. V. Chekhova, "Schmidt modes in the angular spectrum of bright squeezed vacuum," *Physical Review A*, vol. 91, p. 043816, Apr 2015.

[53] B. Yurke, S. L. McCall, and J. R. Klauder, "Su(2) and su(1,1) interferometers," *Physical Review A*, vol. 33, pp. 4033–4054, Jun 1986.

[54] R. A. Campos, B. E. A. Saleh, and M. C. Teich, "Quantum-mechanical lossless beam splitter: Su(2) symmetry and photon statistics," *Physical Review A*, vol. 40, pp. 1371–1384, Aug 1989.

[55] M. V. Chekhova and Z. Y. Ou, "Nonlinear interferometers in quantum optics," *Advances in Optics and Photonics*, vol. 8, pp. 104–155, Mar 2016.

[56] P. R. Sharapova, K. H. Luo, H. Herrmann, M. Reichelt, C. Silberhorn, and T. Meier, "Modified two-photon interference achieved by the manipulation of entanglement," *Physical Review A*, vol. 96, p. 043857, Oct 2017.

[57] M. A. Nielsen and I. Chuang, "Quantum computation and quantum information," 2002.

[58] G. Harder, V. Ansari, B. Brecht, T. Dirmeier, C. Marquardt, and C. Silberhorn, "An optimized photon pair source for quantum circuits," *Optics Express*, vol. 21, pp. 13975–13985, Jun 2013.

[59] P. Sharapova, K. Luo, H. Herrmann, M. Reichelt, T. Meier, and C. Silberhorn, "Toolbox for the design of linbo3-based passive and active integrated quantum circuits," *New Journal of Physics*, vol. 19, no. 12, p. 123009, 2017.

[60] C. Lang, C. Eichler, L. Steffen, J. Fink, M. Woolley, A. Blais, and A. Wallraff, "Correlations, indistinguishability and entanglement in hong–ou–mandel experiments at microwave frequencies," *Nature Physics*, vol. 9, no. 6, pp. 345–348, 2013.

[61] C. Sparaciari, S. Olivares, and M. G. A. Paris, "Gaussian-state interferometry with passive and active elements," *Physical Review A*, vol. 93, p. 023810, Feb 2016.

[62] C. M. Caves, "Quantum-mechanical noise in an interferometer," *Physical Review D*, vol. 23, pp. 1693–1708, Apr 1981.

[63] C. M. Caves, "Quantum limits on noise in linear amplifiers," *Physical Review D*, vol. 26, pp. 1817–1839, Oct 1982.

[64] M. J. Holland and K. Burnett, "Interferometric detection of optical phase shifts at the heisenberg limit," *Physical Review Letters*, vol. 71, pp. 1355–1358, Aug 1993.

[65] Z. Y. Ou, "Fundamental quantum limit in precision phase measurement," *Physical Review A*, vol. 55, pp. 2598–2609, Apr 1997.

[66] B. E. Anderson, B. L. Schmittberger, P. Gupta, K. M. Jones, and P. D. Lett, "Optimal phase measurements with bright- and vacuum-seeded su(1,1) interferometers," *Physical Review A*, vol. 95, p. 063843, Jun 2017.

[67] R. Demkowicz-Dobrzański, M. Jarzyna, and J. Kołodyński, "Chapter four - quantum limits in optical interferometry," vol. 60 of *Progress in Optics*, pp. 345 – 435, Elsevier, 2015.

[68] M. O. Scully and M. S. Zubairy, "Quantum optics," *American Journal of Physics*, vol. 67, no. 7, pp. 648–648, 1999.

[69] T. Lipfert, J. Sperling, and W. Vogel, "Homodyne detection with on-off detector systems," *Physical Review A*, vol. 92, p. 053835, Nov 2015.

[70] T. Hirano, H. Yamanaka, M. Ashikaga, T. Konishi, and R. Namiki, "Quantum cryptography using pulsed homodyne detection," *Physical Review A*, vol. 68, p. 042331, Oct 2003.

[71] M. Manceau, F. Khalili, and M. Chekhova, “Improving the phase super-sensitivity of squeezing-assisted interferometers by squeeze factor unbalancing,” *New Journal of Physics*, vol. 19, no. 1, p. 013014, 2017.

[72] M. Xiao, L.-A. Wu, and H. J. Kimble, “Precision measurement beyond the shot-noise limit,” *Physical Review Letters*, vol. 59, pp. 278–281, Jul 1987.

[73] P. Grangier, R. E. Slusher, B. Yurke, and A. LaPorta, “Squeezed-light–enhanced polarization interferometer,” *Physical Review Letters*, vol. 59, pp. 2153–2156, Nov 1987.

[74] J. Kong, Z. Y. Ou, and W. Zhang, “Phase-measurement sensitivity beyond the standard quantum limit in an interferometer consisting of a parametric amplifier and a beam splitter,” *Physical Review A*, vol. 87, p. 023825, Feb 2013.

[75] R. Demkowicz-Dobrzański, J. Kołodyński, and M. Guţă, “The elusive heisenberg limit in quantum-enhanced metrology,” *Nature communications*, vol. 3, no. 1, pp. 1–8, 2012.

[76] H. Lee, P. Kok, and J. P. Dowling, “A quantum rosetta stone for interferometry,” *Journal of Modern Optics*, vol. 49, no. 14-15, pp. 2325–2338, 2002.

[77] S. Slussarenko, M. M. Weston, H. M. Chrzanowski, L. K. Shalm, V. B. Verma, S. W. Nam, and G. J. Pryde, “Unconditional violation of the shot-noise limit in photonic quantum metrology,” *Nature Photonics*, vol. 11, no. 11, p. 700, 2017.

[78] W. N. Plick, J. P. Dowling, and G. S. Agarwal, “Coherent-light-boosted, sub-shot noise, quantum interferometry,” *New Journal of Physics*, vol. 12, p. 083014, aug 2010.

[79] S. Lemieux, M. Manceau, P. R. Sharapova, O. V. Tikhonova, R. W. Boyd, G. Leuchs, and M. V. Chekhova, “Engineering the frequency spectrum of bright squeezed vacuum via group velocity dispersion in an su(1,1) interferometer,” *Physical Review Letters*, vol. 117, p. 183601, Oct 2016.

[80] D. Li, C.-H. Yuan, Y. Yao, W. Jiang, M. Li, and W. Zhang, “Effects of loss on the phase sensitivity with parity detection in an su(1,1) interferometer,” *Journal of the Optical Society of America B*, vol. 35, pp. 1080–1092, May 2018.

[81] A. M. Marino, N. V. Corzo Trejo, and P. D. Lett, “Effect of losses on the performance of an su(1,1) interferometer,” *Physical Review A*, vol. 86, p. 023844, Aug 2012.

[82] K. Mattle, H. Weinfurter, P. G. Kwiat, and A. Zeilinger, “Dense coding in experimental quantum communication,” *Physical Review Letters*, vol. 76, no. 25, p. 4656, 1996.

[83] J. R. Torgerson, D. Branning, C. H. Monken, and L. Mandel, “Experimental demonstration of the violation of local realism without bell inequalities,” *Physics Letters A*, vol. 204, no. 5-6, pp. 323–328, 1995.

[84] E. M. Nagasako, S. J. Bentley, R. W. Boyd, and G. S. Agarwal, “Nonclassical two-photon interferometry and lithography with high-gain parametric amplifiers,” *Physical Review A*, vol. 64, no. 4, p. 043802, 2001.

[85] A. N. Boto, P. Kok, D. S. Abrams, S. L. Braunstein, C. P. Williams, and J. P. Dowling, “Quantum interferometric optical lithography: exploiting entanglement to beat the diffraction limit,” *Physical Review Letters*, vol. 85, no. 13, p. 2733, 2000.

[86] M. C. Tichy, M. Tiersch, F. Mintert, and A. Buchleitner, “Many-particle interference beyond many-boson and many-fermion statistics,” *New Journal of Physics*, vol. 14, no. 9, p. 093015, 2012.

[87] Z. Y. Ou, J.-K. Rhee, and L. J. Wang, “Photon bunching and multiphoton interference in parametric down-conversion,” *Physical Review A*, vol. 60, pp. 593–604, Jul 1999.

[88] A. F. Abouraddy, T. M. Yarnall, and G. Di Giuseppe, “Phase-unlocked hong-ou-mandel interferometry,” *Physical Review A*, vol. 87, p. 062106, Jun 2013.

[89] Z. Y. Ou, J.-K. Rhee, and L. J. Wang, “Observation of four-photon interference with a beam splitter by pulsed parametric down-conversion,” *Physical Review Letters*, vol. 83, pp. 959–962, Aug 1999.

[90] S. Agne, T. Kauten, J. Jin, E. Meyer-Scott, J. Z. Salvail, D. R. Hamel, K. J. Resch, G. Weihs, and T. Jennewein, “Observation of genuine three-photon interference,” *Physical Review Letters*, vol. 118, p. 153602, Apr 2017.

[91] T. Giordani, F. Flamini, M. Pompili, N. Viggianiello, N. Spagnolo, A. Crespi, R. Osellame, N. Wiebe, M. Walschaers, A. Buchleitner, *et al.*, “Experimental statistical signature of many-body quantum interference,” *Nature Photonics*, vol. 12, no. 3, p. 173, 2018.

[92] M. Tillmann, S.-H. Tan, S. E. Stoeckl, B. C. Sanders, H. de Guise, R. Heilmann, S. Nolte, A. Szameit, and P. Walther, “Generalized multiphoton quantum interference,” *Physical Review X*, vol. 5, p. 041015, Oct 2015.

[93] M. Bentivegna, N. Spagnolo, C. Vitelli, F. Flamini, N. Viggianiello, L. Latmiral, P. Mataloni, D. J. Brod, E. F. Galvão, A. Crespi, *et al.*, “Experimental scattershot boson sampling,” *Science Advances*, vol. 1, no. 3, p. e1400255, 2015.

[94] H. Wang, Y. He, Y. Li, Z. Su, B. Li, H. Huang, X. Ding, M. Chen, C. Liu, J. Qin, J. Li, Y. He, C. Schneider, M. Kamp, C. Peng, S. Hoefling, C. Lu, and J. Pan, “High-efficiency multiphoton boson sampling,” *Nature Photonics*, vol. 11, pp. 361–365, 2017.

[95] Y. Shen, N. C. Harris, S. Skirlo, M. Prabhu, T. Baehr-Jones, M. Hochberg, X. Sun, S. Zhao, H. Larochelle, D. Englund, *et al.*, “Deep learning with coherent nanophotonic circuits,” *Nature Photonics*, vol. 11, no. 7, p. 441, 2017.

[96] T. W. Hughes, M. Minkov, Y. Shi, and S. Fan, “Training of photonic neural networks through in situ backpropagation and gradient measurement,” *Optica*, vol. 5, no. 7, pp. 864–871, 2018.

[97] A. N. Tait, T. F. de Lima, E. Zhou, A. X. Wu, M. A. Nahmias, B. J. Shastri, and P. R. Prucnal, “Neuromorphic photonic networks using silicon photonic weight banks,” *Scientific reports*, vol. 7, no. 1, p. 7430, 2017.

[98] F. Flamini, N. Spagnolo, and F. Sciarrino, “Visual assessment of multi-photon interference,” *Quantum Science and Technology*, vol. 4, p. 024008, mar 2019.

[99] Y.-S. Ra, M. C. Tichy, H.-T. Lim, O. Kwon, F. Mintert, A. Buchleitner, and Y.-H. Kim, “Nonmonotonic quantum-to-classical transition in multiparticle interference,” *Proceedings of the National Academy of Sciences*, vol. 110, no. 4, pp. 1227–1231, 2013.

[100] O. Cosme, S. Pádua, F. A. Bovino, A. Mazzei, F. Sciarrino, and F. De Martini, “Hong-ou-mandel interferometer with one and two photon pairs,” *Physical Review A*, vol. 77, p. 053822, May 2008.

[101] A. J. Menssen, A. E. Jones, B. J. Metcalf, M. C. Tichy, S. Barz, W. S. Kolthammer, and I. A. Walmsley, “Distinguishability and many-particle interference,” *Physical Review Letters*, vol. 118, p. 153603, Apr 2017.

[102] Z. Ou, “Distinguishing four photons in an entangled state from two independent pairs of photons,” *Physical Review A*, vol. 72, no. 5, p. 053814, 2005.

[103] P. Walther, J.-W. Pan, M. Aspelmeyer, R. Ursin, S. Gasparoni, and A. Zeilinger, “De broglie wavelength of a non-local four-photon state,” *Nature*, vol. 429, no. 6988, p. 158, 2004.

[104] B. A. Bell, G. S. Thekkadath, R. Ge, X. Cai, and I. A. Walmsley, “Testing multiphoton interference on a silicon chip,” *Opt. Express*, vol. 27, pp. 35646–35658, Nov 2019.

[105] B. J. Metcalf, N. Thomas-Peter, J. B. Spring, D. Kundys, M. A. Broome, P. C. Humphreys, X.-M. Jin, M. Barbieri, W. S. Kolthammer, J. C. Gates, *et al.*, “Multiphoton quantum interference in a multiport integrated photonic device,” *Nature Communications*, vol. 4, no. 1, pp. 1–7, 2013.

[106] X. Zou and W. Mathis, “Generating a four-photon polarization-entangled cluster state,” *Physical Review A*, vol. 71, p. 032308, Mar 2005.

[107] D. Bouwmeester, J.-W. Pan, M. Daniell, H. Weinfurter, and A. Zeilinger, “Observation of three-photon greenberger-horne-zeilinger entanglement,” *Physical Review Letters*, vol. 82, no. 7, p. 1345, 1999.

[108] J.-W. Pan, D. Bouwmeester, M. Daniell, H. Weinfurter, and A. Zeilinger, “Experimental test of quantum nonlocality in three-photon greenberger–horne–zeilinger entanglement,” *Nature*, vol. 403, no. 6769, p. 515, 2000.

[109] M. Hillery, V. Bužek, and A. Berthiaume, "Quantum secret sharing," *Physical Review A*, vol. 59, no. 3, p. 1829, 1999.

[110] I. Afek, O. Ambar, and Y. Silberberg, "High-noon states by mixing quantum and classical light," *Science*, vol. 328, no. 5980, pp. 879–881, 2010.

[111] T. Nagata, R. Okamoto, J. L. O'brien, K. Sasaki, and S. Takeuchi, "Beating the standard quantum limit with four-entangled photons," *Science*, vol. 316, no. 5825, pp. 726–729, 2007.

[112] B. T. Gard, R. M. Cross, P. M. Anisimov, H. Lee, and J. P. Dowling, "Quantum random walks with multiphoton interference and high-order correlation functions," *Journal of the Optical Society of America B*, vol. 30, pp. 1538–1545, Jun 2013.

[113] M. Yabuno, R. Shimizu, Y. Mitsumori, H. Kosaka, and K. Edamatsu, "Four-photon quantum interferometry at a telecom wavelength," *Physical Review A*, vol. 86, p. 010302, Jul 2012.

[114] G. Jaeger, "Bell gems: the bell basis generalized," *Physics Letters A*, vol. 329, no. 6, pp. 425 – 429, 2004.

[115] G. Jaeger and A. Sergienko, "Constructing four-photon states for quantum communication and information processing," *International Journal of Theoretical Physics*, vol. 47, pp. 2120–2125, Aug 2008.

[116] B. A. Bell and B. J. Eggleton, "Multiphoton interference in the spectral domain by direct heralding of frequency superposition states," *Physical Review Letter*, vol. 121, p. 033601, Jul 2018.

[117] N. Quesada and J. E. Sipe, "Time-ordering effects in the generation of entangled photons using nonlinear optical processes," *Physical Review Letters*, vol. 114, p. 093903, Mar 2015.

[118] V. Ansari, B. Brecht, G. Harder, and C. Silberhorn, "Probing spectral-temporal correlations with a versatile integrated source of parametric down-conversion states," *arXiv preprint arXiv:1404.7725*, 2014.

[119] H. D. Riedmatten, V. Scarani, I. Marcikic, A. Acín, W. Tittel, H. Zbinden, and N. Gisin, "Two independent photon pairs versus four-photon entangled states in parametric down conversion," *Journal of Modern Optics*, vol. 51, no. 11, pp. 1637–1649, 2004.

[120] B.-S. Shi and A. Tomita, "Four photons interfering but showing the two-photon interference behaviour," *Journal of Modern Optics*, vol. 53, no. 7, pp. 1003–1009, 2006.

[121] V. Ansari, J. M. Donohue, B. Brecht, and C. Silberhorn, "Tailoring nonlinear processes for quantum optics with pulsed temporal-mode encodings," *Optica*, vol. 5, no. 5, pp. 534–550, 2018.

[122] B. Liu, F. Sun, Y. Gong, Y. Huang, G. Guo, and Z. Ou, “Four-photon interference with asymmetric beam splitters,” *Optics Letters*, vol. 32, no. 10, pp. 1320–1322, 2007.

[123] D. Li, C.-H. Yuan, Z. Y. Ou, and W. Zhang, “The phase sensitivity of an SU(1,1) interferometer with coherent and squeezed-vacuum light,” *New Journal of Physics*, vol. 16, p. 073020, jul 2014.

[124] J. Su, L. Cui, J. Li, Y. Liu, X. Li, and Z. Y. Ou, “Versatile and precise quantum state engineering by using nonlinear interferometers,” *Optics Express*, vol. 27, pp. 20479–20492, Jul 2019.

[125] J. Li, J. Su, L. Cui, T. Xie, Z. Y. Ou, and X. Li, “Generation of pure-state single photons with high heralding efficiency by using a three-stage nonlinear interferometer,” *Applied Physics Letters*, vol. 116, no. 20, p. 204002, 2020.

[126] L. Cui, J. Su, J. Li, Y. Liu, X. Li, and Z. Y. Ou, “Quantum state engineering by nonlinear quantum interference,” *Physical Review A*, vol. 102, p. 033718, Sep 2020.

[127] P. R. Sharapova, G. Frascella, M. Riabinin, A. M. Pérez, O. V. Tikhonova, S. Lemieux, R. W. Boyd, G. Leuchs, and M. V. Chekhova, “Properties of bright squeezed vacuum at increasing brightness,” *Physical Review Research*, vol. 2, p. 013371, Mar 2020.

[128] J. O’Brien, B. Patton, M. Sasaki, and J. Vučković, “Focus on integrated quantum optics,” *New Journal of Physics*, vol. 15, p. 035016, mar 2013.

[129] S. Tanzilli, A. Martin, F. Kaiser, M. De Micheli, O. Alibart, and D. Ostrowsky, “On the genesis and evolution of integrated quantum optics,” *Laser & Photonics Reviews*, vol. 6, no. 1, pp. 115–143.

[130] J. B. Spring, B. J. Metcalf, P. C. Humphreys, W. S. Kolthammer, X.-M. Jin, M. Barbieri, A. Datta, N. Thomas-Peter, N. K. Langford, D. Kundys, J. C. Gates, B. J. Smith, P. G. R. Smith, and I. A. Walmsley, “Boson sampling on a photonic chip,” *Science*, vol. 339, no. 6121, pp. 798–801, 2013.

[131] A. Peruzzo, M. Lobino, J. C. F. Matthews, N. Matsuda, A. Politi, K. Poulios, X.-Q. Zhou, Y. Lahini, N. Ismail, K. Wörhoff, Y. Bromberg, Y. Silberberg, M. G. Thompson, and J. L. OBrien, “Quantum walks of correlated photons,” *Science*, vol. 329, no. 5998, pp. 1500–1503, 2010.

[132] P. R. Sharapova, K. H. Luo, H. Herrmann, M. Reichelt, T. Meier, and C. Silberhorn, “Toolbox for the design of LiNbO3-based passive and active integrated quantum circuits,” *New Journal of Physics*, vol. 19, p. 123009, dec 2017.

[133] K.-H. Luo, S. Brauner, C. Eigner, P. R. Sharapova, R. Ricken, T. Meier, H. Herrmann, and C. Silberhorn, “Nonlinear integrated quantum electro-optic circuits,” *Science Advances*, vol. 5, no. 1, 2019.

[134] G. Frascella, R. V. Zakharov, O. V. Tikhonova, and M. V. Chekhova, "Experimental reconstruction of spatial schmidt modes for a wide-field SU(1,1) interferometer," *Laser Physics*, vol. 29, p. 124013, oct 2019.

[135] K. A. Kuznetsov, E. I. Malkova, R. V. Zakharov, O. V. Tikhonova, and G. K. Kitaeva, "Nonlinear interference in the strongly nondegenerate regime and schmidt mode analysis," *Physical Review A*, vol. 101, p. 053843, May 2020.

[136] P. R. Sharapova, O. V. Tikhonova, S. Lemieux, R. W. Boyd, and M. V. Chekhova, "Bright squeezed vacuum in a nonlinear interferometer: Frequency and temporal schmidt-mode description," *Physical Review A*, vol. 97, p. 053827, May 2018.

[137] G. Triginer, M. D. Vidrighin, N. Quesada, A. Eckstein, M. Moore, W. S. Kolthammer, J. E. Sipe, and I. A. Walmsley, "Understanding high-gain twin-beam sources using cascaded stimulated emission," *Physical Review X*, vol. 10, p. 031063, Sep 2020.

[138] D. Klyshko, "Ramsey interference in two-photon parametric scattering," *JETP*, vol. 104, pp. 2676–2684, 1993.

[139] D. S. Hum and M. M. Fejer, "Quasi-phasematching," *Comptes Rendus Physique*, vol. 8, no. 2, pp. 180 – 198, 2007. Recent advances in crystal optics.

[140] S. Helmfrid, G. Arvidsson, and J. Webjörn, "Influence of various imperfections on the conversion efficiency of second-harmonic generation in quasi-phase-matching lithium niobate waveguides," *Journal of the Optical Society of America B*, vol. 10, pp. 222–229, Feb 1993.

[141] A. B. U'Ren, C. Silberhorn, R. Erdmann, K. Banaszek, W. P. Grice, I. A. Walmsley, and M. G. Raymer, "Generation of pure-state single-photon wavepackets by conditional preparation based on spontaneous parametric downconversion," *arXiv preprint quant-ph/0611019*, 2006.

[142] W. P. Grice, A. B. U'Ren, and I. A. Walmsley, "Eliminating frequency and space-time correlations in multiphoton states," *Physical Review A*, vol. 64, p. 063815, Nov 2001.